EFFECTS OF MICROSTRUCTURE ON THE ELASTIC PROPERTIES OF SANDSTONES AND ITS SEISMIC IMPLICATION

A Dissertation Presented to

the Faculty of the Department of Earth and Atmospheric Sciences

University of Houston

In Partial Fulfillment

of the Requirements for the Degree

Doctor of Philosophy

By

Hui Li

December 2015

EFFECTS OF MICROSTRUCTURE ON THE ELASTIC PROPERTIES OF SANDSTONES AND ITS SEISMIC IMPLICATION

Hui Li

APPROVED:

Dr. De-hua Han, Co-chair
Department of Earth and Atmospheric Science

Dr. Hua-wei Zhou, Chair
Department of Earth and Atmospheric Science

Dr. Aibing Li
Department of Earth and Atmospheric Science

Dr. Ratnanabha Sain
ExxonMobil

Dean, College of Natural Sciences and Mathematics

Acknowledgement

I would like to express my sincere gratitude to my advisor, Dr. De-hua Han, who has provided me with assistance and guidance during my research. Without his help, I would have been unable to complete this dissertation. I would also like to thank my doctoral committee members, Dr. Hua-wei Zhou, Dr. Aibing Li, and Dr. Ratnanabha Sain for their advice, time, and commitment.

I would like to acknowledge the Rock Physics Lab at the University of Houston and all the researchers working there. The discussions with my colleagues Julian Yao, Min Sun, and Fuyong Yan, and many current and former students including Luanxiao Zhao, Hemin Yuan, Xuan Qin, Qi Huang, Yang Wang, Jiali Ren, and Qianqian Wei, who constantly inspired me and refreshed my interest in the subjects studied.

I am deeply thankful for the unselfish help and support from professor Xuehui Han and his student, Junxin Guo, at the China University of Petroleum during my research.

Finally, I am most indebted to my family, for their patience and encouragement. Without their support and sacrifice, I would not have been able to enjoy my academic life. I would also like to express my appreciation to my girlfriend, Lynn, for her generous and unconditional support.

EFFECTS OF MICROSTRUCTURE ON THE ELASTIC PROPERTIES OF SANDSTONES AND ITS SEISMIC IMPLICATION

An Abstract of a Thesis

Presented to

the Faculty of the Department of Earth and Atmospheric Sciences

University of Houston

In Partial Fulfillment

of the Requirements for the Degree

Doctor of Philosophy

By

Hui Li

December 2015

Abstract

The primary focus of this dissertation is to link the geological diagenesis mechanism of sandstones to theoretical rock-physics models and experimental measurements to quantitatively characterize the elastic modulus of sandstone from high-porosity (early geological stage) sediments to low-porosity consolidated (aged geological stage) rocks. In order to quantitatively investigate the velocity dispersion and attenuation mechanism of sandstones, the seismic-frequency measurements are conducted under both room-dry and partial gas or water-saturation conditions.

I address two main aspects of this research topic, from the theoretical point of view: (1) to modify the grain-contact models and understand the effect of micro-scale physical parameters on the elastic properties of porous-granular packs; and (2) to characterize the cementation thickness and cement material as feature-effects on the elastic modulus of cemented grain packs, with consideration of geological diagenesis. Meanwhile, from the experimental point of view: (1) to integrate the seismic-frequency measurements with ultrasonic measurements, and to quantitatively characterize velocity dispersion and attenuation mechanism of weakly consolidated sandstone under room-dry and partial water-saturation conditions; and (2) to conduct specialized ultrasonic measurements on the mixture of heavy oil-glass bead to investigate the uniquely elastic property of heavy oil-sand, which is predominantly temperature-dependent.

CONTENTS

List of Figures

List of Tables

Chapter 1
Introduction

The sandstone-reservoir rocks undergo complicated diagenesis but with a traceable geological history. The elastic property of sandstones is highly related to the geological environment, which, in itself, is a challenging issue. Theoretical rock-physics modeling and experimental measurements have been recognized to be promising approaches for characterizing sandstone-reservoir rock's elastic properties. However, the blurred understanding of the geological diagenesis mechanism of sandstone obstructs us from quantitatively characterizing its elastic modulus. In addition, the pore fluids is another key parameter for determining the elastic properties and seismic responses. It is essential to establish a rock-physics relationship to link the physical properties of sandstone to their historically geological diagenesis. Specific laboratory measurements were undertaken to establish this link.

1.1 Geological background of sandstones

The geological history of sandstone can be split into three stages: suspension, deposition, and compaction. Mechanical compaction and chemical compaction are the two-basic phenomena that underlie the elastic properties of sandstone.

1.1.1 Mechanical compaction

The compaction of sand grains usually goes through stages of dynamic and static processes, as seen in Figure 1.1. The nonlinear variation in the elastic property of sandstone by gravity can be observed at the static stage. The deformation of unconsolidated sands is time-dependent, where a threshold of viscous-compaction pressure causes an inelastic to elastic transition or the reverse (Hagin and Zoback, 2004).

Either soft-pore or micro-crack closure or grain repacking could induce inelastic compaction. As sand grains start to stabilize as a random, condensed structure, further packing by the increased pressure, as seen in the laboratory, is mainly elastic. A variable parameter, coordination number, of significantly affecting the elastic property of sandstone is fairly stable. However, while the ultrasonic measurement points are elastic, increased pressure process is inelastic. More specifically, we always measure the elastic properties of a "new" rock during the pressure cycles.

1.1.2 Chemical compaction

For the geological diagenesis of clastic rocks, increased pressure compacts buried sediments. This is a quasi-static, inelastic process. With increasing depth, sand grains can flow, roll over, slide, deform, and break to repack and reduce porosity. As Figure 1.1 shows, the mechanical compaction vanishes when the temperature reaches 70 ^{o}C. However, the chemical compaction process, including

pressure, mineral precipitation, and cementation, will occur and continue to reduce porosity significantly.

With the rise in pressure and temperature as the depth increases, cementation could occur due to mineral precipitation or chemical reaction-induced cementation by pore-filling materials. Cementation significantly influences the elastic properties of sandstones through the following factors: first, the physical property of the cementation materials has a significant impact on elastic properties of sandstones; second, the fraction of cementation materials is non-ignorable; and third, distribution of cementation is another key factor should be considered.

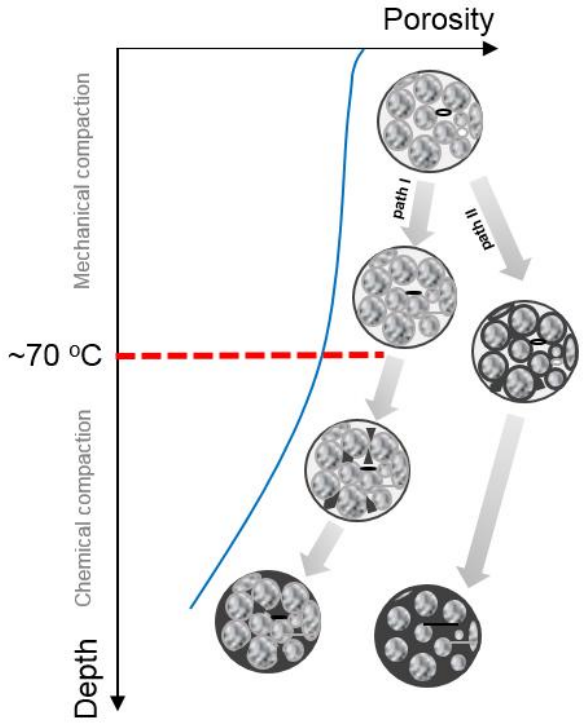

Figure 1.1 A schematic of sand-clay compaction. At 70 °C, mechanical compaction gradually transforms into predominantly chemical compaction in siliciclastic systems.

For quartz-rich sands, initial cementation tends to start at the same depth. Path I is direct grain contact with cementation around the corner of grain contacts, while path II is direct grain contact with coating cementation.

1.2 Effects of sorting and packing on grain-contact model

Sorting and packing are textural properties of the clastic sediments, which are initially associated with the depositional process. Sorting refers to the spread of the grain-size population. Packing refers to the grain concentration. They both are closely related to porosity. For un-cemented granular packs in the same pressure condition, sorting and packing are considered to be the dominant mechanisms affecting velocity-porosity, and is generally calculated from rock-physics models of an idealized sphere packs (Marion et al., 1992; Avseth et al., 2000; Dvorkin and Gutierrez, 2001; Zimmer et al., 2002; Zimmer, 2003). However, the main source of uncertainty in these contact models comes from the coordination number and the assumption of using an idealized sphere grain. Therefore, incorporating a reasonable coordination number into the grain-contact model is a reasonable representation of the sorting and packing effects.

1.3 Effect of cementation on cement-contact model

During diagenesis, unconsolidated sands are likely to become cemented sandstone. The cemented material may be diagenetic quartz, calcite, albite, or other minerals. Cementation has a rigid, stiffening effect, because the grain contacts are glued together (Avesth et al., 2010). Moreover, according to the cement-contact model (Dovrkin et al.,

1994), the cementation distribution is also a key parameter that affects the stiffness of sandstone, Figure 1.2.

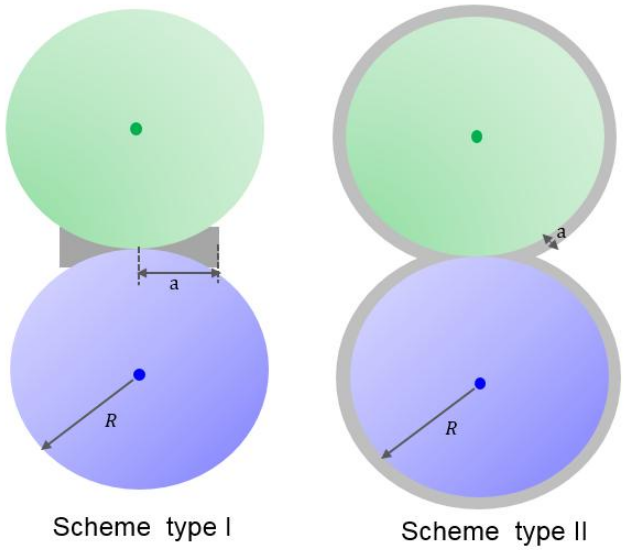

(a) (b)

Figure 1.2 A schematic of sand grains with cementation: (a) arrangement type I; (b) arrangement type II.

1.4 Stress magnitude and strain-amplitude order

For the original geological packing process, the compaction of sediments usually goes through stages of dynamic and static process. The static process possibly occurs at the stage of mechanical compaction, while the dynamic process is observed when the sediments are completely lithified at the stage of chemical compaction, or after the grain packs are stabilized during the pressure-involved laboratory measurement. The strain-amplitude order is a quantitative parameter in the laboratory measurement. When the magnitude of the measured strain amplitude is less 10^{-6}, it is assumed to be a dynamic

(elastic) measurement. In comparison, when the magnitude of the strain amplitude is over 10^{-6}, it is considered to be a static (inelastic) measurement.

For original process of geological packing, the critical porosity mechanically divides sandstone into a static stage and a dynamic stage, Figure 1.3 (a). While static stage of laboratory measurements generally occurs when the confining pressure is less than 20 MPa, Figure 1.3 (b). "Static" indicates that the suspension particles or artificial loose-grain packs slide into more stable positions, forming tighter packing with low porosity and increased grain-to-grain contacts. On the other hand, based on a specific geological environment, a primarily mechanical with a partially chemical process could occur. This would cause grain deformation, even under increased pressure. Point contacts between grains would be gradually transformed into flat contacts and, finally, into concave or sutured contacts. While "dynamic" suggests that only elastic diagenesis can be implemented with increased pressure. With regarding to the laboratory measurement, the strain-amplitude order is always less 10^{-6} at dynamic stage before the rock yields.

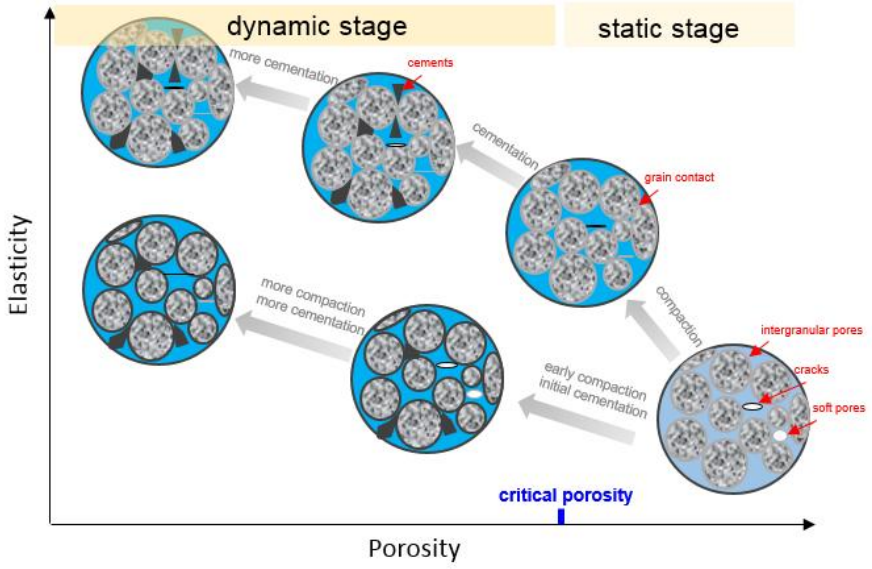

(a)

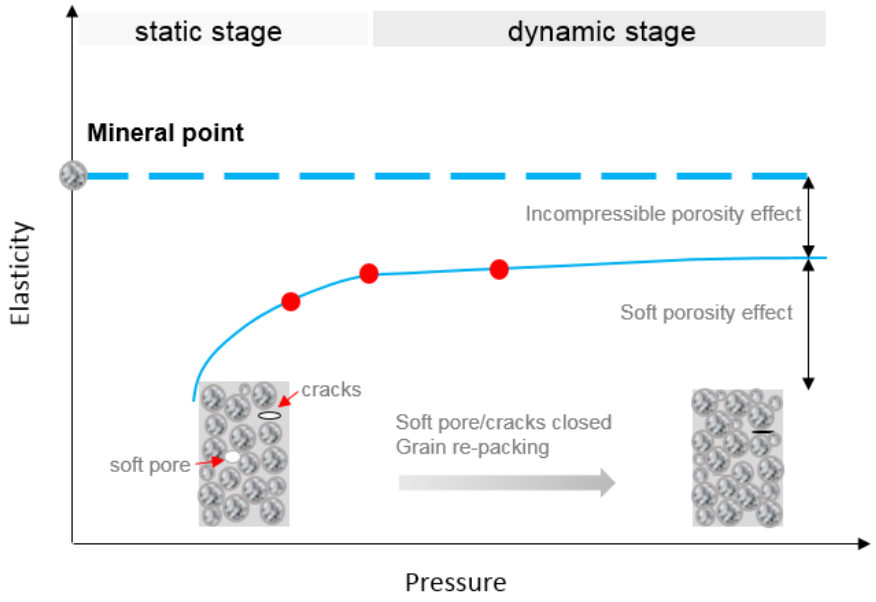

(b)

Figure 1.3 (a) The elasticity against porosity during geological diagenesis; (b) Elasticity against pressure during laboratory measurement.

1.5 Frequency and scale

With respect to clastic rocks, the geological process and the statistical fluctuation in geological history can cause sedimentary rocks to exhibit heterogeneities, ranging from the micrometer grain and pore scale to the many-kilometer basin scale. Moreover, the frequencies of measured waves can span from several Hz to 10^7 Hz. Correspondingly, scales and frequencies of geophysical measurements range from millimeter wavelength in high-frequency ultrasonic measurements to tens of meters in low-frequency surface seismic, Figure 1.4.

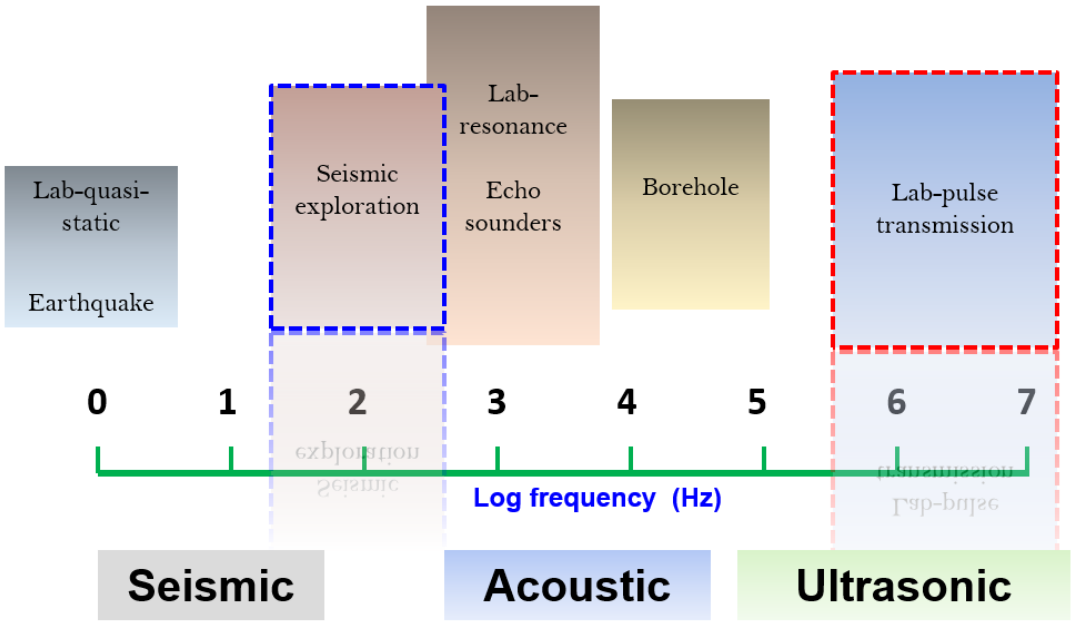

Figure 1.4 A scheme of scales and frequencies used for variously geophysical measurements.

Figure 1.5 shows the frequency-dependent intrinsic attenuation of P-wave determined from a series of experiments conducted at the Imperial College test site (Sams et al., 1997). These experimental results combine ultrasonic measurements (300-900 kHz) with sonic logs (8-24 kHz), crosswell (0.2-2.3 kHz), and vertical seismic profile (VSP) data (30-280 Hz), suggesting that a significant amount of energy loss can take place over a broad frequency range.

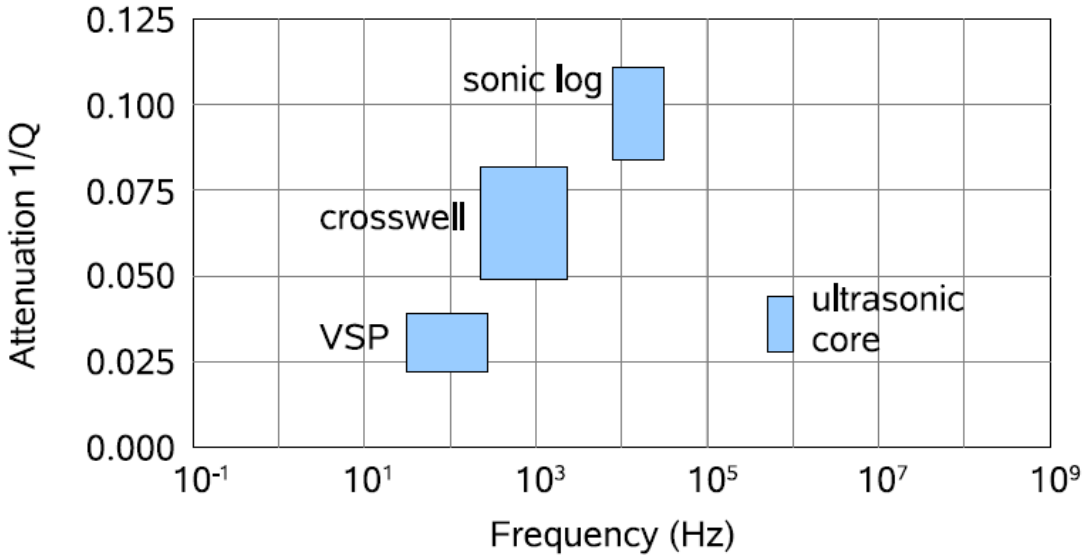

Figure 1.5 Intrinsic P-wave attenuation, 1/Q, plotted as a function of the frequency on the rocks at the Imperial College test site (Sams et al., 1997). VSP and sonic-log estimations is corrected for scattering attenuation.

The intrinsic dispersion and attenuation arise a wave-induced fluid flow (WIFF) mechanism. WIFF occurs as passing waves create pressure gradients within the fluid phase, and internal friction accompanies the resulting movement of the fluid relative to the solid until the pore pressure is equilibrated (Müller et al., 2010). Therefore, frequency-dependent waves, propagating in a fluid-saturated porous media, could cause scale-dependent intrinsic dispersion and attenuation, where the mechanical energy would dissipate into heat (Aki and Richards, 1980). The integration of the geophysical measurement of rock's property at different frequencies aids in the complete understanding of the complexity of clastic rocks.

1.6 Motivations

Unconsolidated sands and consolidated sandstones are porous, granular sedimentary rocks with pore-filling materials, which may strengthen the rock frame or only occupy the pore space depending on the geological diagenesis. This research focuses on the prediction of elastic property of sandstones from experimental measurements, integrating concepts from a theoretical rock-physics model, sedimentary geology, and geo-mechanisms. This work has developed rock-physics models and measurement method that will assist in the assessment of sandstone (heavy oils) reservoir. The primary aim is the thorough understanding of the effects of micro-scale physical parameters on the elastic properties of sandstones, taking geological diagenesis into consideration. More specifically, it addresses three-key issues:

(a) How do the microstructures of unconsolidated sediments impact their elastic properties? What role does the geological diagenesis play in determining the elastic properties of clastic rocks? With respect to loose-sand media, surface friction between grain contacts is non-ignorable, resulting in the tangential loading path being irreversible when tangential stress is added. Moreover, the tangential stress will cause partial sliding on the surface of grain contacts. Macroscopically, the effective shear modulus increases when increased partial slip-grain contacts, or increased micro-friction on the area of grain contacts. Regarding poorly cemented sandstones, the numerical simulations show that both the cementation thickness and cementation feature have significant impacts

on elastic property of consolidated sandstone. In addition, the position of cementation is another key parameter that should be considered when applying cement-contact model to predict elastic properties of consolidated sandstones.

(b) What is the effect of frequency on the elastic property of fluid-saturated sandstone in laboratory measurement? How does the degree of water-saturation affect the elastic property of water-saturated sandstone? How is low-frequency measurement conducted in the laboratory? It was known that when waves pass through partially fluid-saturated sandstones, there would be velocity dispersion and attenuation (Winkler, 1989; Han et al., 2004; Batzle et al., 2006). It may exist different interpretation mechanisms of inducing velocity dispersion and attenuation (Biot, 1956a, 1956b, 1962). Measuring these phenomena in the laboratory within the seismic frequency band is always challenging. The low-frequency measurements ranging from 2 Hz to 800 Hz are conducted for the partially water-saturated sandstones. Meanwhile, simultaneous measurements over the ultrasonic frequency band (1000 KHz) are also conducted to ensure that the measurements are consistent.

(c) How can we experimentally measure the "as-is" porosity of sample of heavy oil-sand? What is the role of heavy oil in determining the elastic property of heavy oil-sand? Can we quantitatively characterize the effects of temperature, pressure, and microstructure on the heavy oil-sand reservoir? A promising measurement strategy is proposed to identify the "as-is" porosity of a heavy oil-sand sample. The proposed strategy not only keeps the sample intact, but is

also advantageous in minimizing mass loss and external covers using Archimedes principle. Moreover, porosity calculated from a direct measurement gives us a low bound of porosity, while the "as-is" porosity, estimated from Archimedes principle, presents an upper bound of porosity. It is found that the elastic properties of heavy oil-sand is affected by multiphase of heavy oil and solid matrix with regards to the temperature, pressure, and microstructure. In particular, the viscosity-induced elastic modulus of heavy oil makes the elastic property of heavy oil-saturated grain packs temperature-dependent.

1.7 Dissertation organization

The first part of this dissertation, which constitutes chapter 2 to chapter 4, presents the results regarding both theoretical rock-physics modeling and experimental measurements of the elastic property of sandstones. The second part, which includes chapter 5 and chapter 6, deals with the elastic property of sample of heavy oil-sand.

Chapter 2 specifically focuses on the rock-physics modeling of unconsolidated sands, which accounts for the macroscopic stress-heterogeneity distribution of grain packs and microscopic friction on the area of grain contacts. Based on a theoretical analysis and numerical simulation, it is demonstrated that surface friction between grain contacts is non-ignorable, which results in the tangential loading-path being irreversible when tangential stress is added. Moreover, the tangential stress causes partial sliding on the surface of grain contacts. Macroscopically, the effective shear modulus increases with increased partial slip-grain contacts, or increased micro-friction on the area of grain

contacts.

Chapter 3 analyzes the effects of cementation thickness and cementation feature on the elastic property of poorly consolidated sandstones and their relationship with the geological diagenesis.

Chapter 4 uses the force-deformation principle to experimentally investigate the effect of partial water-saturation on sandstone over the low-frequency band. Seismic waves, propagating in fluid-saturated porous rocks, are subject to intrinsic dispersion and attenuation, where the mechanical energy dissipates into heat (Aki and Richards, 1980). Here, intrinsic attenuation refers to the relative movement between pore fluids and skeleton due to the pore-pressure gradient. Theoretically, Gassmann's equation is applied to characterize the elastic property of sandstone at relaxed frequency (2 Hz). Meanwhile, Cole-Cole equation, as a model of characterizing single dispersion and attenuation mechanism of fluids-saturated rock, is utilized to verify the measured Young's model and predict corresponding attenuation.

Chapter 5 mainly focuses on dealing with the issues of heavy oil-sand. A confined porosity-measurement strategy is specifically proposed to measure the "as-is" porosity of a heavy oil-sand sample. This proposed strategy successfully estimates the "as-is" porosity of heavy oil-sand, using the Archimedes principle. It can be assumed to be the upper bound of porosity. More importantly, Archimedes principle not only keeps the sample intact but is also advantageous for minimizing mass loss and external covers. Furthermore, another porosity data, calculated by the direct measurement of grain volume and bulk volume, leads us to a low bound of porosity.

Chapter 6 experimentally studies the elastic properties of heavy oil-sand, influenced by the multiphase of heavy oil and the solid matrix with regard to temperature, pressure, and microstructure. The specialized ultrasonic measurements are designed and performed for both heavy oil and heavy oil-saturated grain packs. It is found that heavy oil acts as a part of solid frame of the heavy oil-sand when the viscosity of heavy oil reaches 10^{15} cP at the temperature of the glass point, while heavy oil is likely to be movable, accordingly, once its viscosity dramatically drops to ~10^{3} cP at the temperature of the liquid point. The viscosity-induced elastic modulus of heavy oil, in turn, makes the elastic properties of heavy oil-saturated grain packs particularly temperature-dependent. Therefore, the temperature, as the external condition, is the first-order factor to determine the elastic property of the sample of heavy oil saturated-sand packs.

Chapter 2
Rock-physics modeling of unconsolidated sands

2.1 Geological background of sandstones

The geological history of sandstone can be split into three stages: suspension, deposition, and compaction. Laboratory experiments demonstrate that the deposition condition for sandstones has a strong impact on the concentration of natural sediments (Allen, 1991). The results from different studies (Steinour, 1944; Kolbuszewski, 1948; and Macrae and Gray, 1961) indicated that the grain concentration varies from a constant value of about 0.65 at a small rate of deposition to a lower constant value of about 0.55 at a fast rate of deposition under the assumption of identical grain. Mechanical compaction and chemical compaction are the two-basic phenomena that underlie the elastic properties of sandstones.

2.2 Classification of rock physics models

Rock-physics model is a powerful tool to bridge the elastic properties of sandstones and the physical parameters, which include porosity, fluid saturation, pressure, mineral composition, and degree of consolidation. Both theoretical studies and laboratory experiments are conducted to identify the effects of physical parameters on the elastic properties of sandstones. On the one hand, experimental observations need to be

interpreted by theoretical rock-physics models. On the other hand, because assumptions must be made in developing any rock-physics models to simplify the mathematics, experimental observations are required to verify the validity of the assumptions.

Grain-contact models are mostly developed to study the effective elastic properties of a random granular packs. Most contact models (Brandt, 1955; Walton, 1987; Digby, 1981; Noriss and Johnson, 1997; Makse and Herrmann., 1999; Jenskin, 2005) are based on the Hertz-Mindlin solution (Hertz, 1884; Mindlin, 1949). The key parameters determining the stiffness of grain packs are the elastic modulus of the spherical grains and the area of grain contacts, which results from the deformability of the grain under external pressure (Avseth et al., 2005).

Hertz (1884), Mindlin (1949), Digby(1981), Walton (1987), and Johnson (1988) have studied the normal stiffness of two-grains in contacts, deformed by the only external normal-force, Figure 2.1(a). The contact area of two-grain spheres is related to Young's modulus E, Poisson's ratio υ, the radius R of the grain sphere, and the applied force F_n. The radius of the contact area is given by

$$a_n = \left(\frac{3F_nR(1-\upsilon^2)}{4E}\right)^{\frac{1}{3}} = \left(\frac{3F_nR(1-\upsilon)}{8G}\right)^{\frac{1}{3}} \tag{2.1}$$

It is assumed to be smaller than the grain radius. G is the shear modulus of the grain.

The displacement between the center of the two-grain spheres is given by

$$u = \frac{2a_n^{\ 2}}{R} = \frac{2}{R}\left(\frac{3F_nR\ (1-\upsilon)}{8G}\right)^{\frac{2}{3}} \tag{2.2}$$

Therefore, the normal contact stiffness S_n is

$$S_n = \frac{2}{du/dF_n} = \frac{4Ga_n}{1-\upsilon} \tag{2.3}$$

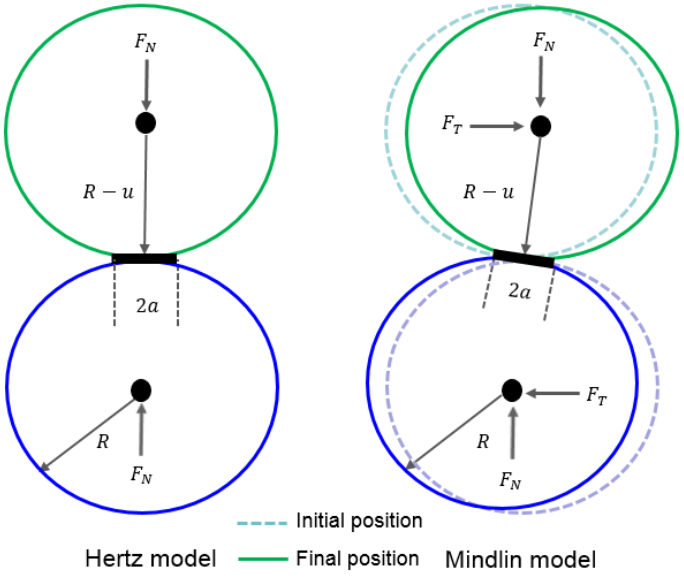

(a) (b)

Figure 2.1 Schematic illustrations of (a) Hertz model; and (b) Mindlin model of two-grain spheres.

Mindlin (1949) formulated a model that includes both normal and tangential forces, Figure 2.1(b). It has been proved that the shear stiffness is more sensitive to the sequence of loading, the area of grain contact, and friction coefficient. It is assumed that no slip should occur at the contact-surface area as long as the applied tangential force F_t is much smaller than the limit of friction force μF_n, where μ is the coefficient of friction.

The tangential displacement u_t is

$$u_t = \frac{3\mu F_n (2-\upsilon)\left[1-\left(1-\frac{F_t}{\mu F_n}\right)^{\frac{2}{3}}\right]}{8Ga} \tag{2.4}$$

Therefore, the tangential contact stiffness S_t is

$$S_t = \frac{2}{du/dF_t} = \frac{8Ga}{2-\upsilon}\left(1-\frac{F_t}{\mu F_n}\right)^{\frac{1}{3}} \tag{2.5}$$

In Equation 2.5, if $F_t = \mu F_n$, the shear stiffness is null, which is a frictionless case, as Walton (1987) proposed. It will reduce to the low bound of elastic property of random grain packs, Figure 2.2. If set $\mu F_n \to \infty$, then $\frac{F_t}{\mu F_n}$ is close to 0. As a result, an upper bound of shear stiffness is given by

$$S_t = \frac{8Ga}{2-\upsilon} \tag{2.6}$$

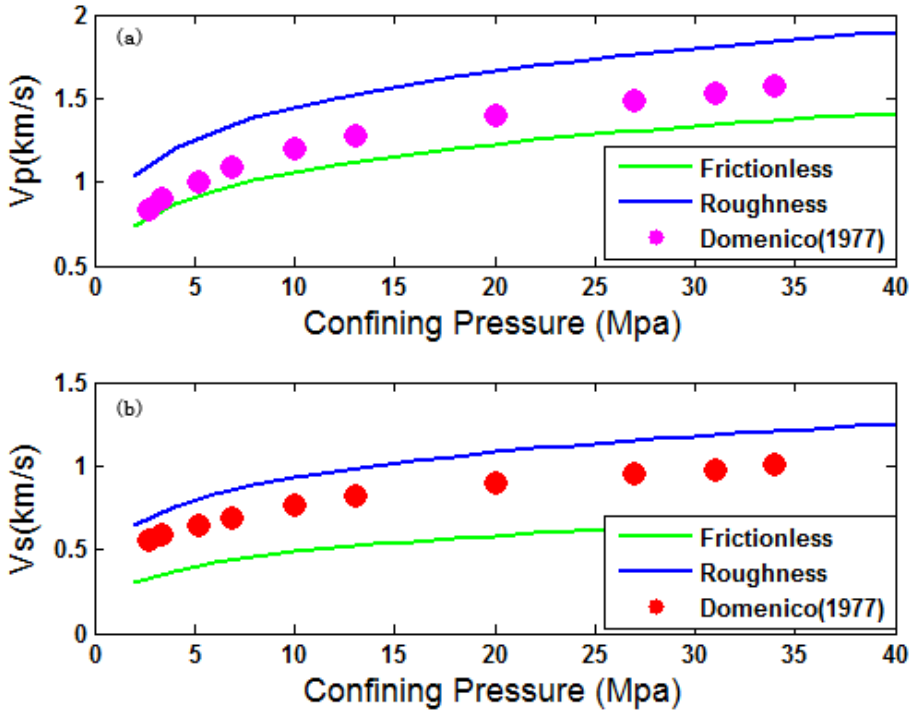

Figure 2.2 Calculation of P-wave and S-wave velocities of a condensed sand-packs using Walton's roughness and frictionless-sphere models; the measured velocities of a glass-bead packs (Domenico, 1977) is also listed.

Digby (1981) related the shear stiffness to the pre-existing radius b of the area of grain contacts as follows

$$S_t = \frac{8Gb}{2-\upsilon} \tag{2.7}$$

The normal displacement of the grain contact satisfies (Digby, 1981)

$$\frac{\delta}{a} + \frac{b}{R_1}\left\{\sin^{-1}(\frac{c}{a}) - \sin^{-1}(\frac{b}{a})\right\} + \frac{a}{cR_1}\left\{b(1-\frac{c^2}{a^2})^{0.5} - c(1-\frac{b^2}{a^2})^{0.5}\right\} = 0 \quad \text{if}$$

$$a \geq c > b > 0 \tag{2.8}$$

Normal force is given by

$$
\begin{aligned}
Y = & \frac{4\mu a\delta}{(1-\upsilon)} + \frac{2\mu b a^3}{3R_1 c(1-\upsilon)}(2+\frac{c^2}{a^2})(1-\frac{c^2}{a^2})^{0.5} \\
& - \frac{2\mu a^3}{3R_1 c(1-\upsilon)}(2+\frac{b^2}{a^2})(1-\frac{b^2}{a^2})^{0.5} \qquad \text{if } a \geq c > b > 0 \\
& + \frac{2\mu a^2 b}{R_1(1-\upsilon)}\left\{\sin^{-1}(\frac{c}{a}) - \sin^{-1}(\frac{b}{a})\right\}
\end{aligned} \tag{2.9}
$$

If set $c \to b+0,\ b=0$

$$
\begin{aligned}
& \delta = a(a^2 - b^2)^{0.5} / R \\
& Y = \frac{4\mu}{(1-\upsilon)}\left\{a\delta - \frac{(a^2-b^2)^1}{R}\right\}^{\frac{3}{2}}
\end{aligned} \tag{2.10}
$$

2.3 Rock-physics modeling of unconsolidated sands: accounting for partial friction-grain contacts and the heterogeneous stress field

2.3.1 Abstract

A partial friction-heterogeneity model of a random-compacted granular medium can be formulated using two parameters (f_p , $f(\mu)$) to account for (1) the macroscopic stress-heterogeneity distribution of grain packs and (2) the microscopic friction on the area of grain contact. This proposed partial friction-heterogeneity model indicates that surface friction on the surface of grain contacts is non-ignorable, which results in the tangential loading path being irreversible when tangential stress id added. Moreover, the tangential stress causes partial sliding on the surface of grain contacts. Macroscopically, the effective shear modulus will increase when partial slip-grain contacts or micro-friction on the area of grain contacts increases.

2.3.2 Introduction

Hertz (1882), Mindlin (1949), Brandt (1955), Digby (1981), Walton (1987), and Noriss and Johnson (1997) initially developed grain-contact model, which is an alternative rock-physics method of studying the elastic properties of a porous granular medium. Both the normal and tangential stiffness determine the elastic properties of a random granular packs. The key parameters in determining the stiffness are mineral modulus of the spherical grains and the area of grain contacts (Avseth et al., 2005). However, due to the failure of understanding the fundamental physical-law behind the random granular packs, only the boundary limits of the elastic property of a randomly-packed sphere-medium are investigated under specific assumptions.

According to Walton's model (1987), the rough-sphere case assumes no slippage across the area of grain contacts, implying infinite friction on the area of grain contacts. It gives an upper boundary of effective modulus of the assembled-granular medium. By contrast, the smooth-sphere case assumes frictionless contacts, which allows partial slip to take place across the whole area of grain contact. Therefore, a low bound of effective modulus can be calculated as well.

Bachrach and Avseth (2008) argued that the assumptions of a perfectly smooth and infinite rough-surface case in a random pack may be invalid. Then an ad hoc model is presented to characterize stress heterogeneities on the grain packs. Dutta et al. (2010) followed a similar approach of mixing frictionless and infinite-friction spheres, which inverts the coordination number from dynamic measurement. Duffaut et al. (2010) argued

that the fundamental contact law should consider partial slip on the surface of grain contacts. Based on Mindlin's partial-slip model (1949) and the assumption of a uniform stress-strain field, effective modulus of grain packs is derived.

Considering the fact that friction on the grain surface cannot completely hold the grain pairs without relative slip in the field case, Mindlin (1949) further extended the assumption of no-slip on grain contacts. Hence, partial slip could take place whenever the tangential stress exceeds the internal friction on the surface of grain contacts.

The previous derivation of the grain-contact stiffness and the effective modulus of a random granular packs with friction on the area of grain contacts are based on the assumption that all stress-strain fields are homogeneous (Duffaut, 2010). However, Sain (2010) has numerically proved that the stress distribution of random granular packs is considerably heterogeneous and evolves with pressure as well. As a result, the assumption of homogeneous-stress distribution on each grain will not capture the heterogeneities of a stress field as tangential stiffness is path-dependent (Bachrach, 2008).

Furthermore, elastic property observed from laboratory measurements on random granular packs display significant discrepancies comparing with prediction of using grain-contact model, especially for shear modulus. Therefore, to verify that the observed truth of the stress distribution of each grain is macroscopically heterogeneous and partial slip could take place on the area of grain contacts microscopically, a new expression for predicting the effective shear modulus is proposed. The partial friction-heterogeneity model assumes a non-uniform stress-strain field applied to a random grain packs composed of frictional-grain contacts. Meanwhile, experimental data (Domenico, 1977)

demonstrates that the partial friction-heterogeneity model is capable of predicting the elastic properties of unconsolidated sediments that have different inter-particle friction in the microscopic scale and heterogeneous stress in the macroscopic scale.

2.3.3 Grain-contact theory

Effective bulk and shear modulus of a granular medium with a homogenous stress-strain field

Digby (1981) solved the grain-interaction issues of an assembly of spherical particles that are initially bonded together across the contact area.

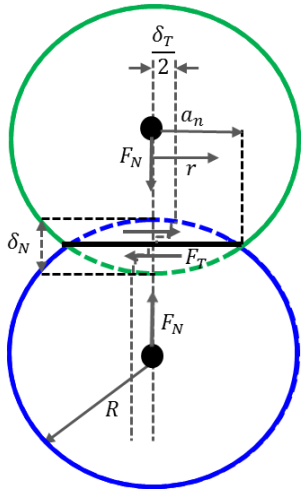

Figure 2.3 Schematic view of identical two-sphere grains undergoing deformation when pressure is added.

Based on assumptions that there is either no initial bonding or the contact radius a_n is greater than or equal to the bonding radius, the effective-bulk modulus is given by

$$K_{dry}^{eff} = \frac{(1-\phi)C_p}{12\pi R} S_n \tag{2.11}$$

where ϕ is the porosity, C_p is the coordination number, and R is the sphere radius, Figure 2.3. The normal stiffness contact S_n is (Digby, 1981)

$$S_n = \frac{\partial F_n}{\partial \delta} = \frac{4Ga_n}{1-\upsilon} \tag{2.12}$$

where F_n and δ are the normal force acting on the grain contacts and normal displacement resulting from such a force, respectively. G and υ are the shear modulus and Poisson's ratio of a single grain, respectively. a_n is the contact radius. The corresponding effective shear modulus is given by

$$G_{dry}^{eff} = \frac{(1-\phi)C_p}{20\pi R}(S_n + \frac{3}{2}S_\tau) \tag{2.13}$$

where S_τ is the tangential contact stiffness.

$$S_\tau = \frac{\partial F_t}{\partial \tau} = \frac{8Ga_t}{2-\upsilon} \tag{2.14}$$

where F_t and τ are the tangential force acting on the grain contacts and tangential displacement resulting from such a force, respectively. a_t is the radius of the contact region held by friction. The tangential stiffness not only depends on the boundary conditions, but also depends on the loading path (Noriss and Johnson, 1997).

Heterogeneous stress-strain field of a random granular packs

Since the stress-strain distribution on a random granular packs is non-uniform,

Figure 2.4. The tangential stiffness is path-dependent. Consequently, the assumption of all the grain contacts are the same (Digby, 1981; Walton, 1987; Noriss and Johnson, 1997) cannot not fully capture such heterogeneities. Hence, a promising way to accommodate heterogeneities of the stress-strain field is proposed.

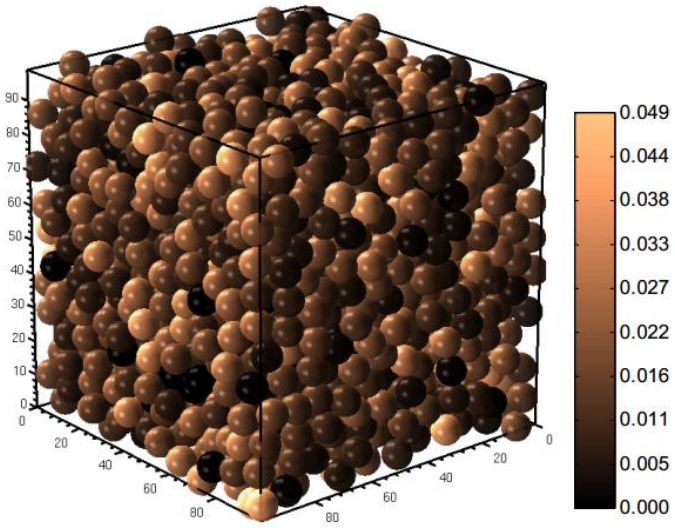

Figure 2.4 The heterogeneity distribution of mean-stress for each grain in a stable granular pack. The color bar shows stress magnitudes in MPa (Sain, 2010).

Based on the same grain contacts, the strain-energy density per unit volume U is given by (Digby, 1981; Walton, 1987; Noriss and Johnson; 1997)

$$U = \frac{1}{V}\sum_{contacts}\int \vec{F}\cdot d\vec{u} \approx \frac{C_p(1-\phi)}{V_0}\left\langle \int \vec{F}\cdot d\vec{u} \right\rangle \tag{2.15}$$

where V_0 is the volume of a single grain. $\vec{F}\cdot d\vec{u} = F_n \cdot d\delta + F_t \cdot d\tau$ with respect to strain and V is the volume associated with the effective average medium approach (Digby, 1981).

Considering the truth of heterogonous-stress distribution in a random granular packs, some of the grain contacts behave like smooth contacts with zero tangential stiffness, while some display infinite tangential stiffness (Walton, 1987). More importantly, the rest of the grain contacts may slide partially if an external force-fluctuation exists. This assumption attempts to account for the heterogeneities of stress distribution on a porous-granular medium as observed in laboratory measurement and numerical simulations (Geng et al., 2001; Markse et al., 2004).

The binary model, simplified from the true grain packs, can be viewed as a probable distribution of non-uniform contacts. Therefore, Equation 2.15 is given by

$$\begin{aligned} U &= U_s + U_p + U_n \\ &= \sum_{smooth} \sum_{contacts} \int \vec{F} \cdot d\vec{u} + \sum_{partial} \sum_{contacts} \int \vec{F} \cdot d\vec{u} + \sum_{no-slip} \sum_{contacts} \int \vec{F} \cdot d\vec{u} \\ &= \frac{n(1-\phi)}{V_0} \left(f_s \left\langle \int \vec{F} \cdot d\vec{u} \right\rangle + f_p \left\langle \int \vec{F} \cdot d\vec{u} \right\rangle \right) \end{aligned} \tag{2.16}$$

where f_s is the fraction of smooth contacts, and $f_p = 1 - f_s$ is the fraction of the partial slip contacts. The tangential force, however small, causes some partial slip to occur over part of the contact area (Johnson, 1988). Hence, the no-slip contact term is eliminated.

The macroscopic stress is derived by differentiating Equation 2.16 with respect to the strain (Noriss and Johnson, 1997):

$$\sigma_{ij} = \frac{\partial U}{\partial e_{ij}} = \frac{\partial U_s}{\partial e_{ij}} + \frac{\partial U_p}{\partial e_{ij}} \tag{2.17}$$

Because of the linearity of Equation 2.17, the macroscopic stress-strain relations

for heterogeneous stress-distribution of grain contacts is given by

$$\sigma_{ij} = (f_s C^*_{ijkl}(S_n, S_t = 0) + f_p C^*_{ijkl}(S_n, S_t \neq 0))e_{kl} \tag{2.18}$$

Combined with normal stiffness, Equation 2.12, and shear stiffness, Equation 2.14, the effective modulus in terms of the volume fraction of partial slip contacts f_p is given by

$$K^{eff}_{dry} = \frac{C_p(1-\phi)}{12\pi R} S_n \tag{2.19a}$$

$$G^{eff}_{dry} = \frac{C_p(1-\phi)}{20\pi R}(S_n + \frac{3}{2} f_p S_t) \tag{2.19b}$$

2.3.4 Partial slip on the surface of grain contacts with non-zero friction

Bachrach and Avseth (2008) argued that the assumption of perfectly smooth and infinitely-rough spheres in a random-granular pack may be invalid. Therefore, friction heterogeneities on the area of grain contacts should be considered. Figure 2.5 shows that grain surface is frictional due to chemical interaction, mechanical interaction, etc. during geological diagenesis.

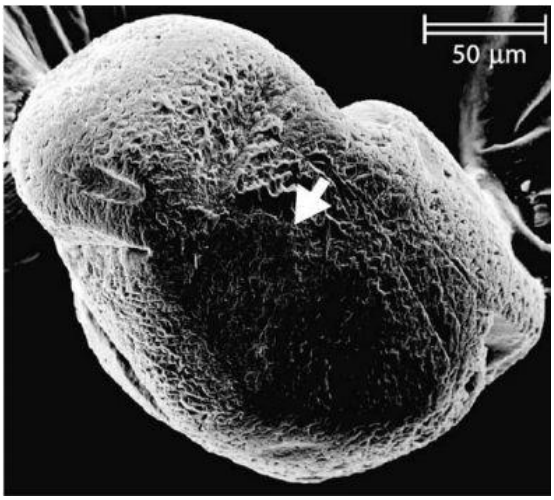

Figure 2.5 SE image of single grain surface showing micro-roughness (Chester, 2004).

Partial friction-grain contact model assumes that partial slip initiates at the outer radius a of a circular contact zone under constant normal force F_n and steadily increasing tangential force F_t (Mindlin, 1949). According to the Hertz-Mindlin model, the partial sliding could take place in the circular contact zone ($c \le r \le a$), and

$$\frac{c}{a} = \left(1 - \frac{F_t}{\mu F_n}\right)^{\frac{1}{3}} \tag{2.20}$$

which shows that the inner no-slip zone ($r = c$) is a function of contact forces, F_n, F_t, and the static friction coefficient μ.

Tangential stiffness depends on the boundary conditions and loading path for a random-granular packs (Noriss, Johnson, 1997). It implies that the partial sliding of grains is not simply irreversible along the loading trajectory when oscillating stress passes through, Figure 2.6, because the peak of oscillating stress can be considered to be

force loading and its trough can be considered to be force unloading.

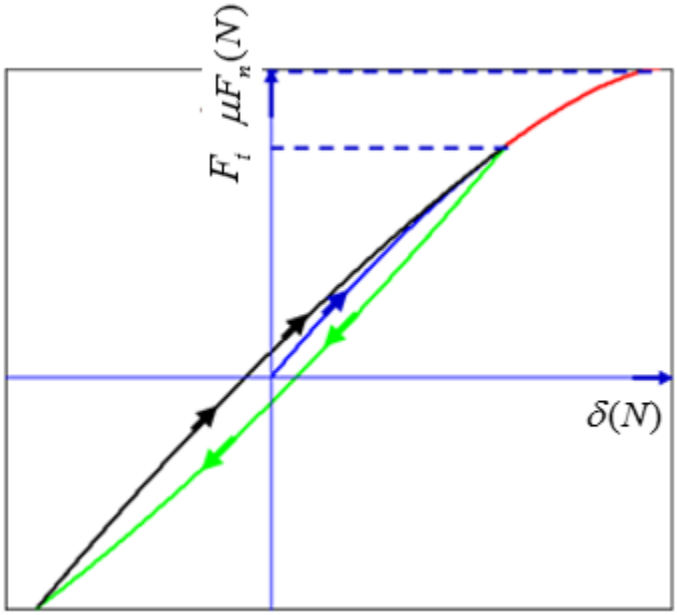

Figure 2.6 Schematic relation between tangential stress and loading path history.

The shear stress-distribution across the contact surface is given by (Mindlin, 1949)

$$\tau = \begin{cases} -\dfrac{3\mu F_n}{2\pi a^3}(a^2 - r^2)^{\frac{1}{2}} & c' \le r \le a \\ -\dfrac{3\mu F_n}{2\pi a^3}\{(a^2 - r^2)^{\frac{1}{2}} - 2(c'^2 - r^2)^{\frac{1}{2}}\} & c \le r \le c' \\ -\dfrac{3\mu F_n}{2\pi a^3}\{(a^2 - r^2)^{\frac{1}{2}} - 2(c'^2 - r^2)^{\frac{1}{2}} + (c^2 - r^2)^{\frac{1}{2}}\} & r \le c \end{cases} \tag{2.21}$$

where c is the radius of the inner no-slip zone with tangential force loading, c' is the radius of the inner no-slip zone with tangential force unloading.

Furthermore, Mindlin (1949) assumed that the surface displacement of grain δ_t within the no-slip zone is uniform. Thus, the tangential force-displacement relation is

given by

$$F_t = \mu F_n[1-(1-\frac{16Ga\delta_t}{3(2-\upsilon)\mu F_n})^{\frac{3}{2}}] \tag{2.22}$$

Subsequently, it is easy obtain tangential stiffness by differentiating Equation 2.22 with respect to the displacement ($\partial F_t / \partial \delta_t$):

$$S_t = \frac{8Ga}{2-\upsilon}(1-\frac{F_t}{\mu F_n})^{\frac{1}{3}} \tag{2.23}$$

Which is also the equation that Mindlin (1949) deduced. The tangential stiffness can now vary nonlinearly with the applied tangential force according to Equation 2.23. A new expression of the effective shear modulus of a random dense packs with frictional contacts is given by

$$G_{dry}^{eff} = \frac{C_p(1-\phi)}{20\pi R}(S_n + \frac{3}{2}f_p f(u)S_t') \tag{2.24}$$

Here, $f(u) = (1-\frac{F_t}{\mu F_n})^{\frac{1}{3}}$, S_t' is tangential stiffness without the friction term, which is equal to Equation 2.14.

Then bulk modulus and shear modulus are given by

$$K_{dry}^{eff} = \frac{C_p(1-\phi)Ga}{3\pi R(1-\upsilon)} \tag{2.25a}$$

$$G_{dry}^{eff} = \frac{C_p(1-\phi)Ga}{5\pi R}[\frac{1}{1-\upsilon} + \frac{f_p 3}{2-\upsilon}(1-\frac{F_t}{\mu F_n})^{\frac{1}{3}}] \tag{2.25b}$$

The effective-bulk modulus could also be given by (Dufffaut et al., 2010)

$$K_{dry}^{eff} = \left(\frac{C_p^2(1-\phi)^2 G^2 p}{18\pi^2(1-\upsilon)^2}\right)^{\frac{1}{3}} \tag{2.26}$$

The Hertz model (Hertz, 1884) derived radius a as

$$a = \left(\frac{3F_n R(1-\upsilon)}{8G}\right)^{\frac{1}{3}} \tag{2.27}$$

Inserting Equations 2.25a and 2.27 into Equation 2.25b, the effective shear modulus of a random-granular packs is

$$G_{dry}^{eff} = \frac{3}{5}\left[1 + \frac{3(1-\upsilon)}{2-\upsilon} \cdot f_p \cdot f(\mu) K_{dry}^{eff}\right] \tag{2.28}$$

Then it is easy to get dry velocities of a random grain pack by combining Equations 2.26 and 2.28 with the known bulk density:

$$V_{p_{dry}} = \left(\frac{K_{dry}^{eff} + \frac{4}{3}G_{dry}^{eff}}{(1-\phi)\rho_m}\right)^{\frac{1}{2}} \tag{2.29a}$$

$$V_{s_{dry}} = \left(\frac{G_{dry}^{eff}}{(1-\phi)\rho_m}\right)^{\frac{1}{2}} \tag{2.29b}$$

2.3.5 Numerical examples

In this section, the elastic property of a random granular packs is numerically simulated with increased fraction of partial slip grain contacts, increased friction on the surface of grain contacts. To facilitate a reasonable comparison between our partial friction-heterogeneity model and the experimental glass-bead data of Domenico (1977), the porosity is assumed as 38.3% and the coordination number is 8.4, Table 2.1 shows the physical parameters of the silica glass.

Table 2.1: Physical parameters of silica glass

Parameters	Physical properties
ρ_g (g/cm^3)	2.42
μ_d (GPa)	29
υ	0.2

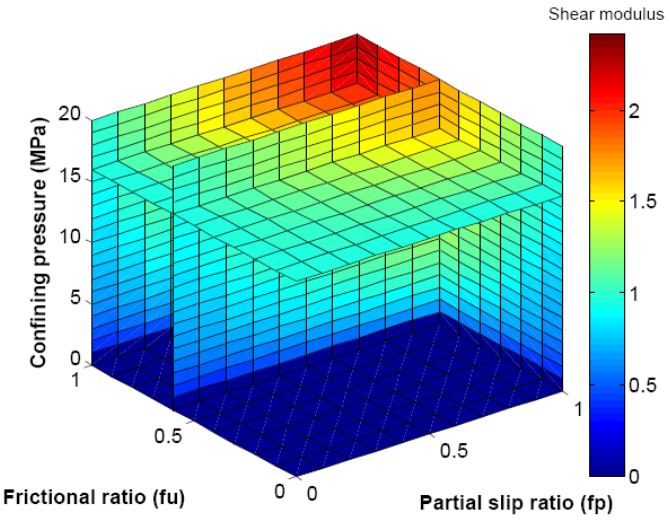

Figure 2.7 Shear modulus is a function of the partial slip parameter, friction term, and confining pressure.

Figure 2.7 displays the shear modulus, which is controlled by the fraction of partial slip taking place on the area of grain contacts, internal friction, and confining pressure. It is evident that the shear modulus increases as any above mentioned parameters increases.

e factors increase. It implies that micro-friction on the area of grain contacts is non-ignorable. In addition, tangential stress will cause partial sliding on the area of grain contacts, which leads to the heterogeneous-stress field.

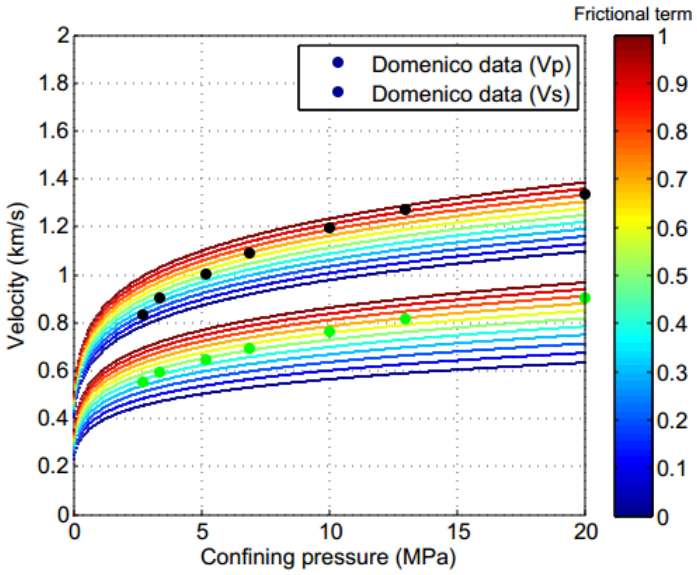

Figure 2.8 Velocities against confining pressure when the fraction of partial slip is 1.

For a special case of the occurrence of complete partial slippage, Figure 2.8 shows the velocities increase as confining pressure increases. In addition, the internal friction on the area of grain contacts simultaneously increases. The experimental data is located between a perfectly smooth boundary and an infinite friction boundary. The blue dots and green dots are Domenico's (1977) measurement data.

2.3.6 Discussion

Frictionless homogeneity case

If set $f_p = f(\mu) = 0$, it means that all grain contacts are frictionless, namely, $s_\tau = 0$, and the stress distribution is homogenous in the macroscopic scale, Equation 2.28 reduces to

$$G_{dry}^{eff} = \frac{3}{5} K_{d} \tag{2.30}$$

and

$$\frac{V_p}{V_s} = \sqrt{\frac{K_{dry}^{eff}}{G_{dry}^{eff}} + \frac{4}{3}} = \sqrt{\left[\frac{3}{5}\left(1 + \frac{3(1-\upsilon)}{2-\upsilon} f_p \cdot f(\mu)^{-1}\right)\right] - \frac{4}{3}} \tag{2.31}$$

$$\upsilon_{dry}^{eff} = \frac{5 - 2\left[1 + \frac{3(1-\upsilon)}{2-\upsilon} f_p \cdot f(\mu)\right]}{10 + 2\left[1 + \frac{3(1-\upsilon)}{2-\upsilon} f_p \cdot f(\mu)\right]} = \frac{1}{4} \tag{2.32}$$

Equations 2.30, 2.31, and 2.32 correspond to the equations of Marko (2009). Also, Equation 2.31 is analogous to Equation 4.21 of Walton (1987), which applies to the perfectly smooth case. So it is evident that the proposed partial friction-heterogeneity model is a generalized grain-contact model, which is consistent with all these special model cases.

Infinite roughness-heterogeneity case

Figure 2.9 is the effective shear modulus prediction of the partial friction-heterogeneity model when the fraction of partial slip grains is 1. As a consequence, Equation 2.28 reduces to Equation 29 of Duffaut's (2010). The black dot

and red dot indicate the infinite roughness case and the frictionless case of Walton's model (1987), respectively.

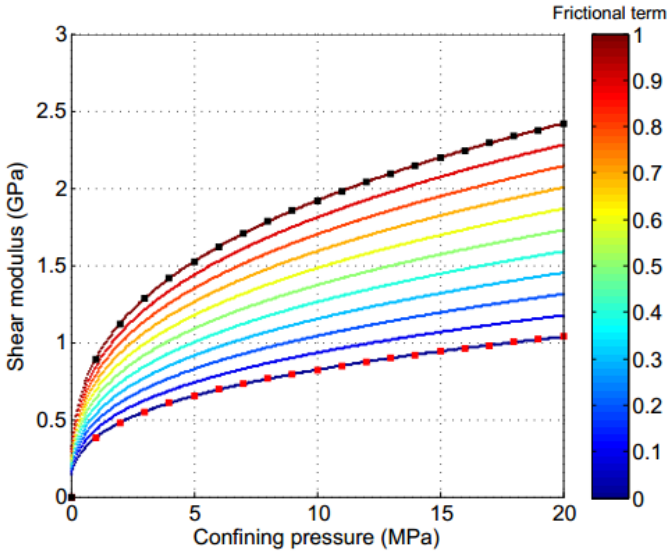

Figure 2.9 Effective shear modulus of partial friction-heterogeneity model when $f_p = 1$.

2.3.7 Conclusions

An explicit expression is proposed to combine the heterogeneous stress-distribution of each single grain in the macroscopic scale and the partial slip occurring on the area of grain contacts in the microscopic scale. By replacing the linear interpolation between frictionless smooth and infinite roughness-grain contacts, the partial friction-heterogeneity model involves Mindlin's nonlinear friction term, $f(\mu)$, to characterize the internal friction. The numerical simulations indicate that micro-friction on the area of grain contacts is non-ignorable, which results in the tangential loading path being irreversible.

The partial friction-heterogeneity model also indicates that an existing non-uniform stress-strain field, which is close to the truth, could cause partial grain sliding on the surface of grain contacts due to its force disequilibrium. Macroscopically, the effective shear modulus will be affected with the fraction variation of partial slip grain contacts.

The partial friction-heterogeneity model is a generalized grain-contact model, which is consistent with all special model cases. When $f_p = f(\mu) = 0$, it reduces to the frictionless-homogenous case. When the fraction of partial grains (f_p) is 1, it reduces to the case of homogeneous stress distribution in the macroscopic scale and nonlinear micro-friction on the area of grain contacts in the microscopic scale. When the friction term ($f(\mu)$) is 1, it reduces to the case of heterogeneous stress distribution in the macroscopic scale and infinite roughness on the area of grain contacts in the microscopic scale.

Chapter 3
Rock-physics modeling of depositional texture, diagenetic alternations in cemented sandstones

3.1 Abstract

An extended cement-contact model is formulated to characterize the effects of cementation thickness and cementation kind on the elasticity of sandstones, considering the geological digenesis from the weak phase (high-porosity) to the strong phase (low-porosity). The proposed rock-physics model indicates that cement thickness and cementation kind have an assignable influence on the elastic property of sandstone, with a thoughtful micro-mechanism interpretation.

3.2 Introduction

Sandstones are generally divided into two kinds. One is high-porosity unconsolidated sands, which constitutes initial stage of the depositional process and is likely to be found on the marine seabed. Since cementation does not exist, the grain-contact models (Mindlin, 1949; Brandt, 1955; Digby, 1981; Walton, 1987; Dvorkin, 1996; Bahrami, 2005; Xia, 2011; Deng, 2011; Liu, 2011) are utilized to investigate elastic property of unconsolidated sands. Another is cemented sandstones. The cementation from

chemical reactions and mineral dissolution significantly strength the unconsolidated sands. Dvorkin et al., (1994, 1995, 1996) and Avseth (2000) started to develop the cement-contact theory (CCT) to characterize the elastic properties of weakly cemented-sandstone, which generally has porosity between 25% and 36%, Figure 3.1.

With further cementation diagenesis, the differential-medium theory (DMT) gives excellent prediction of the elastic modulus whenever the porosity is negligible. However, when the porosity is not negligible, it is more difficult to use the DMT, because DMT is an inherent two-component approach. Allowing for two-solid constituents and also including porosity requires a three-component method. Either the Kuster-Toksoz model (KTM) or the self-consistent (SC) approximation is easily generalized to multiple components (Berryman, 1994).

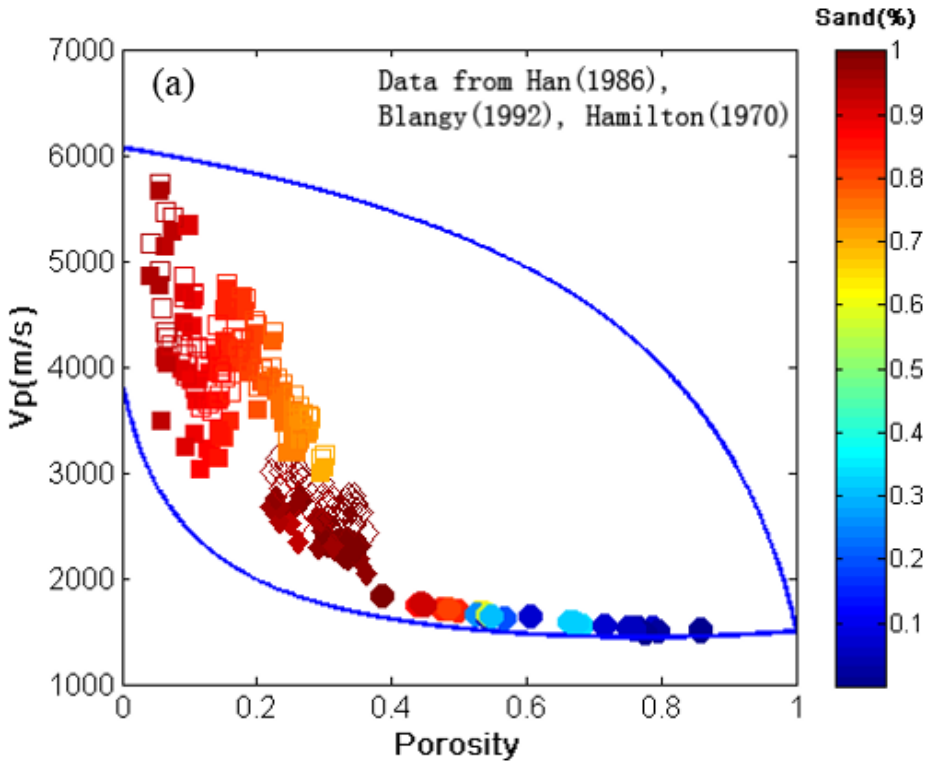

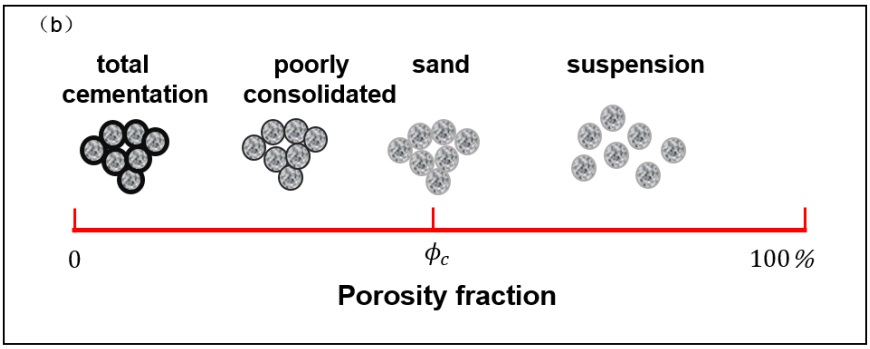

Figure 3.1 (a) P-wave velocity-porosity of sandstones; (b) A schematic of geological diagenesis of sandstones (after Nur et al., 1998).

Various well-known expressions (e.g., Voigt, Reuss, and the Wyllie's equation) do not consider the geological diagenesis of sandstones. Most models for poorly consolidated sandstone are based on CCT, which considers the physical interaction between the grains and cementation. Although the existing CCT models, to some degree, can delineate the elasticity of poorly consolidated sandstone, they have great deficiency in the modulus prediction. Therefore, with the consideration of the geological diagenesis of sandstone and the deposition environment, The CCT model will be modified to make more adequate and reliable.

This chapter is organized as follows: first, the extended cement-contact models are briefly reviewed. Second, the extended cement-contact model is derived. Third, extended CCT is used to analyze the effect of the cementation thickness on the elastic properties of loose sandstone with weak cementation. Finally, the discussion and conclusions are summarized.

3.3 Sandstone diagenesis

The instantly deposited sediments eventually evolve into consolidated clastic rocks with subject to physical, chemical, and biological factors. The combined effects of burial, bioturbation, compaction, and chemical cementation between grains, fluids, and organic matter ultimately determine the elasticity of clastic rocks. The sediments diagenesis encompasses all natural changes occurring from the moment of deposition continuing through compaction and lithification (de Segonzac, 1968). These post-depositional alterations take place at the relatively low pressure and temperatures conditions. As the depth increases, the increased pressures and temperatures promote further consolidation and cementation and ultimately form lithified rocks (Krumbei, 1942).

Both sedimentary and environmental factors are important to diagenesis of sandstone. Sedimentary factors include particle size, fluid content, and mineral composition. Environmental factors include temperature, pressure, and chemical conditions. At 70 ^{o}C, the mechanical compaction gradually transforms into predominantly chemical compaction in siliciclastic systems. For quartz-rich sands, initial cementation tends to start at the same depth. According to cement classification, Figure 3.2 shows that the sediments can follow two different path to form lithified rocks. For the path I, there is a distinct gap between the mechanical and chemical-deposition stage. In this path, the clay cementation may involve allogenic sources, which initially only undergo mechanical compaction at shallow depth. As the burial depth increases, the temperature and pressure increase until chemical compaction is triggered. Then chemical recrystallization,

cementation, and dissolution could occur to change the grain size and rock matrix. For the path II, due to the authigenic clays, unconsolidated sediments can simultaneously encounter both mechanical and chemical compaction.

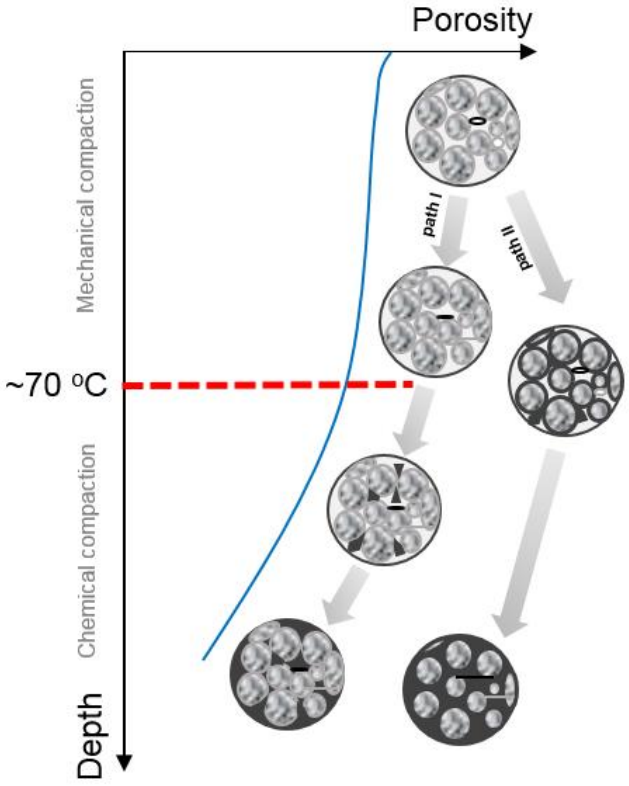

Figure 3.2 A schematic of sand-clay compaction.

3.3.1 Porosity evolution of sandstones

Diagenesis comprises all processes that convert raw sediments into sedimentary rocks (Worden and Burley, 2003). It is a continually active process, by which sedimentary mineral assemblages react to regain equilibrium in an environment, whose pressure, temperature, and chemical conditions are changing. These reactions can

enhance and modify porosity of sandstone, Figure 3.3.

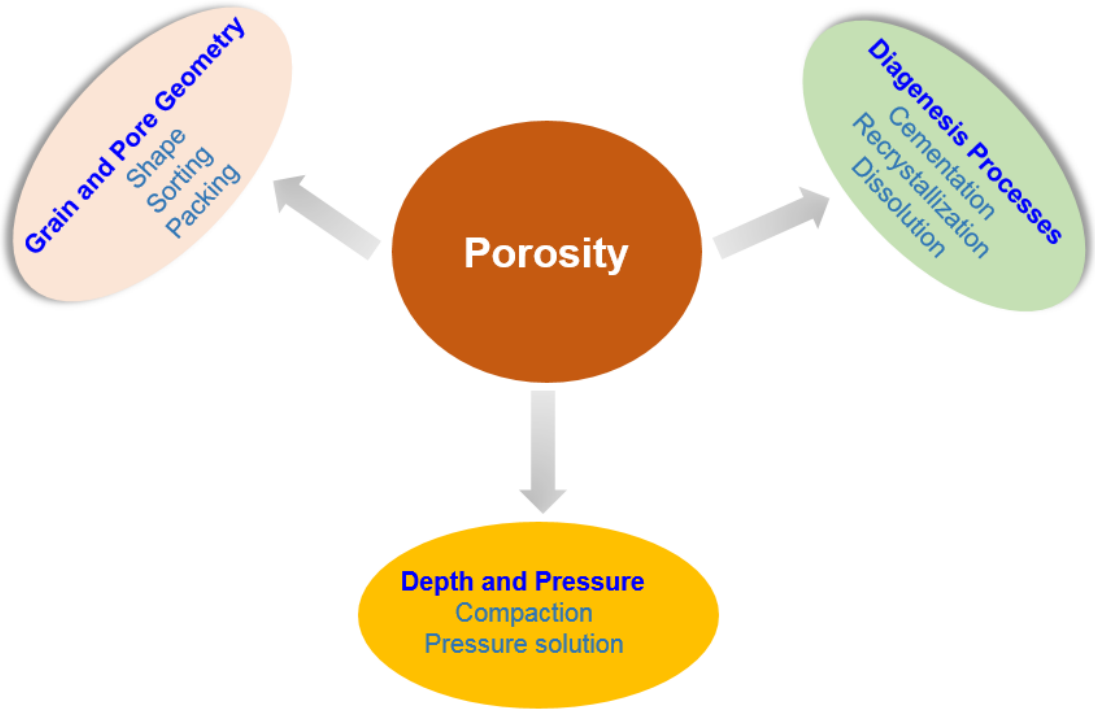

Figure 3.3 The factors that influence porosity during raw sedimentary diagenesis.

Sedimentary conditions initially control porosity at the time of deposition, but diagenesis subsequently alters it. Sedimentary supply controls sand deposition, and the energy of the transport medium affects the supply of coarser grains, in particular. Prior to the onset of diagenesis, sediment composition and the deposition conditions control porosity. Even before it is laid down, a sedimentary particle may undergo changes between its source and final deposition (Choquette and Pray, 1970).

3.3.2 Critical porosity of sandstone

Critical porosity is a key physical parameter that differentiates the mechanical and acoustic behavior of sandstone into two domains. As a readily observable macro-scale parameter, it is determined by the way of solid matrix and pore space are formed and is a more natural descriptor of the pore space. For porosity greater than critical porosity, the fluid phase is assumed to support the load, and the mineral grains behave mechanically in suspension, while for porosity lower than critical porosity, the mineral grains are load bearing. In the suspension region, the Reuss average describes the P-wave velocities quite well. However, the situation appears to be more complicated in the load-bearing region. Therefore, the effective-medium models and grain-contact models are proposed to characterize the elastic properties of sandstone. Sandstone generally has the critical porosity of $0.36-0.40$.

3.3.3 Clay types and their distribution

Clays are also important to the diagenetic process. They are responsible for easily compressible grains, cements, and pore-fillings. Clay distribution in pores could involve bond clay, matrix clay, clay fragments, pore-filling clay, float trace clay, and laminated clay. These clays are classified as allogenic and authigenic clays.

Allogenic clays originate as dispersed matrix, sand-to-cobble-sized mud, or shale clasts (Wilson et al., 1977). Individual clay particles may be dispersed throughout the sandstone or may accumulate to form thin laminate. Allogenic clays can also be introduced into sands as biogenic mud pellets, that is produced through ingestion and

excretion. The biogenic activity tends to homogenize the mud and sand, Figure 3.4. Authigenic clays develop within the subsequent burial-sand, chemical property of pore water and rock composition strongly influence the growth of authigenic clays.

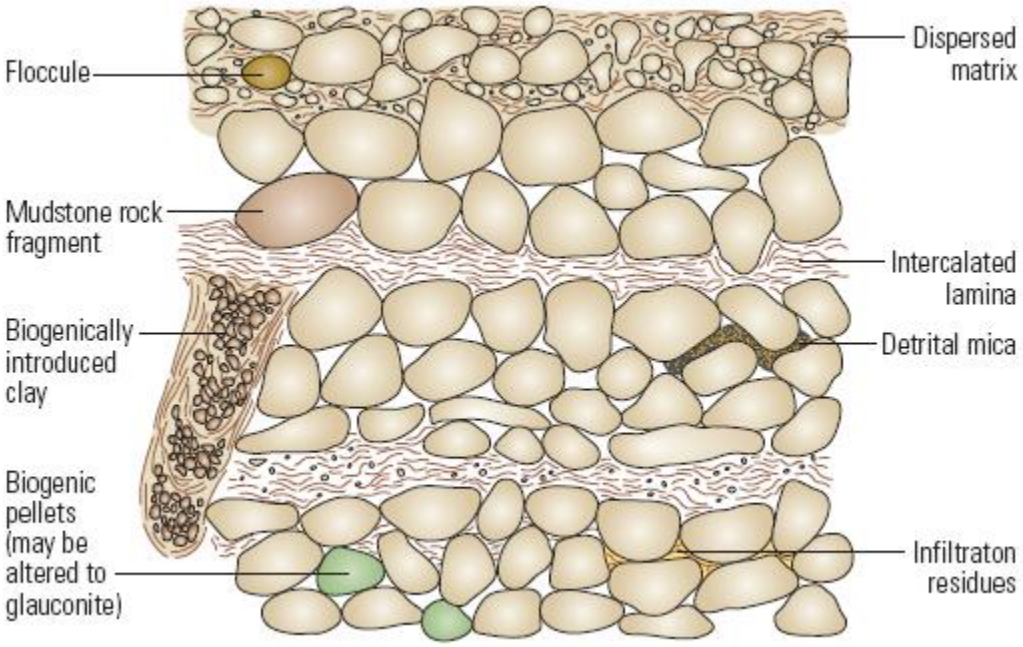

Figure 3.4 Allogenic clay sources. Sandstones may be infiltrated by a variety of detrital clays. (from Ali et al., 2010).

More importantly, it can be observed that clays exist in pore space in two forms. First, clay coatings can be deposited on the surfaces of grains except at points of grain-to-grain contacts. In the interstices between grains, the coatings act as pore-lining clay. These clays may be enveloped during subsequent cementation by feldspar and quartz overgrowths, Figure 3.5 (a), (Wilson et al., 1977). Second, clays only exist as pore-filling materials, which do not strength the rock frame, Figure 3.5 (b).

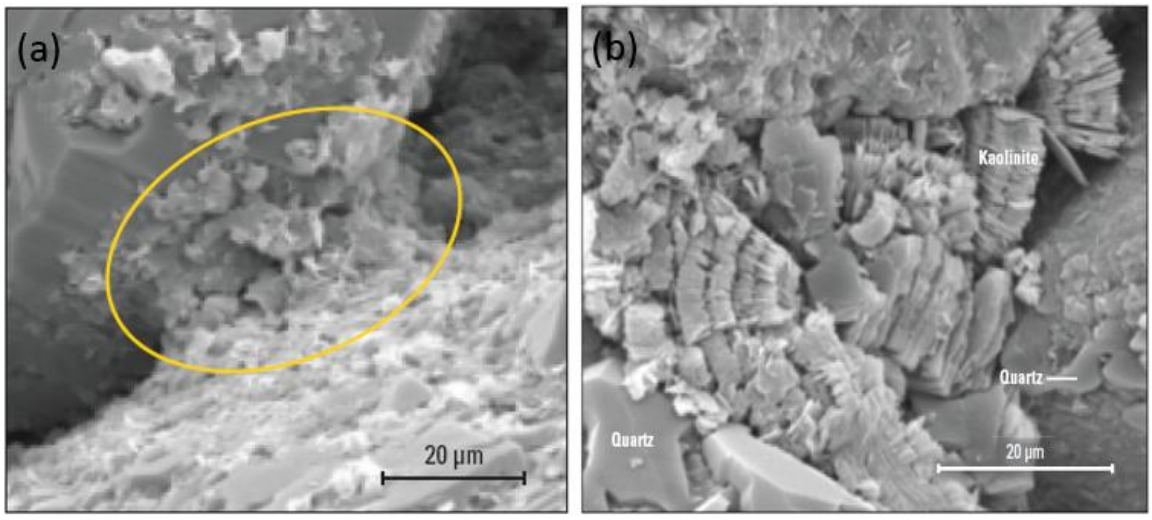

Figure 3.5 (a) Cemented clay in interstices between grains; (b) Pore-filling kaolinite in the pore space (Adapted from Ali et al., 2010).

3.4 Revision of rock-physics modeling on sandstones

Weakly consolidated sandstone bridges the regime between suspension and consolidated sandstone. Critical porosity is a key physical parameter that differentiates most clastic rocks' mechanical and acoustic behavior into two domains, Figure 3.6.

Based on our limited data and knowledge, we can observe a wide span of influences, such as rock texture, clay content, clay cementation, compactions, and anisotropic stresses, on the elasticity of sandstones. Researchers have separately studied the elasticity of sandstones based on their diagenesis stages. As we discussed in chapter 2, grain-contact models (Brandt, 1955; Walton, 1987; Digby, 1981; Noriss and Johson, 1997; Makse et al., 1999; Jenskin, 2005) are proposed to characterize elastic behavior of two elastic-spheres in contacts. As the diagenesis of sediments evolves, cementation effect is

more indispensable. Dvorkin (1994) introduced the CCT model to predict the elastic modulus of cemented sandstone. CCT model can only be utilized for a small amount of cementation. Therefore, the self-consistent (SC) and differential-effective medium (DEM) models are considered to delineate the elastic behavior of sandstone as the pore-filling materials keep merging into the pores.

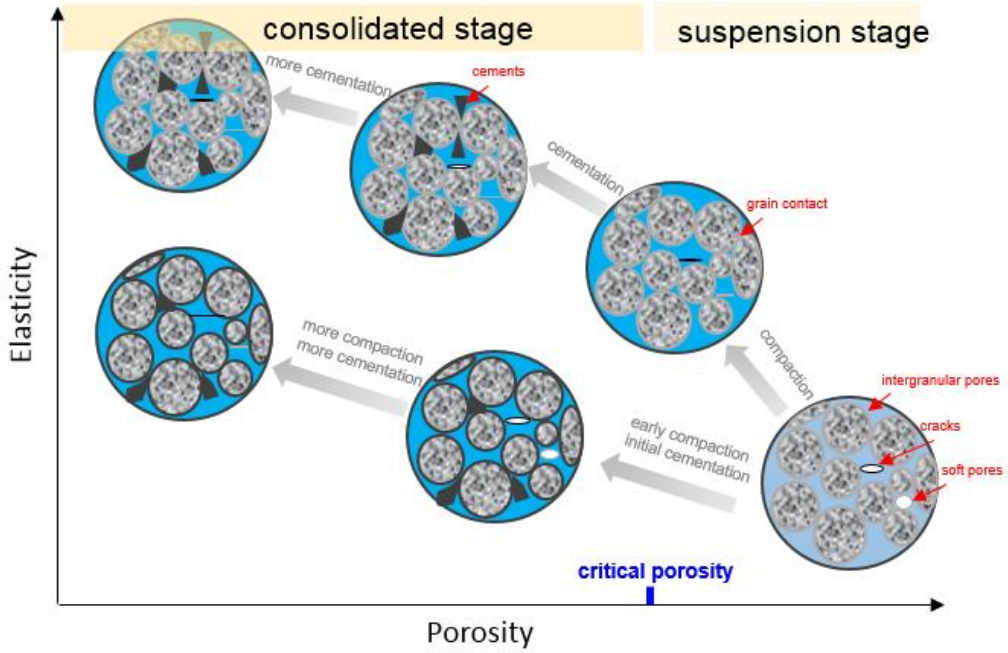

Figure 3.6 Sketch of elasticity of sandstones against porosity in different diagenesis stage.

3.4.1 Cement-contact model

The cementation theory (Dvorkin, 1994) predicted that even a small amount of cementation would reinforce the grain contacts, causing a large increment in the elastic modulus of cemented sandstone. The initial volume of cementation added in the pores

between grains is the most important. The effect of additional cementation placed around this initial cementation is relatively small. Several experiments have supported CCT prediction (Yin, 1993; Tutuncu et al., 1997). Even by adding cementation in the entire intergranular pore-space, it is not possible to achieve the high stiffness as small volumes of cementation at the grain contacts do (Dvorkin et al., 1994; Dvorkin et al., 1999; Yin, 1993; Tutuncu et al., 1997).

3.4.1.1 Stiffness of cement-contact model

Through the mechanic relationship between the grains and the cementation, the following expressions for normal stiffness S_n and tangential stiffness S_τ are derived (Dvorkin, 1994):

$$S_n = -\frac{4\pi R G_c (1-\nu_c)}{1-2\nu_c} \frac{k_n}{\Delta_n} \tag{3.1a}$$

$$S_\tau = -2\pi R G_c \frac{k_\tau}{\Delta_\tau} \tag{3.1b}$$

where $k_n = \int_0^\alpha \frac{H_n(t)tdt}{\varepsilon + t^2/2}$; $k_\tau = \int_0^\alpha \frac{H_\tau(t)tdt}{\varepsilon + t^2/2}$; R is the radius of the grain; G_c is the shear modulus of the cementation; ν_c is the Poisson's ratio of the cementation; k_n and k_τ are proportional to the normal force and tangential force, respectively; $H_n(t)$ and $H_\tau(t)$ are the normal and tangential deformation of the cementation, respectively; Δ_n and Δ_τ are the overall normal and tangential deformation, respectively; ε is the ratio of the cementation thickness to the radius of grain; α is the ratio of the cementation radius to the radius of the grain.

3.4.1.2 Effective modulus calculation

The bulk and shear modulus of cemented sandstone can be obtained from normal and tangential stiffness (Digby, 1981; Winkler, 1983; Mavko, 1998; Chen, 2001):

$$K_{eff} = \frac{n(1-\phi)}{12\pi R} S_n = \frac{G_c(1-\nu_c)}{1-\nu_c} \frac{C(1-\phi_0)}{3\pi(1+\varepsilon)} \left(-\frac{k_n}{\Delta_n}\right) \tag{3.2a}$$

$$G_{eff} = \frac{n(1-\phi)}{20\pi R}(S_n + \frac{3}{2}S_\tau) = \frac{3}{5}K_{eff} + G_c \frac{3C(1-\phi_0)}{20(1+\varepsilon)}\left(-\frac{k_\tau}{\Delta_\tau}\right) \tag{3.2b}$$

where n is the coordination; R is the radius of the grain; ϕ is the porosity of the cemented sandstone; K_{eff} and G_{eff} are the bulk and shear modulus of the cemented sandstone.

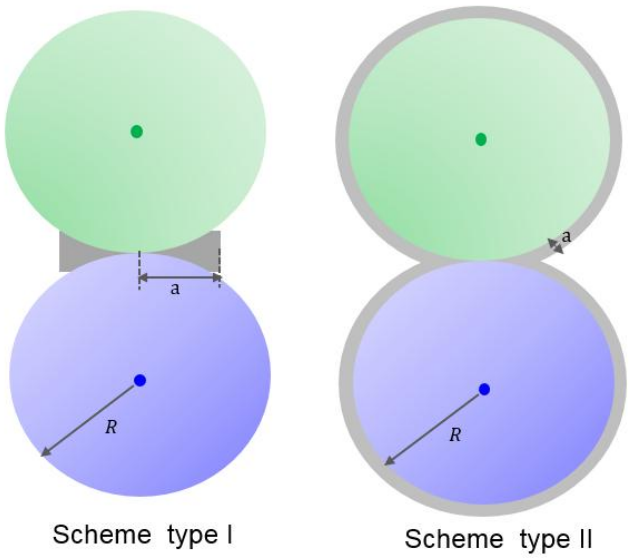

(a) (b)

Figure 3.7 Cemented grain contacts of conventional CCT. (a) Arrangement type I; (b) Arrangement type II.

Under the assumption that the cementation thickness is zero, Figure 3.7, two cementation types are given by

$$\text{Arrangement type I:} \quad \alpha = \frac{a}{R} = 2\left[\frac{\phi_0 - \phi}{3n(1-\phi_0)}\right]^{0.25} \tag{3.3a}$$

$$\text{Arrangement type II:} \quad \alpha = \frac{a}{R} = \left[\frac{2(\phi_0 - \phi)}{3(1-\phi_0)}\right]^{0.5} \tag{3.3b}$$

3.4.2 Stress distribution at the contacts

To understand stress transition among deformable particles through inter-particle bonds. Two-cemented grains are considered with cementation deposited around grain-to-grain contacts. Table 3.1 is the related physical parameters.

Table 3.1: The parameters for normal stress distribution in cementation with cemented materials.

Parameters	Values
Poisson's ratio($\upsilon_g = \upsilon_c$)	0.28
Cement thickness	0
Normalized radius	0.4
Density ($\rho_g = \rho_c$, g/cc)	2.3
Shear modulus ratio (G_c/G)	0.2; 0.4; 0.6; 0.8; 1.0; 1.2

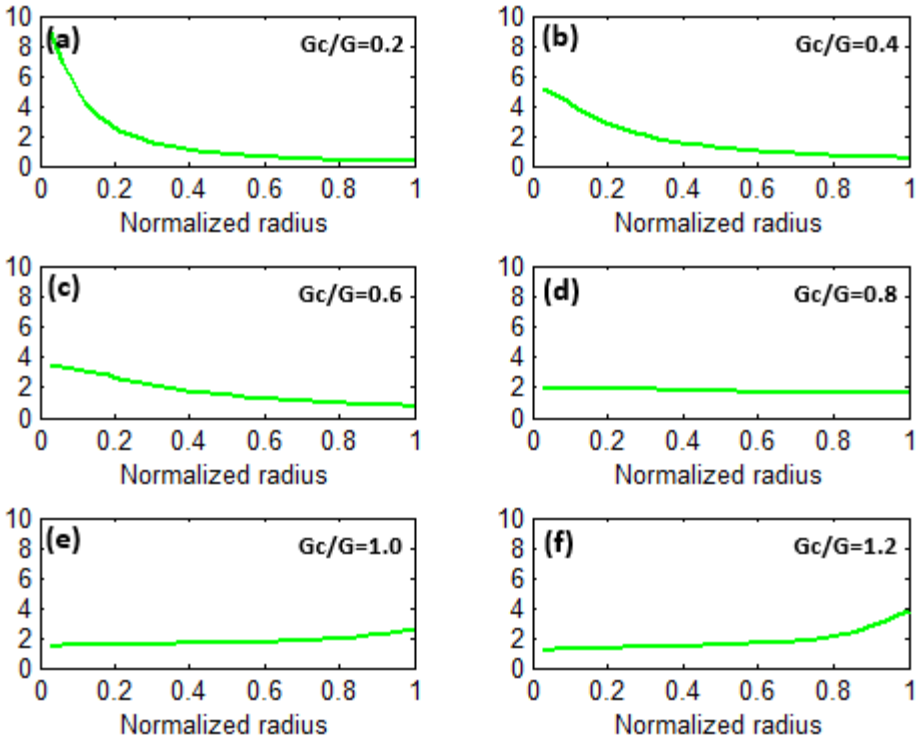

Figure 3.8 Normal stress distribution along the radius of cement layer. Stress (vertical axis) is normalized by the average stress. The horizontal axis is the normalized distance along the radius of the cement layer ($0 < r < a$).

Figure 3.8 shows that the stress is maximum at the center of the contact region when the cemented material is soft relative to the grain ($G_c/G = 0.2$), while the maximum stress gradually transits to the periphery when the cement material is stiffer ($G_c/G = 1.2$). In addition, the stress distribution provides us with important insight into the possible modes of inter-granular cementation failure: relatively stiff cementation yields at the periphery of a cement layer.

3.5 Extended cement-contact model

Considering the geological diagenesis of sediments evolving into sandstones, cement-contact model is extended to characterize the effect of cementation thickness on elastic properties of sandstones, Figure3.9. CCT model is only applicable for the direct grain-contacts with a few pore cements around them. To solve this issue, the effects of cementation thickness are mathematically considered.

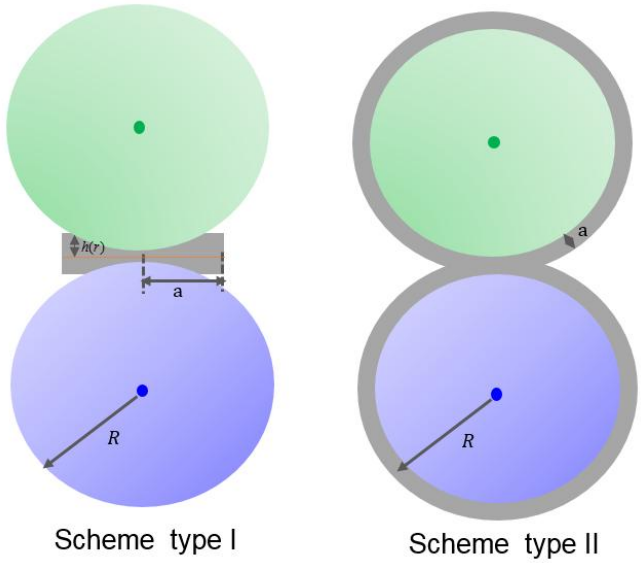

(a) (b)

Figure 3.9 Cemented grain contacts of extended CCT. (a) Arrangement type I with cementation thickness $h(r)$; (b) Arrangement type II with coating cementation thickness (a).

The detailed mathematical deduction is shown in Appendix A. For arrangement type I, the normalized radius is given by

$$\alpha = \sqrt{-2\varepsilon + 2\sqrt{\varepsilon^2 + \frac{4}{3n}\frac{\phi_0 - \phi}{1-\phi_0}}} \tag{3.4}$$

If assume $\varepsilon = 0$, then Equation 3.4 is simplified as

$$\alpha = 2\left[\frac{\phi_0 - \phi}{3n(1-\phi_0)}\right]^{0.5} \tag{3.5}$$

which is arrangement type I, as Dvorkin (1994) proposed.

For arrangement type II, the extended case is same as Equation 3.3b.

3.6 Numerical simulation

To evaluate the effect of the cementation thickness on the effective modulus of grain packs-cemented by different materials, the physical parameters of Table 3.1 is applied in numerical modeling. In addition, the range of the porosity is from 10% to 35%; the normalized cementation thickness varies from 0 to 0.05.

Table 3.2: The parameters for the host materials and variation in stiffness of cement materials (The parameters from Nur et al., 2009).

Parameters	Stiff cement	Soft cement
K_c (GPa)	38	1.5
G_c (GPa)	44	1.4
K_g (GPa)	38	38
G_g (GPa)	44	44
Initial porosity	0.36	0.36
Coordination number	8.5	8.5

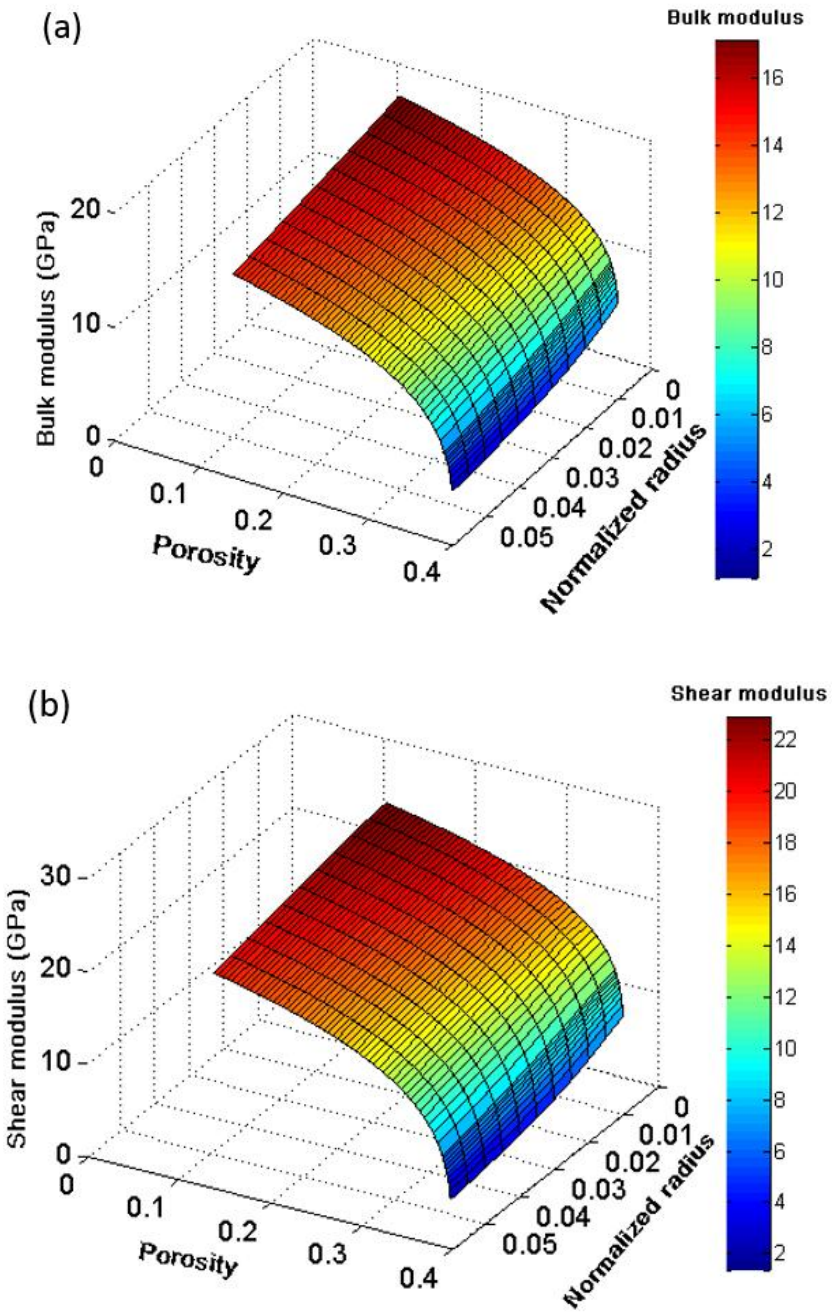

Figure 3.10 Effective modulus of cemented grain packs. (a) Bulk modulus of quartz-cemented grain packs with cementation type I; (b) Shear modulus of quartz-cemented grain packs with cementation type I.

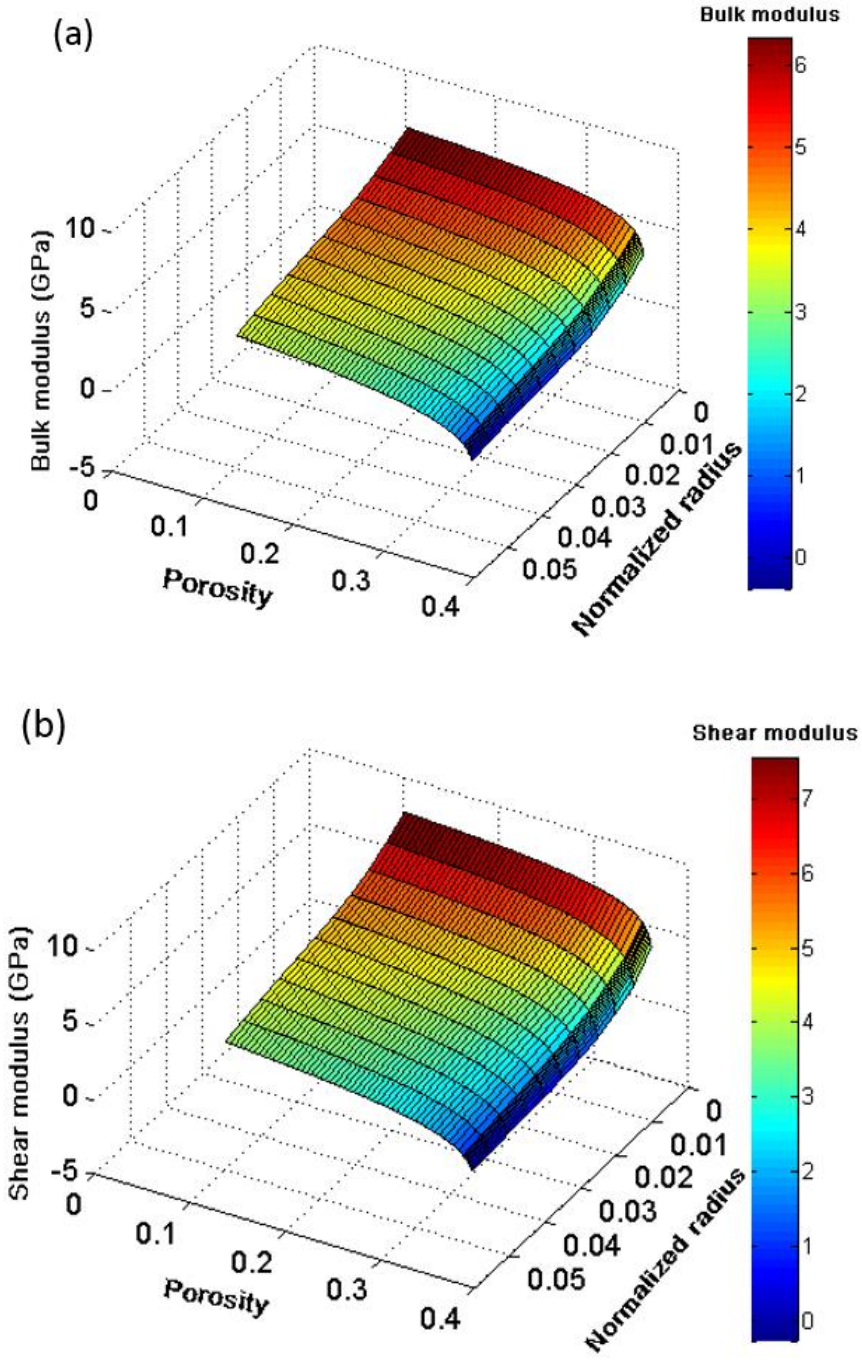

Figure 3.11 (a) Bulk modulus of clay-cemented grain packs with cementation type I; (b) Shear modulus of clay-cemented grain packs with cementation type I.

In the cement-contact model with non-zero thickness cementation between the grain contacts, both the bulk modulus and the shear modulus decrease as the normalized cementation thickness increases, Figure 3.10 and Figure 3.11. It is because that the normal and tangential stiffness decrease as the normalized cementation thickness increases. Both Figure 3.10 and Figure 3.11 indicate that the normalized cementation thickness has a significant impact on the elastic modulus when porosity is relatively high. It means that even a little cementation placed at the corner of grain contacts can dramatically increase the elastic modulus of grain packs (Dvorkin et al., 1994). With increased porosity, the effective modulus gradually increases. However, the increment is smooth. The numerical results show that the maximum modulus is observed when the normalized thickness is zero and the porosity is lowest.

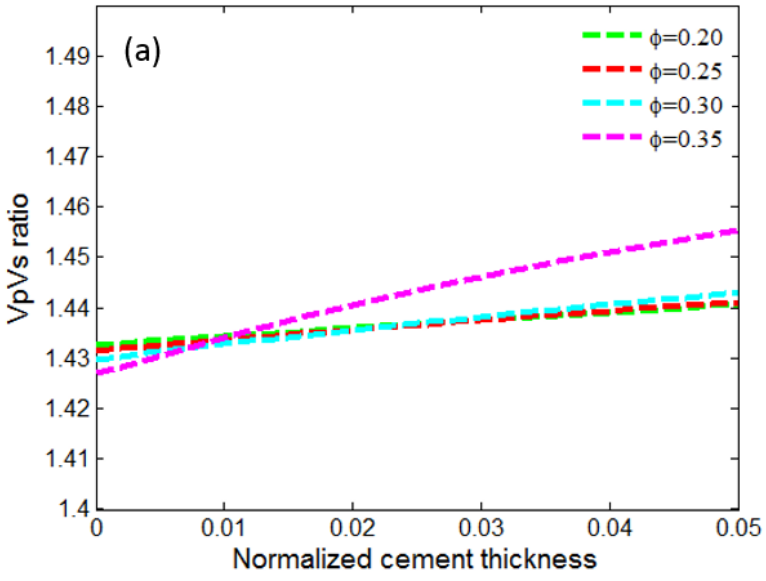

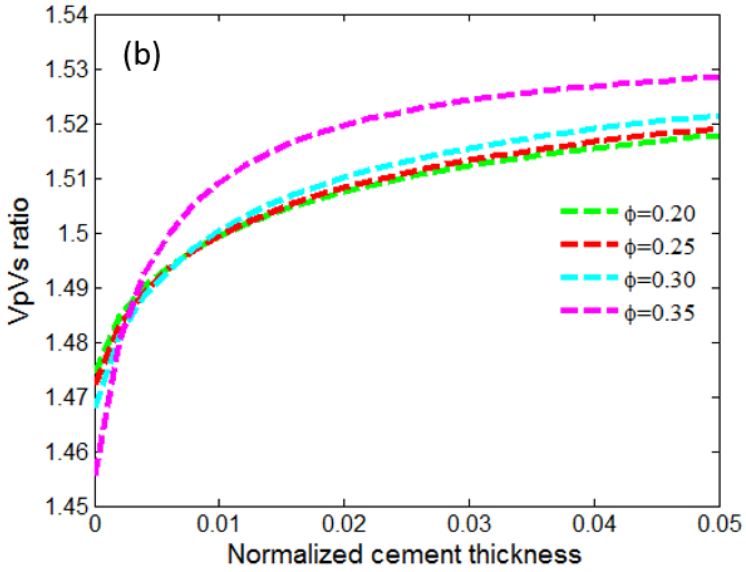

Figure 3.12 VpVs ratio against normalized cementation thickness for cement type I. (a) Quartz-cemented grain packs; (b) Clay-cemented grain packs.

Figure 3.12 (a) shows the VpVs ratio for the quartz-cemented grain packs gradually increases with the increment of normalized cementation thickness. Additionally, VpVs ratio is relatively high when the porosity is 35%. It means that the P-wave velocity increases dramatically with a little cementation. Figure 3.12 (b) shows that VpVs of clay-cemented grain packs increases significantly with a little cementation for the entire porosity-range, especially when the porosity is relatively high. It means that the soft-cement has an indispensable effect on both P- and S-wave velocities with a little cementation around the grain contacts.

3.7 Conclusions

The generalized cementation-radius expressions are derived to investigate the effect of cementation thickness on the elastic modulus of cemented sandstone. With the generalized cementation radius expressions, CCT cannot only be applicable to the pore-cemented loose sandstone but also to the loose sandstone with basal cementation.

Chapter 4
Partial water-saturation effect on velocity dispersion and attenuation of poorly consolidated sandstone at low frequencies

4.1 Abstract

The intrinsic velocity dispersion and attenuation, resulting from the relative movement between the pore fluids and the rock skeleton when seismic waves pass through, have been theoretically investigated. Considering the significant potential of velocity dispersion and attenuation in the reservoir characterization, the low-frequency measurements (2-800 Hz) are conducted for water-saturated sandstones. The measured results indicate that the degree of water-saturation and measured frequency have a significant impact on the elastic properties of sandstones. The water-saturated sandstone may demonstrate different relaxation mechanisms. If the macroscopic pore fluids have time to equilibrate at low frequencies, the Gassmann's equation is capable of modeling the response between the pore fluids and rock frame when the seismic waves pass through. However, it is possible to observe a substantial modulus increment as the measured frequencies. Moreover, as we observed, the different attenuation mechanisms may overlap. With the crossing of the relaxation times (frequencies) of different flow mechanisms, the attenuation approaches the peak and the elastic modulus (velocity)

increases most sharply.

4.2 Introduction

Seismic velocity dispersion and attenuation have been studied theoretically and experimentally for decades. Seismic wave passing through fluid-saturated porous rocks is subject to intrinsic dispersion and attenuation. The mechanical energy dissipates into heat (Aki and Richards, 1980). The intrinsic attenuation results from the relative movement between the pore fluids and the rock skeleton. It is broadly known as wave-induced fluid flow (WIFF) mechanism (Müller et al., 2010).

Attenuation is frequency-dependent. Gassmann's equation (1951) can be assumed as an extra low-frequency (relaxed status) case of WIFF theory. In addition, Biot (1956a, 1956b, 1962) studied the WIFF due to wavelength-scale pore-pressure equilibration and the resulting viscous-inertial attenuation. WIFF associated with wavelength-scale pressure gradients is often called global or macroscopic flow, whereas the "squirt" and "mesoscopic" flow are often termed local flow. The squirt flow typically emphasizes grain-scale heterogeneities such as loose grain contacts and micro-cracks that frequently take place in the reservoir rocks. In past decades, significant velocity dispersion and attenuation, mainly resulting from microscopic squirt flow, were experimentally observed at ultrasonic frequencies (Winkler, 1983, 1985; Murphy et al., 1984, 1986; Han, 1986; Jones, 1986; Batzle et al., 2006; Yao, 2014).

Many theories have been developed to make sense of the various dispersion and attenuation mechanisms, and many models have been proposed to estimate dispersion

and attenuation from other rock properties. However, none of the theories and models have received strong support from real measured data. The biggest issue is that velocity in seismic frequency cannot be measured directly in the laboratory. The early laboratory evidence of velocity dispersion is inferred indirectly from discrepancies between measured ultrasonic velocities and low-frequency Gassmann prediction (Gregory, 1976; Domenico, 1976; Gist, 1994). Attenuation is also obtained from ultrasonic data using the spectral ratio method (Toksöz et al., 1978) and Weiner filtering method (Tang et al., 1987). Although these early attempts gave robust evidence for the existence of dispersion and attenuation in sedimentary rocks at ultrasonic frequencies, it is not appropriate to transfer or apply that knowledge directly to well log or seismic data due to the large frequency differences among those datasets.

Efforts must be made to directly measure the velocity dispersion and wave attenuation in seismic frequency band. Winkler and Nur (1982) used the resonance-bar technique to measure the P-wave attenuation in sandstone at frequencies ranging from 0.5 to 9 kHz. The results suggested that attenuation mainly resulted from the partial saturation. Murphy (1982, 1984) and Yin et al. (1992) continued with the resonance-bar measurements and slightly expanded the frequency range to 0.3-14 kHz, making their results more meaningful for the well-log data interpretation. However, given constraints due to the size and geometry of the sample, it is impossible to extend the measurement into the seismic frequency range when employing the resonance-bar method.

The force-deformation method is an alternative technique for measuring the frequency-dependent velocity and attenuation in the seismic frequency range. This

method was originally designed and widely used in material science and mechanical engineering studies for measuring the static elastic constants of solid materials (Czichos et al., 2006). It was then developed into stress-strain hysteresis techniques to dynamically measure the frequency-dependent elastic constants, as well as the attenuation in granite and other anelastic solids (McKavanagh and Stacey, 1974; Peselnick et al., 1979). Spencer (1981) first succeeded in managing the measurements with a strain amplitude of around 10^{-6} and a frequency below 100 Hz in dry and water-saturated rocks. His results showed a strong dispersive modulus and the frequent dependency of Q^{-1} in water-saturated samples but not in dry samples. Liu et al. (1983) discussed the difficulties and challenges of carrying out such experiments under a small amplitude meaningful to in-situ seismic applications. Batzle and his group in the Colorado School of Mines (Gautam. 2003; Batzle et al., 2006; Adam et al., 2009; Das, 2009) further developed the techniques.

In this chapter, we will use the force-deformation principle to quantitatively measure the effect of partial gas-saturation on weakly consolidated sandstone at seismic frequencies. This chapter is organized as follows: first, it briefly reviews the dispersion and attenuation mechanisms. Second, it summarizes and analyzes the measurement principle and challenges of low-frequency apparatus. Third, the low-frequency measurement are conducted on the sandstone in partial water-saturation conditions.

4.3 Theory

4.3.1 Velocity dispersion and attenuation mechanism

Figure 4.1 shows that other mechanisms also cause velocity dispersion and attenuation, that may couple with the WIFF. If we do not consider the geometric spreading effects, wave-energy loss will result from intrinsic attenuation and elastic scattering. This chapter will focus on the effect of WIFF, as it is believed that the understanding of fluid-related dispersion mechanisms is inevitable.

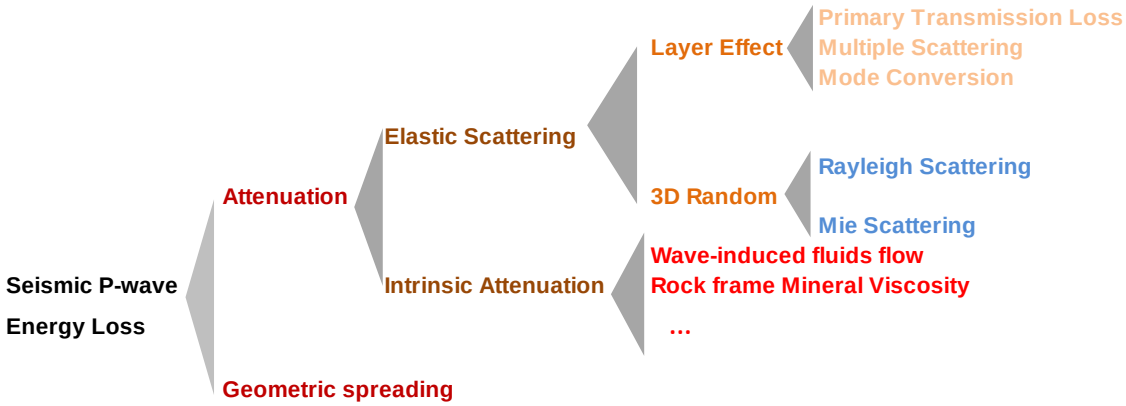

Figure 4.1 Seismic wave-energy loss mechanism (after Liner, 2012).

Multi-scale heterogeneities always coexist in a discrete manner or in a continuous manner since randomness and statistical fluctuation are the most prominent features of subsurface rocks in nature (O'Connell and Budiansky, 1974; Han, 2009; Yao, 2014). Consequently, the velocity dispersion behaves in a continuous manner, and many flow mechanisms can simultaneously take place over different frequency ranges, depending on the scale and hydro-physical properties of the geological features. Figure 4.2 schematically illustrates the possible relative positions of these different mechanisms and the associated geological features. Note that, when the open boundary condition occurs for the porous fluid-saturated system, the velocity can be even lower than that of the

Gassmann prediction.

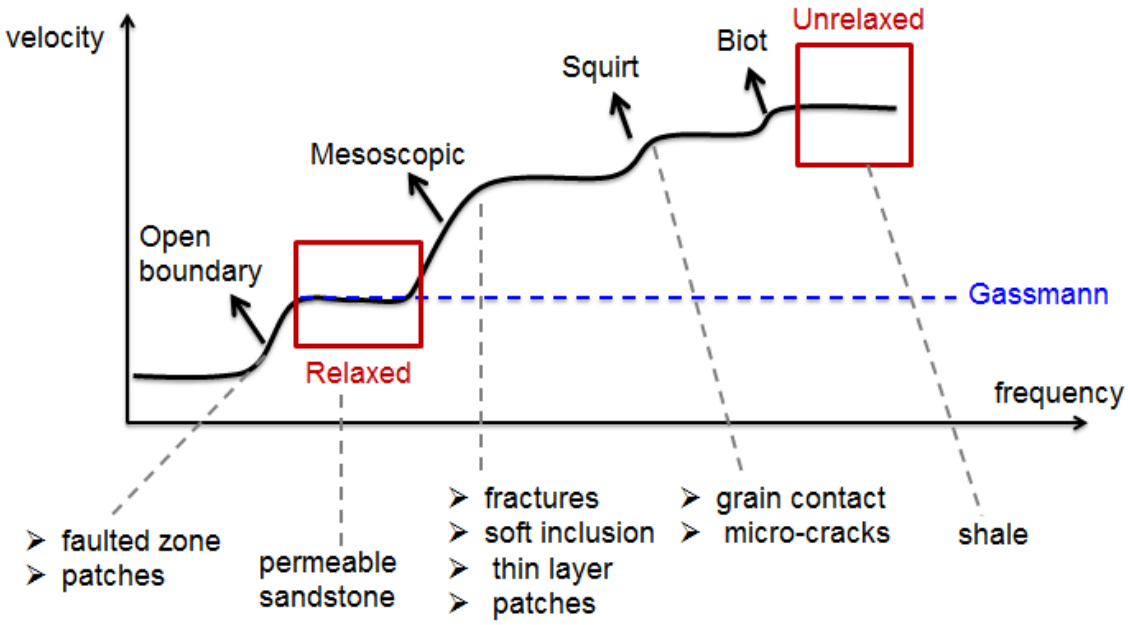

Figure 4.2 A schematic illustration of velocity dispersion associated with different mechanisms. The potential geological features that cause the flow are also listed in the corresponding positions (after Zhao, 2014).

4.3.2 Physical understanding of dispersion and attenuation mechanism

The percentage of water-saturation shall always be considered during the interpretation of the dispersion and attenuation mechanisms. Numerous mechanisms have been proposed to explain attenuation when the rock contains a low percentage of water (Bourbie, 1987). They are summarized as follows:

- The dissipation of energy by friction between grains, with the relative thickness of the layers of molecules absorbed influencing the “lubricating” effect.

- Breakage of chemical bands. Tittmann et al (1980) and Spencer (1981) suggested that the breakage of hydrogen bonds between the surface hydroxyls and the water molecules dissipates part of the energy. A strict interpretation of this hypothesis would lead to a close relationship between the specific surface hydroxyls and water molecules. However, it does not seem to have been verified experimentally so far.
- Capillary forces. In the case of very low-saturation with wetting fluid, the capillary forces may be very high and their disruption when the wave passes may cause the dissipation of energy. The capillary forces are dependent on the geometry of the pores than they are on the specific surface itself.

The precise mechanisms still need to be described. This necessitates expertise in the physico-chemistry of surfaces, because it is clear that the molecules-adsorbed on the solid surface of the rocks, particularly in the grain contacts and micro-cracks, play a predominant role.

4.3.3 Measured frequency and scale

Seismic velocity usually implies that the wave velocities are for frequencies between several Hertz and a few hundred Hertz, while ultrasonic or sonic velocity often refers to wave velocities spanning the frequency band of 10^5 to 10^6 Hz, Figure 4.3. Where clastic rocks are concerned, the geological processes and statistical fluctuation in geological history can cause sedimentary rocks to exhibit heterogeneities to various extents and at various scales (ranging from the micrometer grain and pore scale to the

many-kilometer basin scale), while the frequency of measured waves ranges from 1 Hz to 10^7 Hz. Correspondingly, scales and frequencies of geophysical measurements range from high frequency, millimeter wavelength in ultrasonic measurements to tens of meters of low frequencies. Undoubtedly, the integration of geophysical measurements at different frequencies aids in fully understanding the complexity of clastic rocks.

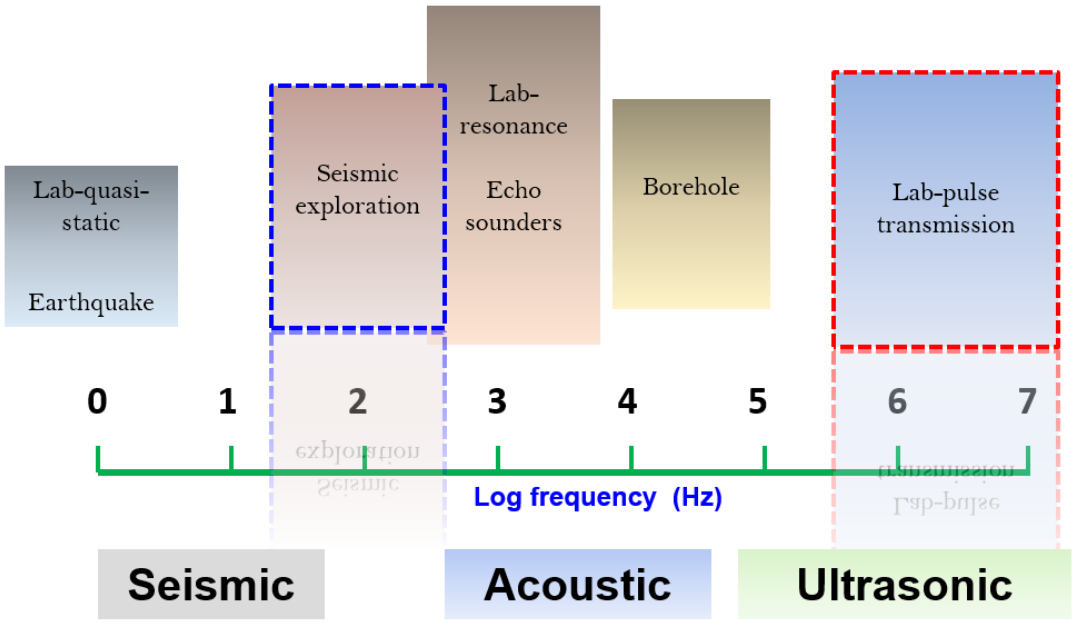

Figure 4.3 A scheme of scales and frequencies for variously geophysical measurement approaches.

Frequency-dependent waves propagating in fluid-saturated porous sandstone could cause scale-dependent intrinsic dispersion and attenuation, where the mechanical energy dissipates into heat (Aki and Richards, 1980). Figure 4.4 schematically shows the frequency-dependent intrinsic attenuation of compressional waves. For a single

relaxation mechanism, the P-wave velocity increases with the increased frequency, while the attenuation approaches the peak at the relaxation frequency, where the velocity increases rapidly. Fluid mobility, characterized by permeability, affects the pore-pressure equilibration time. Moreover, fluid viscosity is another key factor that influences the fluid motion. The two theoretical concepts most commonly used to tie velocity to viscosity are inertial coupling (Biot, 1965) and compliant pore coupling (O'Connell and Budiansky, 1977; Jones, 1986; Dvorkin and Nur, 1993; Berryman and Wang, 2000). Therefore, "relaxation" evidently does not guarantee occurrence at low-frequency. It is essentially related to the rock properties and fluid properties. Sandstone of high-porosity and high-permeability with high-mobility fluid states "relax" even at ultrasonic frequencies, while shale of low-porosity and low-permeability with low-mobility fluid states "un-relax" at seismic frequencies.

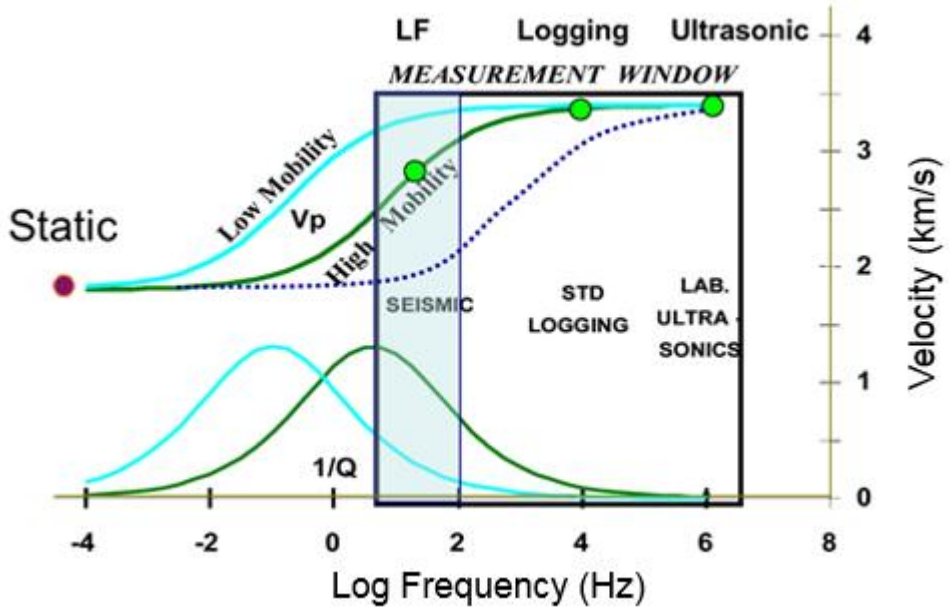

Figure 4.4 A schematic of the entire frequency-dependence of P-wave velocity and corresponding attenuation for partial fluid-saturation under both low and high fluid-mobility circumstances (after Batzle et al., 2006).

4.4 Principle of low-frequency measurement

The force-deformation method has long been applied in material science and structural engineering to measure the elastic strength of a wide range of materials. But those are in a static force with a relatively large deformation. Measurement using a dynamic force with a small deformation imposes new non-trial challenges. Early works (Spencer, 1981; Liu and Peselnick, 1983) presented some very attractive results and showed great potential of this method.

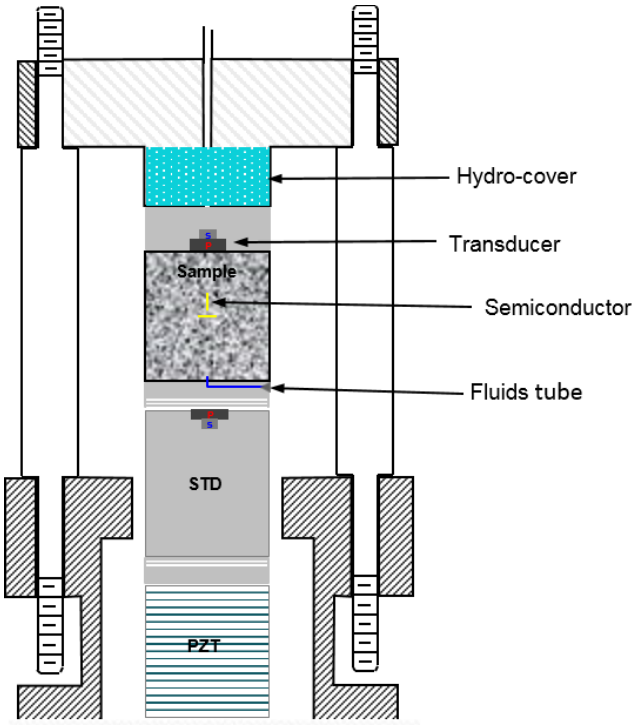

Figure 4.5 A schematic of low-frequency measurement apparatus.

Figure 4.5 is a schematic of low-frequency apparatus. The measured sample is placed in a pressure vessel, so that both the confining pressure and pore pressure can be focused on the sample. It is essential to manipulate it since quantitatively evaluating the effect of partial water-saturation on the velocity dispersion and attenuation of sandstone is our primary goal. A compressed nitrogen cylinder with a pressure regulator supplies the confining pressure. Currently, the maximum pressure reaches 2,000 psi in the measurements. A digital pump supplies and controls the pore pressure with various fluids as desired for experiment-specific purposes.

In predefined confining pressure, pore pressure, and saturation conditions, the function generator sends out a continuous harmonic voltage wave, with its frequency and amplitude specified by the user. This voltage signal is supplied to a linear power amplifier to obtain a harmonic current wave with the desired current level. The current drives a vibration to generate a harmonic mechanical vibration. The vibration deforms the sample and standard. The strain gauges attached to the surface of sample and standard detect both axial and radial strains dynamically. The Wheatstone bridges output voltage waveforms to a special weak-signal amplifier. The amplified waveforms are fed into a 24-bit, multi-channel AD converter. In addition, the original harmonic voltage wave from the function generator is fed into the AD converter. This waveform will be used as a reference signal in lock-in the amplifier.

4.4.1 Directly measured Young's modulus and Poisson's ratio

The principle of low-frequency measurement is based on Hooke's law. The two independent elastic constants (Young's modulus *E* and Poisson's ratio ν) are measured instead of velocities being measured directly under the assumption of isotropic media. Figure 4.6 is the schematic setup of sample stacking with standard. A sinusoid stress field is applied vertically to the core sample. Two sets of strain gauges are attached to the surface of the sample vertically and horizontally, which will measure the vertical strain $\varepsilon_{\perp}$ and horizontal strain $\varepsilon_{//}$. Young's modulus and Poisson's ratio are obtained as follows:

$$E = \frac{\sigma}{\varepsilon_{\perp}} \tag{5.1}$$

where σ is the vertical stress.

$$\upsilon = \frac{\varepsilon_{//}}{\varepsilon_{\perp}} \tag{5.2}$$

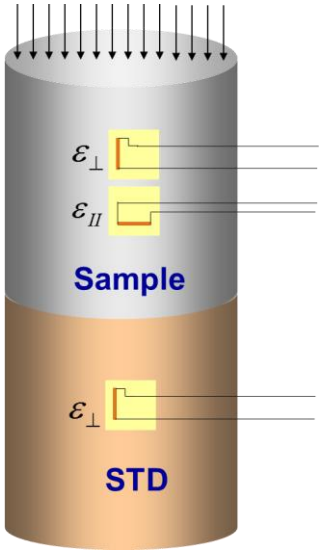

Figure 4.6 A schematic setup of sample stacking with standard.

In reality, a relative measurement strategy is applied instead of the direct measurement of force by stacking the elastic standard, which has a known Young's modulus, with the measured sample, Figure 4.6. The relative strain-amplitude measurement approach ensures that every measurement occurs under the same physical mechanism, with same electronic device and instrument and the same acquisition and processing procedures. This significantly reduces both the system and random errors. Since the standard and rock samples are subjected to the same stress field. Hence, Young's modulus is derived from the strain ratio of the standard to sample.

$$E_{sample} = E_{std} \frac{\varepsilon_{std}}{\varepsilon_{sample}} \tag{5.3}$$

It can be easily converted into bulk modulus *K*, and shear modulus *G* as follows:

$$K = \frac{E}{3(1-2\upsilon)} \tag{5.4a}$$

$$G = \frac{E}{2(1+\upsilon)} \tag{5.4b}$$

With a separated measured bulk density ρ, the P-wave velocity V_p and S-wave velocities V_s can be computed as:

$$V_p = \sqrt{\frac{K + \frac{4}{3}G}{\rho}} \tag{5.5a}$$

$$V_s = \sqrt{\frac{G}{\rho}} \tag{5.5b}$$

4.4.2 Attenuation: phase difference

Tokoz and Johnston (1981) gave a comprehensive summary on the attenuation and quality factor. Complex modulus M is mathematically introduced to describe stored and dissipated energy. It can be expressed as the real part M_R and the imaginary part M_I:

$$M = M_R + iM_I \tag{5.6}$$

The inverse-quality factor Q is defined as the ratio of the imaginary M_I and real M_R of the complex modulus. It can also be physically understood as the phase difference between the applied stress θ_σ and measured strain θ_ε (White, 1983; Paffenholz and Burkhardt, 1989):

$$\frac{1}{Q} = \frac{M_I}{M_R} = \tan(\theta_\sigma - \theta_\varepsilon) \tag{5.7}$$

Purely elastic material is not attenuated. Therefore, the phase difference between stress and strain is 0, and the quality factor is theoretically infinite. The sedimentary rock can be characterized as viscoelastic materials with a finite, non-zero quality factor. Experimentally, if the phase of the applied stress and induced strain can be separately measured, then applying Equation 5.7 calculates the quality factor of the sample. Due to the application of the relative measurement, Young's quality factor Q_E can be calculated by the measured phase θ_{std} of the standard and the phase θ_{sample} of the sample.

$$\frac{1}{Q_E} = \tan(\theta_{std} - \theta_{sam}) \tag{5.8}$$

The quality factor for the P- and S- wave can be obtained using the following relationships (Gautam, 2003):

$$\frac{1}{Q_S} = \frac{1}{Q_E} - \frac{\nu}{1+\nu}\tan(\theta_\nu) \tag{5.9}$$

$$\frac{(1-2\nu)(1-\nu)}{Q_P} = \frac{1+\nu}{Q_E} - \frac{2\nu(2-\nu)}{Q_S} \tag{5.10}$$

θ_ν is the phase difference between Poisson's gauge (horizontal) and Young's gauge (vertical).

4.4.3 Cole-Cole modeling

Kramer-Kronig (Bourbie et al., 1987) linked modulus dispersion and attenuation. No dispersion means no attenuation. Conversely, attenuation will result in

frequency-independent elastic properties (Dvorkin, 2005). The largest attenuation will occur at the frequency, where the change of modulus is maximum. The theoretical models, such as the constant-Q model, the Cole-Cole equation, etc., are proposed to link the modulus dispersion with attenuation. The Cole-Cole model couples dispersion and attenuation by a real M_R and imaginary M_I part of a modulus:

$$M(\omega) = M_R(\omega) + M_I(\omega) = M_\infty + \frac{M_0 - M_\infty}{1 + (i\omega\tau)^{1-k}} \tag{5.11}$$

where τ is the relaxation time and k is a distribution parameter that controls the relaxation range. M_∞ and M_0 are the infinite modulus and zero frequency modulus, respectively.

As a model characterizes the behavior of one single attenuation mechanism, the Cole-Cole model is applied to fit the measured data of fluid-saturated porous rocks. Figure 4.7 (a) shows an example of the Cole-Cole model with $M_\infty = 38.5$ GPa, $M_0 = 20$ GPa, and relaxation time $\tau = 10^{-5}$ s. Evidently, the low-frequency and high-frequency limits are independent of the distribution parameter when it varies from 0.2 to 0.6, but the rate of change of the modulus is largely dependent. The larger distribution ($k = 0.6$) results in a lower change rate for the modulus over a broad frequency range, while the small distribution ($k = 0.2$) results in a steeper modulus change over a narrow frequency range. Since the magnitude of attenuation, measured as inverse Q in Figure 4.7 (b), is directly related to how intensely the modulus varies, it is no surprise that the largest attenuation occurs when $k = 0.2$.

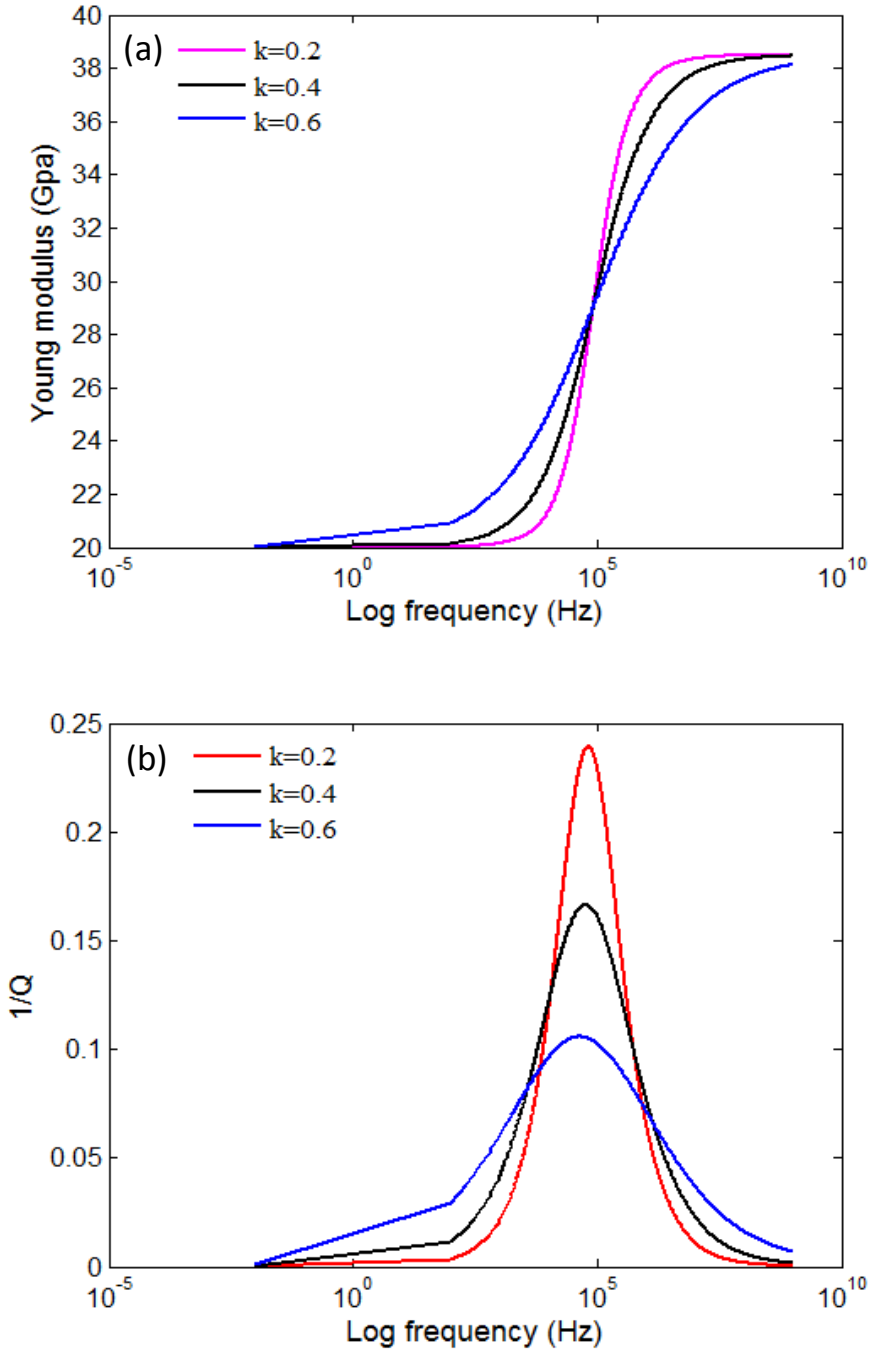

Figure 4.7 An example of Cole-Cole modeling. (a) Young's modulus against frequency; (b) Inverse-quality factor against frequency.

4.5 Measurement challenges

The primary challenges come from the output signals of weak-strain gauge, quality of sample preparation, and quality of mechanical assembling.

4.5.1 Low-strain amplitude

Because the elasticity of seismic strain amplitude is less than 10^{-6} in the far field, Figure 4.8, it requires us to perform low-frequency measurement at the same magnitude of strain amplitude, within seismic frequencies range. As a result, performing the force-deformation measurement for the small strain ($\varepsilon < 10^{-6}$) is technically challenging. Low-frequency apparatus at the University of Houston's Rock Physics Laboratory is in a frequency range of between 2 and 1000 Hz, with a measured strain amplitude less than 10^{-7}. Therefore, the low-frequency apparatus allows us to perform the measurements at the seismic strain-amplitude level over a large frequency band (2-800 Hz). Combination with ultrasonic measurements of the same strain amplitude but high-frequency (1000 kHz) enables us to characterize the possible dispersion and attenuation mechanism over all frequencies.

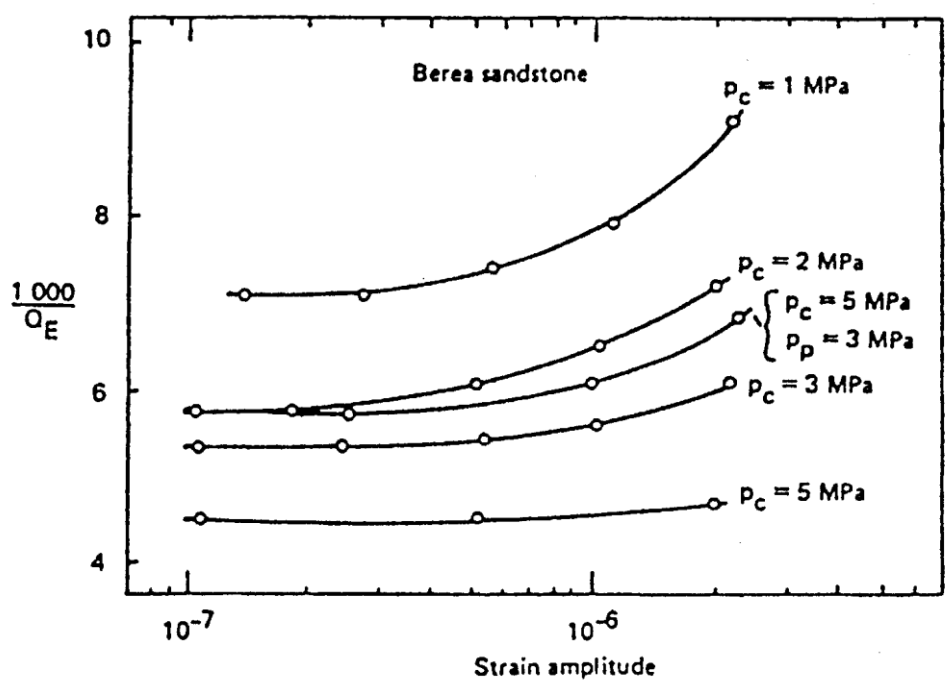

Figure 4.8 Strain amplitude and attenuation in rocks (from Winkler et al., 1979).

4.5.2 Low signal-to-noise ratio

In order to mimic the dynamic seismic strain amplitude ($\varepsilon < 10^{-6}$) in the laboratory, the output signal of strain amplitude only reaches 10^{-8} in practical measurement in our case. Consequently, the strain gauge's Wheatstone bridge output is only in the micro-volt range, which is very easy to contaminate with environmental electromagnetic noise. Therefore, special care has to been taken, where the hardware (wiring, shielding, grounding), AD conversion (high resolution), and software (signal processing, and measurement automation) are concerned for the acquisition and retrieval of the signal (Yao, 2014).

4.6 Accuracy analysis

In order to measure consistent results, four semi-conductors are attached on surface of the sample, placed at 0^0, 90^0, 180^0, and 270^0. Figure 4.9 shows the measured strain amplitude.

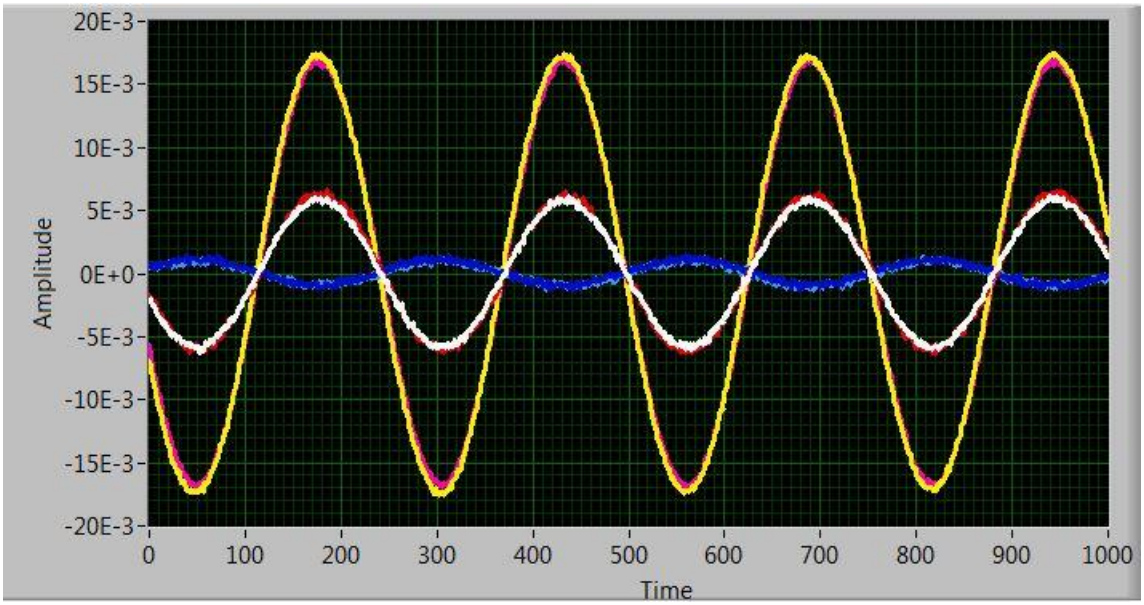

Figure 4.9 Measured six-channel signals at 400 Hz. White and red is the Young's strain-amplitude of the standard; yellow and pink is the Young's strain-amplitude of the sample, which is used to calculate Young's modulus of the sample; blue and light blue is the Poisson's ratio strain-amplitude of the sample, which is applied in the calculation of Poisson's ratio.

Accuracy and reliablity of laboratory measurement is important in the evaluation of data quality. The measured strain amplitude of both the standard and sample are a key to calculate the Young's modulus, while the phase difference between the applied stress and

induced strain is applied to calculate attenuation. Therefore, the electrical system error, and random error including sample preparation and sample setup, are analyzed first before conducting any field-sample measurement. Figure 4.10 (a) shows the strain-amplitude ratio of the sample (aluminum) extracted from single Young's gauge, while Figure 4.10 (c) shows the corresponding phase difference. Theoretically, the strain-amplitude ratio and phase difference are extracted from single strain guage shoubd be 1 and 0, respectively. For our low-frequency apparatus, the electrical system only causes a maximum error of 0.2% in the strain-amplitude ratio, and the distinguished phase difference is 0.05^{o} (corresponding $Q = 1146$). On the other hand, the sample preparation and setup will inevitably cause additional error due to the surface coupling, flatness, and strain-gauge tolerance. Figure 4.10 (b) shows the strain-amplitude ratio of Young's gauge between the standard (titanium) and sample (aluminum) reaches 0.984 at least. It means that the total errors, including electrical system error and sample-prepartion error and setup error are still less than 5%, which is the tolerance of strain gauge. Correspondingly, the system can distinguish the minimum phase difference of 0.12^{o}, which corresponds to maximum quality factor of 477.

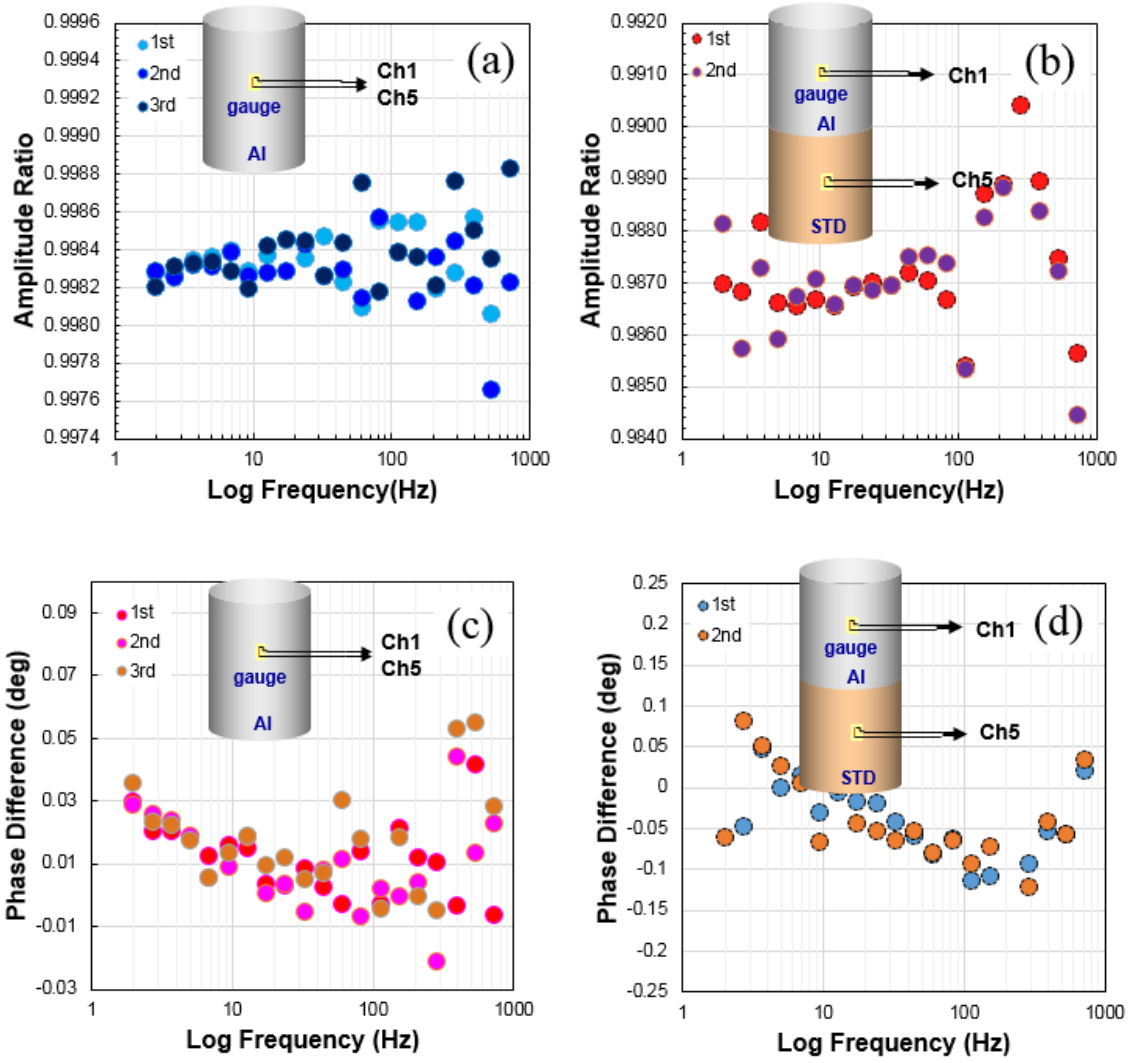

Figure 4.10 (a) Strain amplitude ratio against frequency for single Young's gauge on aluminum; (b) Strain amplitude ratio against frequency for Young's gauge attached on the surface of standard and sample, respectively; (c) Phase difference for single Young's gauge on aluminum; (d) Phase difference for Young's gauge attached on the surface of standard and sample, respectively.

4.7 Calibration of low-frequency system

In order to calibrate the low-frequency system firstly, the measurements are conducted on known modulus materials (aluminum, $E = 69GPa$) using the static method (0 Hz), force-deformation principle (2-800 Hz), and ultrasonic measurement (10^6 Hz) to verify the stability and reliability of low-frequency apparatus. Since aluminum is purely elastic, it offers no response to the frequency, Figure 4.11. Evidently, Young's modulus of aluminum over all frequency band is constant. Figure 4.12 shows that quality factor of aluminum is very high, that indicates that aluminum is purely elastic.

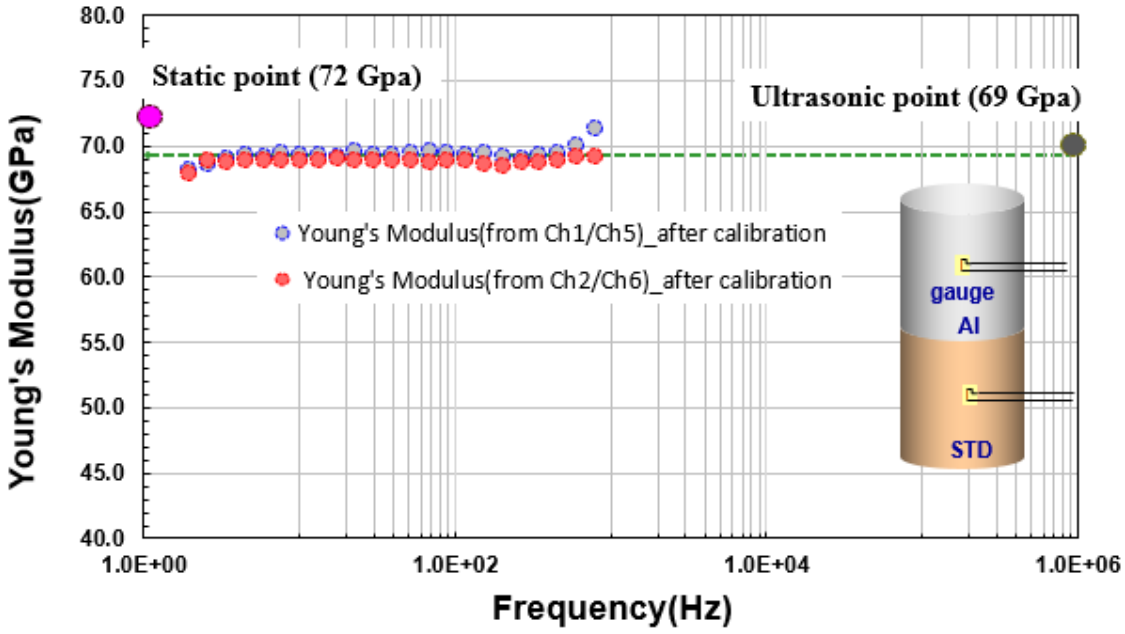

Figure 4.11 The Young's modulus of aluminum, measured by the static method (0 Hz), force-deformation principle (2-800 Hz), and the ultrasonic measurement (10^6 Hz).

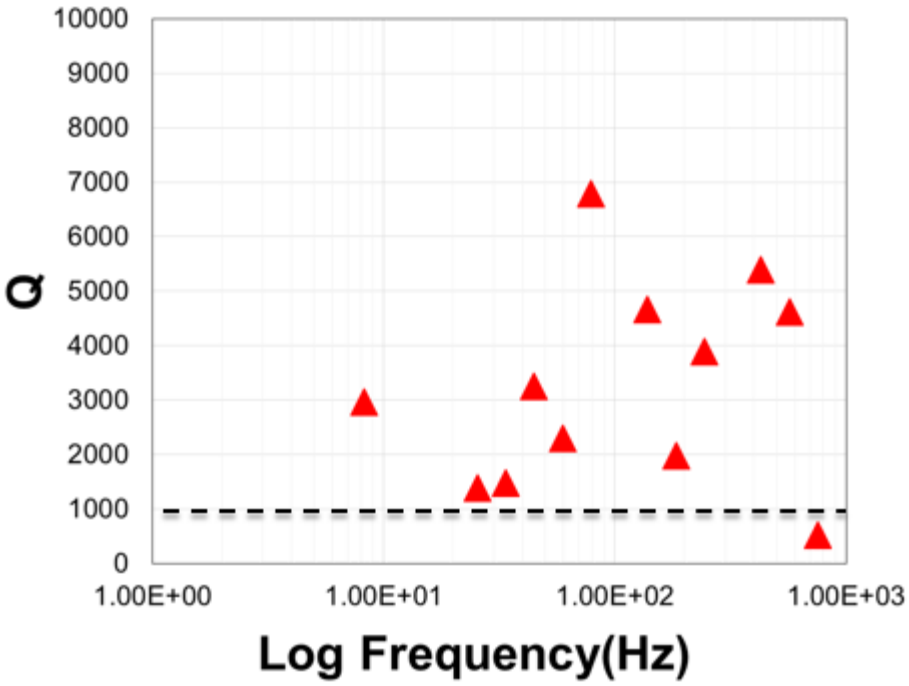

Figure 4.12 Quality factor of aluminum.

4.8 Low-frequency measurement on field sandstones

4.8.1 What is "dry" rock?

The "dry" rock generally refers to the following four states (Bourbié et al., 1987):

- "Moon-dry" refers to a sample without adsorbed water; the attenuation is very low, typically $Q > 2000$.
- "Vacuum-dry" refers to adsorbed fluid that, even in small quantities, is sufficient to cause a relative drop in attenuation ($100 < Q < 1000$).
- "Room-dry" refers to the humidity of the ambient air. Although it is hard to measure with ordinary equipment, it allows water to be adsorbed in sufficient quantities to disrupt the value of attenuation.

- "Wet-air" refers to a rock that has remained in conditions with a high degree of humidity for a long time. The saturation may reach several percentage. Therefore, the attenuation value is generally higher than those in previous cases.

4.8.2 Sample description

The high-porosity sandstone is measured in this section. Table 4.1 lists an overview of rock properties. Total porosity is measured from the bulk and grain volume using Boyle's law. Steady-state gas-permeability measurements are performed at the confining pressure of 600 psi.

Table 4.1: The basic properties of sample #2.

Parameters	**#2**
W (g)	106.37
L (cm)	4.86
D (cm)	3.77
Porosity	24.8%
Permeability (md)	866
Grain density (g/cc)	2.60
Bulk density (g/cc)	1.96

4.8.3 Low-frequency measurement under room-dry conditions

The low-frequency measurement is first performed with different confining pressures under room-dry conditions. The valve, placed at the pore-pressure line, is closed during the measurement. Hence, it is un-drained condition. In other words, it is no fluid communication (if it exists) between the porous sample and pump tank during the

low-frequency measurements.

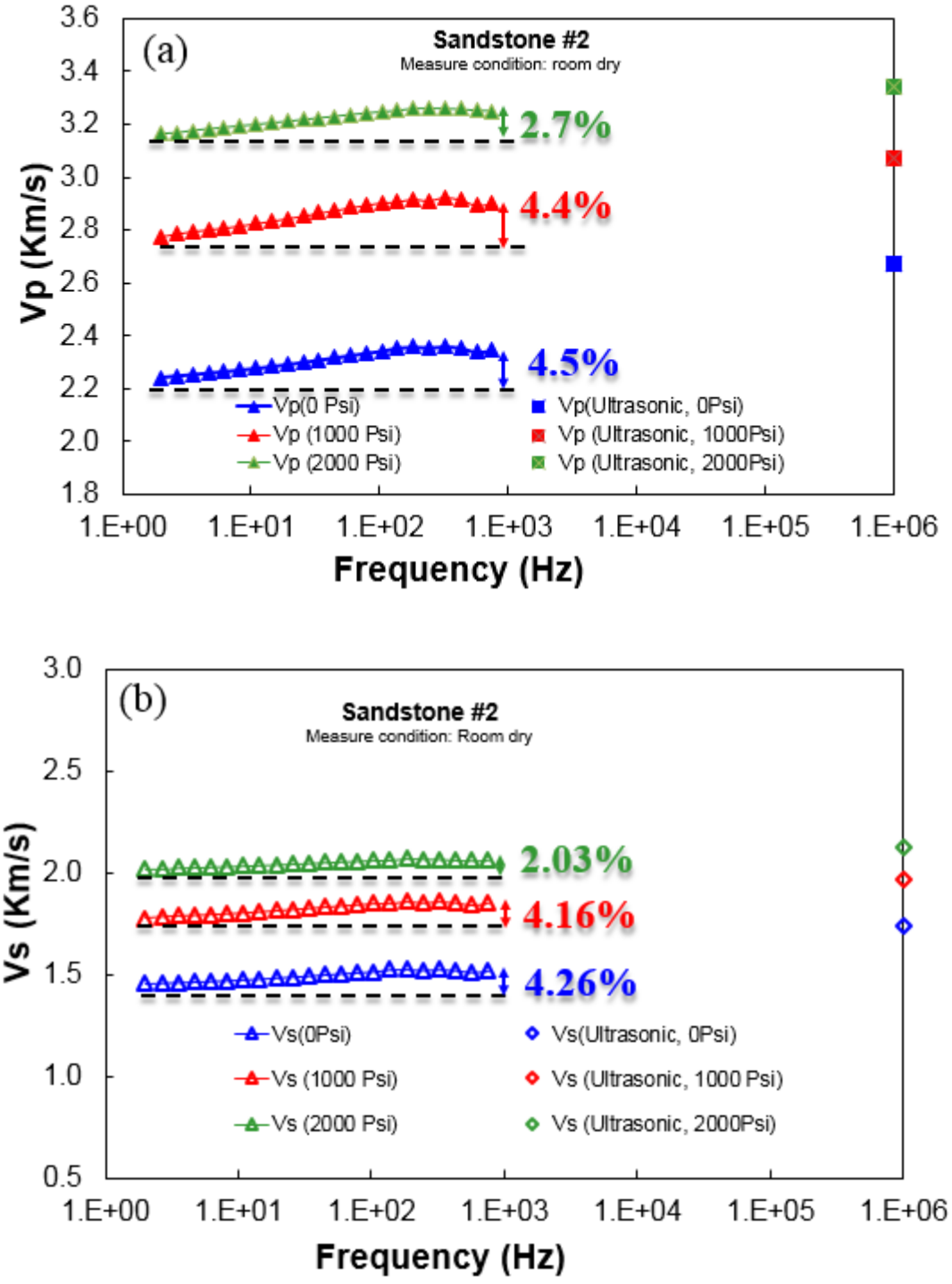

Figure 4.13 Converted P-wave and S-wave velocities against frequency for sample #2

under room-dry conditions

In Figure 4.13, converted P-wave and S-wave velocities increase gradually with increased frequency. Moreover, the velocities continue to be dispersive until they reach the ultrasonic points under the same differential pressure condition. In addition, both the P-wave and S-wave velocities are sensitive to the confining pressure over low-frequency band and ultrasonic frequency. The velocity dispersion decreases gradually with the increased differential pressure, Figure 4.13.

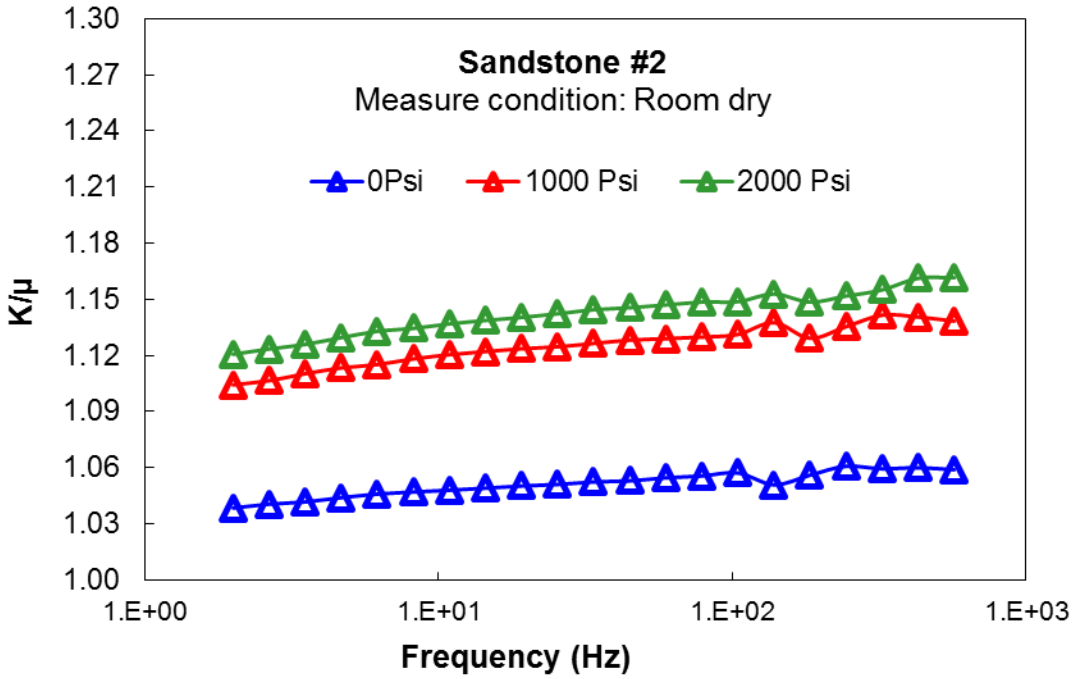

Figure 4.14 Ratio of converted bulk modulus and shear modulus against frequency for sample #2 under room-dry conditions

Since the fluid-flow-related dispersion is mainly reflected in the bulk modulus than

shear modulus, hence, measured Young's modulus and Poisson's ratio are converted into the ratio of bulk and shear modulus, which increases slightly with increases frequency because of dispersive bulk modulus under room-dry condition, Figure 4.14. Due to dispersive bulk modulus. Meanwhile, it confirms that $K/G \approx 1$ in dry sandstone (Smith et al., 2003).

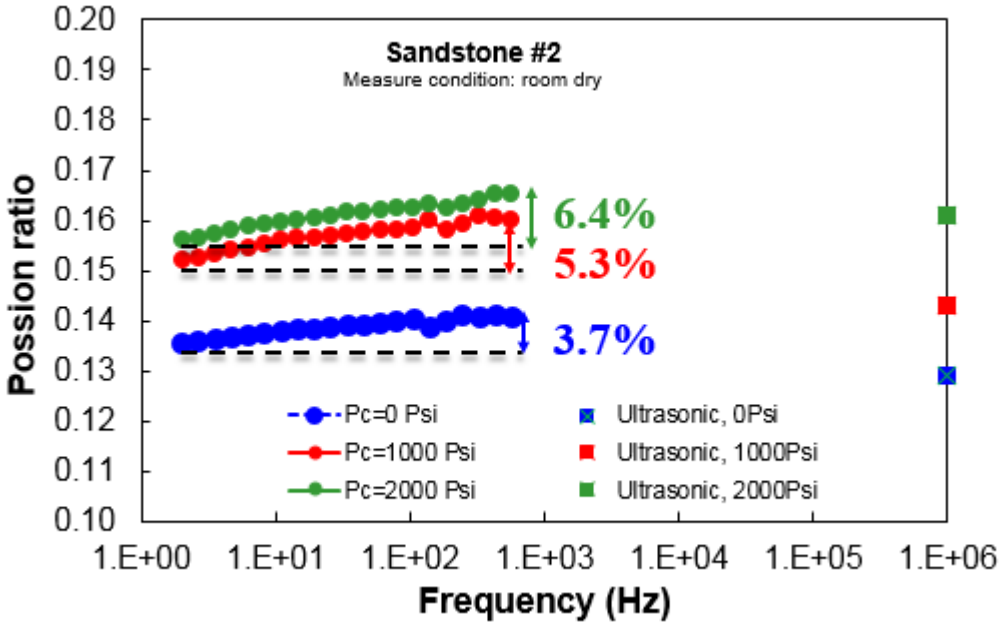

Figure 4.15 Poisson's ratio against frequency for sample #2 under room-dry conditions.

The Poisson's ratio measured in the low-frequency apparatus is actually dynamic. The resonance of the mechanical parts of low-frequency system may affect the dynamic Poisson's ratio, especially at high frequencies around 800 Hz, Figure 4.15. The dynamic Poisson's ratio increases significantly as the differential pressure increases from 0 psi 1,000 psi, then it increases slightly as the differential pressure goes up to 2,000 psi. It

indicates that the pores have a strong effect on Poisson's ratio (Dunn and Ledbetter, 1995; Wang and Nur, 2000). The soft-pores and micro-cracks are closed with increased differential pressure, especially as soft-pores and micro-cracks are sensitive to the initial pressure loading in the high-porosity sample. It can conclude that the presence of considerable numbers of soft-pores and cracks decreases the dynamic Poisson's ratio significantly. In addition, the dynamic Poisson's ratio increases slightly with the increased frequency. Compared with Poisson's ratio at ultrasonic frequency, the Poisson's ratio over low-frequency band is even higher. It is because that Poisson's ratio, converted from measured P- and S-wave velocities, may have significant measurement error.

4.8.4 Low-frequency measurement under partial water-saturation conditions

In order to observe the effect of partial gas/water-saturation on velocity dispersion and attenuation, the imbibition process is performed during low-frequency measurement. The sample is saturated with distilled water at a constant differential pressure of 2,000 psi. Confining pressure is 2,020 psi and pore pressure is 20 psi for all measurement points except water-saturation of 100%, where the confining pressure is 3,000 psi and the pore pressure is 1,000 psi. The constant flow rate ($\upsilon_f = 0.5ml$) is set up to control the saturation state. The valve is closed during the measurement. All measurements are conducted at room temperature.

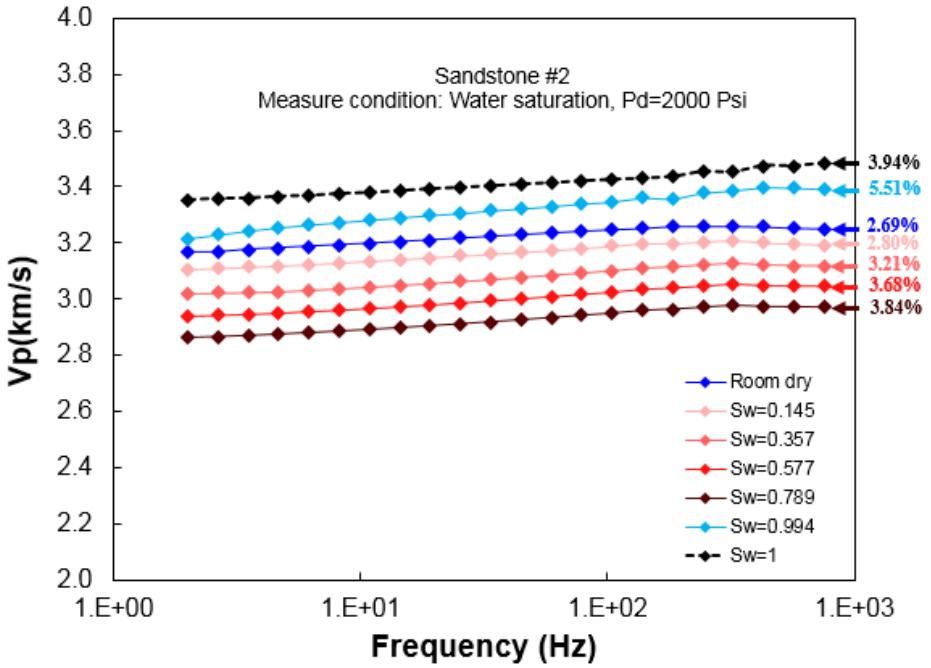

Figure 4.16 Converted P-wave velocity against frequency for sample #2 under different degree of water-saturation.

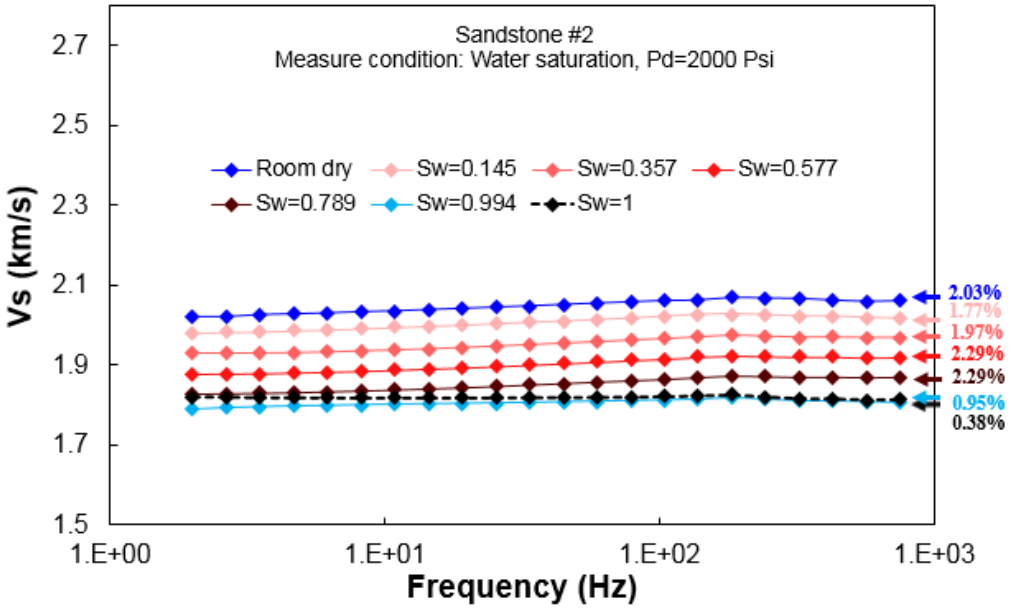

Figure 4.17 Converted S-wave velocity against frequency for sample #2 under different

degree of water-saturation.

The converted P-wave velocity is dependent on both the degree of water-saturation and measured frequency, Figure 4.16. For a given water saturation, P-wave velocity increases gradually with the increased frequency, then it keeps almost constant when frequency reaches about 30 Hz. Moreover, the increment rate of P-wave velocity decreases gradually as the water-saturation increases. According to the data analysis, the peak frequency is around 50 Hz, where the change of P-wave velocity is sharply. In addition, as is evident, for a given measured frequency, P-wave velocity decreases gradually as the degree of water-saturation increases towards 78.9%. P-wave velocity dispersion is highest when the sample is under fully water-saturated condition. In addition, with continuously increased water-saturation, P-wave velocity increases dramatically until water-saturation is almost 100%, Figure 4.16.

As seen in Figure 4.17, S-wave velocity, for a given water-saturation, increases with increased frequency, then it remains almost constant when frequency approaches 300 Hz. Moreover, the rate of increment of S-wave velocity decreases gradually with increased water-saturation, nut with a very weak velocity dispersion, which may be caused by chemical effect. For the peak frequency, the same as P-wave velocity, is about 50 Hz. In addition, S-wave velocity decreases with increased water-saturation until it reaches full 100% water-saturation.

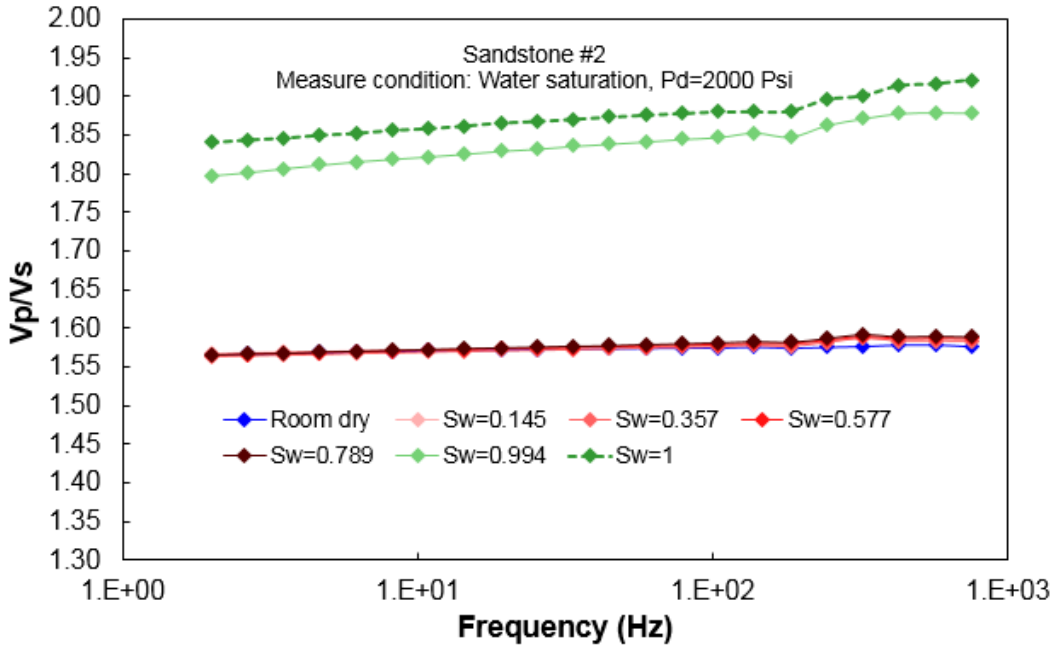

Figure 4.18 The VpVs ratio again frequency for sample #2 at different degree of water-saturation.

Due to the existence of water in the pore space at almost fully saturated status, there is a strong increment in the bulk modulus than shear modulus. As a result, the dynamic VpVs ratio remains constant until water-saturation towards 78.9%, then it increases dramatically under fully water-saturated condition, Figure 4.18, (Carcione and Cavallini, 2002). This may give us an indicator regarding the application of dynamic VpVs ratio of water-saturated porous rock to identify lithology (Domenico, 1983; Kithas, 1976; Miller and Stewart, 1990; Pickett, 1963; Winkler et al., 1979).

Poisson's ratio, as a water-saturation indicator, is extremely sensitive to the degree of water-saturation, Figure 4.19. Evidently, for a given frequency, Poisson's ratio is

almost constant when the water-saturation is less than 78.9%. It increases dramatically from 0.15 to 0.28 under fully water-saturation condition. In addition, for a given water-saturation, Poisson's ratio increases gradually with increased frequency.

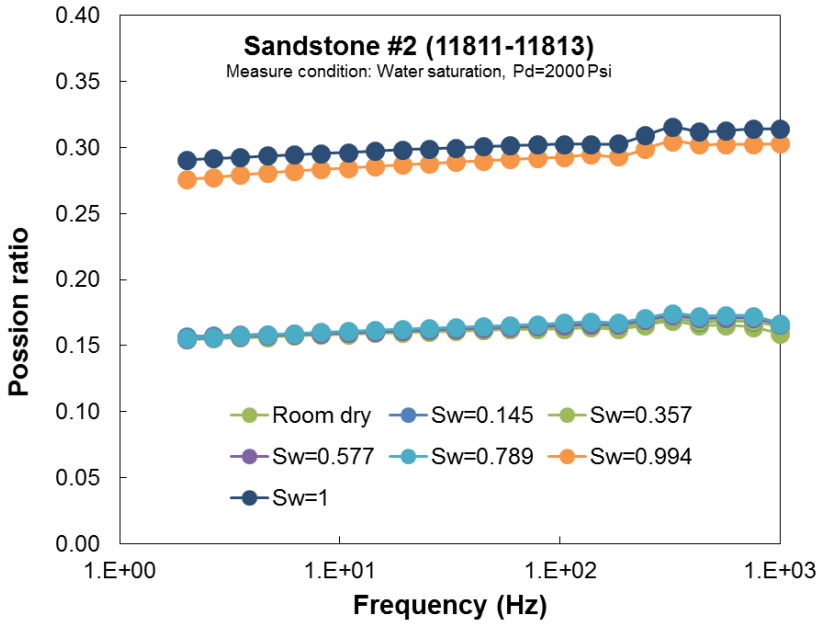

Figure 4.19 The measured Poisson's ratio against frequency for sample #2 under partial water-saturation conditions.

4.9 Discussions

Figure 4.20 shows that the attenuation, characterized by the inverse-quality factor, depends predominantly on degree of water-saturation (Murphy, 1982; Cadoret et al., 1993). As the percentage of water-saturation increases, the attenuation increases until it reaches the energy-loss peaks at a water-saturation of roughly 80%. After that critical water-saturation, the attenuation dramatically decreases. Additionally, it is evident that the attenuation is frequency-dependent. For a given measured frequency, the higher the

frequency, the higher the attenuation. However, the attenuation increment decreases at high frequency.

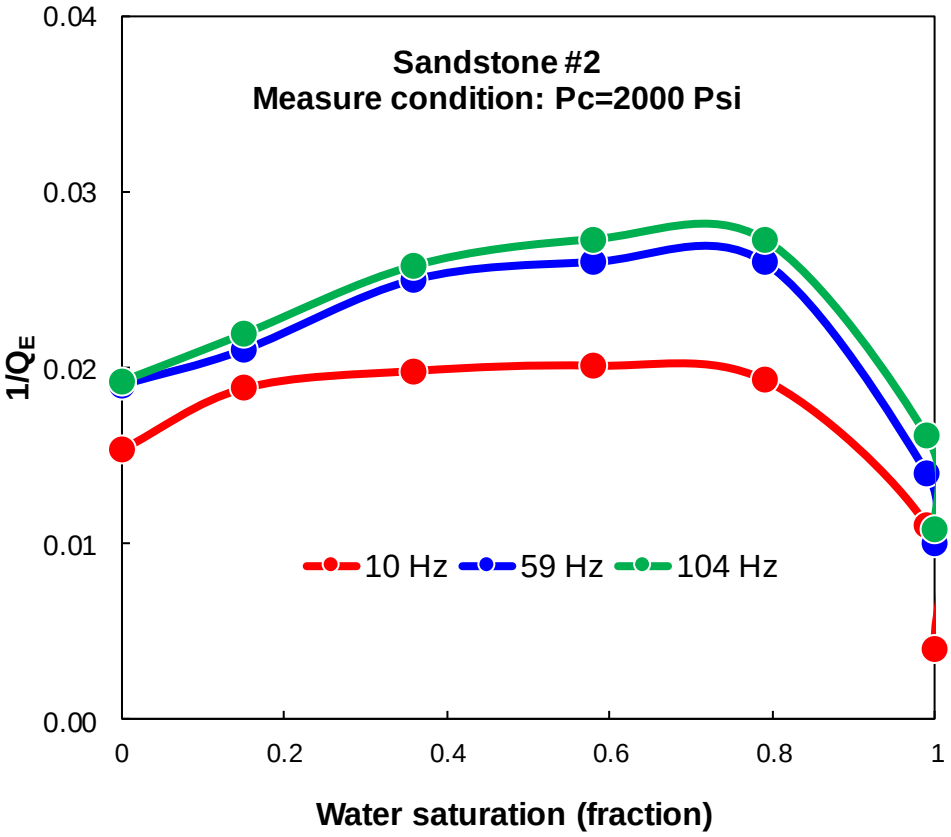

Figure 4.20 The measured Young's inverse-quality factor against water-saturation degree.

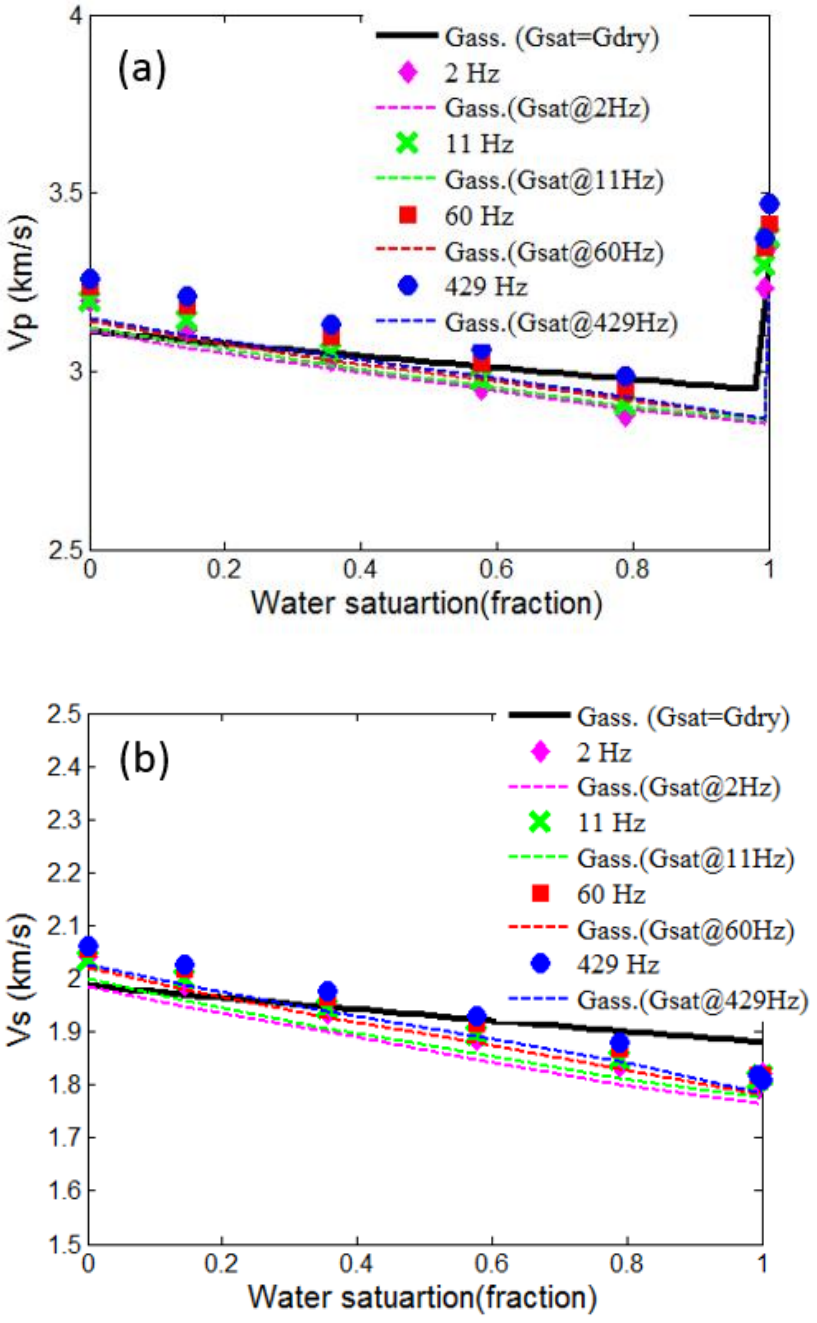

Figure 4.21 Velocities against water-saturation for both measured data and Gassmann predictions. (a) P-wave velocity; (b) S-wave velocity.

Figure 4.21 represents the measured low-frequency data points (dots), which fit well with the Gassmann prediction (dashed line). The input parameters for utilizing the Gassmann's equation are listed in Table 4.2. Estimation errors in the mineral bulk modulus and dry bulk modulus can explain the difference between the measured low-frequency data and Gassmann prediction. For the S-wave in Figure 4.21 (b), the measured data points at low frequencies fit fairly well with constant shear-modulus assumption of Gassmann's equation. The heterogeneous fluid distribution can explain the slight discrepancy (Cadoret et al., 1995). The change in S-wave velocity may result from the density increment with increased water-saturation.

Table 4.2: The input and output parameters for utilizing the Gassmann's equation.

Inputs/Outputs	**Gsat=Gdry**	**Measured Gsat**
Porosity	24.79%	23.49%
Dry bulk modulus *GPa* (Room-dry@2000Psi,2Hz)	8.97	8.97
Shear modulus *Gpa*	8.001 (Room dry@2000Psi,2Hz)	Measured Gsat
Grain bulk modulus *GPa*	38	38
Predicted P-wave velocity (0% Sw/ 100% Sw)	3.1119/3.2891	3.1119/3.2257@2Hz
Measured P-wave velocity (0% Sw/ 100% Sw)	3.1971/3.3513	
Predicted S-wave velocity (0% Sw/ 100% Sw)	1.9865/1.8808	1.9865/1.7964@2Hz
Measured S-wave velocity (0% Sw/ 100% Sw)	2.0409/1.8204	

Note: Gsat is the abbreviation of shear modulus under water-saturation condition. Sw is the abbreviation of water saturation degree.

The Cole-Cole equation, as a single relaxation mechanism model, is applied to fit the measured Young's modulus and attenuation, Figure 4. 22. Table 4.3 shows the fitting parameters. The input Young's modulus at zero frequency is about 2% lower than the measured data at 2 Hz, while Young's modulus at infinite frequency is about 2% higher than the measured data at 240 Hz. The relaxation peak time is calculated from the measured frequency of 50 Hz. Therefore, the distribution factor is the only free parameter. The modeled relaxation peak frequency is around 50 Hz. Meanwhile, the peak-frequency shifts slightly to the low-frequency range as the degree of water-saturation increases. For the suitability of Young's modulus, it is evident that the Cole-Cole model fits well until measured frequency is over 300 Hz, which may result from the overlapping of multiple attenuation mechanisms.

In addition, under supervision, the predicted attenuation fits well with the measured data as is evident in Figure 4.22 (b) in the low-frequency band under all degree of water-saturation except full water-saturation. It is because the attenuation is very weak at fully saturated state. The low-frequency apparatus limit may cause measurement uncertainty. Due to its intrinsic feature of single relaxation mechanism, the Cole-Cole model cannot predict possible overlapping of multiple relaxation mechanisms for the measured data at high frequencies.

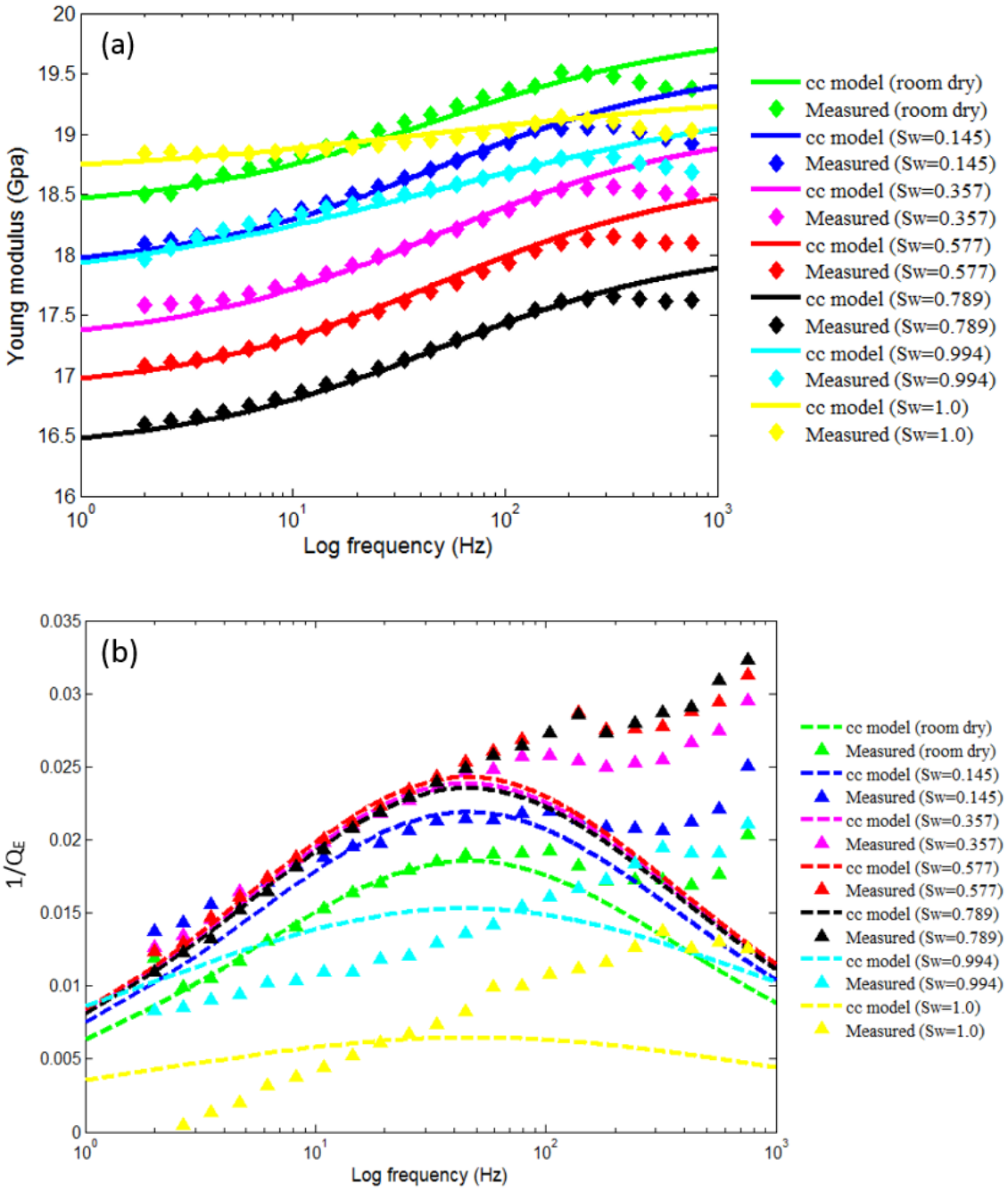

Figure 4.22 (a) Measured Young's modulus and Cole-Cole model fitting against frequency; (b) Inverse-quality factor and Cole-Cole model fitting against frequency.

Table 4.3: The parameters for the Cole-Cole equation for sample #2.

Input parameters	Value
Relaxation peak τ(sec)	0.02
Distribution parameter k	0.46
Young's modulus at zero frequency $M_0(Gpa)$	2% lower than data point at 2 Hz
Young's modulus at infinite frequency $M_\infty(Gpa)$	2% higher than data point at 240 Hz

4.10 Conclusions

The measured results show that the velocity dispersion and attenuation at seismic frequencies cannot be neglected and are significant in seismic characterization. Comparisons between velocities achieved in the low-frequency range (2-800 Hz) and those achieved in the ultrasonic frequency band (10^6 Hz) can show large differences, even for the room-dry rocks. Theoretical models, particularly those assuming zero or low frequencies, may fail to predict the behavior of rock.

The measured data shows that the fluid inside the pore space of rocks has a significant impact on the elastic properties of the sandstones. Two factors are must be considered. One is the degree of water-saturation, another is the measured frequency. The fluid-saturated porous sandstone may demonstrate different relaxation mechanisms. If the macroscopic pore fluids presenting at low frequency has time to equilibrate, the Gassmann's equation can model the response between the pore fluids and rock frame. However, a substantial modulus increment is observable with the increment in the measured frequencies, where disequilibrium pore-pressure occurs when pore fluids do

not have enough time to equilibrate. Moreover, the different attenuation mechanisms may overlap. As the relaxation times (frequencies) of different flow mechanisms are crossed, attenuation reaches a peak and the elastic modulus (velocity) increases sharply.

Chapter 5
Porosity of heavy oil-sand: laboratory measurement and bound analysis

5.1 Abstract

The conventional porosity measurement is not adequate to precisely measure "as-is" porosity of heavy oil-sand sample due to its irregular sample shape, viscous pore-filling fluids, and especially difficult storage without losing mass. A confined porosity measurement strategy is specifically proposed to measure the "as-is" porosity of heavy oil-sand sample. This overall strategy primarily consists of two parts. First of all, "as-is" porosity is estimated using both assumed parameters (grain density, fluids density and fluids saturation) and directly measured bulk-density that is calculated from Archimedes principle. As a consequence, it not only keeps the sample intact, but also is advantageous on minimizing mass loss and external covers. Furthermore, by extracting the pore fluids (heavy oil, water, and possible gas) from the original sample, the assumed parameters are precisely measured. Therefore, another porosity-data can be calculated applying directly measured grain volume data and bulk volume data. Based on the measured data and error analysis, It can conclude that the porosity calculated from directly measured dataset gives us a low bound of porosity, while "as-is" porosity estimated from Archimedes principle presents a upper bound of porosity.

5.2 Introduction

Heavy oil-sand is significant unconventional reserves. It holds the promise of becoming useful fuels when the global demand for energy is increasing steadily. Heavy oil is defined as having API between 22.3^{o} and 10^{o}, whereas API of bitumen is even less than 10^{o}. Heavy oil is often considered to play a unique role in influencing the elastic properties of heavy oil-sand reservoir. First, heavy oil can act like a quasi-solid when temperature is less than the temperature of solid point, wherein it has a shear modulus. Second, heavy oil is strongly temperature-dependent, which causes the physical properties of heavy oil-sand to be temperature-dependent as well. Third, heavy oil often acts as cementing agent in unconsolidated sand (Batzle et al., 2004, 2006; Han et al., 2008). Therefore, the viscosity of heavy oil is a crucial factor to impact reservoir productivity. Moreover, temperature has indispensable impact not only on the physical properties, but also the shape of heavy oil-sand in the laboratory.

Porosity measurement on sample of heavy oil-sand with "original" fluid-saturation, which is called as "as-is" measurements, is still challenging due to unique properties of heavy oil. The viscous heavy-oil with other fluids generally fill with pore space. As a result, heavy oil-sand is completely different from unconsolidated sand packs-saturated with temperature-independent fluid. Heavy oil often leads to shape change when the sample of heavy oil-sand is under the effect of external influences, such as thermal effect, pressure variation, and core damage. With respect to unconsolidated sand with good sorting, grain-packing mechanism indicates that the porosity can be reduced to 30% from the initial high-porosity with low-pressure. However, fluids-supported sample of heavy

oil-sand is usually deposited at shallow stratum. Therefore, sand-suspended in heavy oil will cause high-porosity under room condition. The high-viscosity of heavy oil also makes the sample of heavy oil-sand bear ultra-low apparent-permeability and isolated air bubbles. Usually, "as-is" porosity is around 36%, and in some case, it can be higher than 40%, which is beyond the typically critical porosity of random granular packs. Although the sample of heavy oil-sand has high-porosity, most pores is fully saturated with viscous heavy oil. Therefore, the porosity does not vary very much with the variation of the confining pressure under the assumption of no fluids leaking. In addition, due to pore-filling with viscous heavy oil, the conventional Boyle porosimeter fails to measure the porosity of heavy oil-sand sample.

Two important issues are at least required to be addressed during the measurement of "as-is" porosity of sample of heavy oil-sand. First, it is necessary to keep the sample of heavy oil-sand intact during the measurement, because the sample may need to go through different laboratory processes. Second, precisely estimating physical parameters, including bulk volume, grain density, and fluids saturation in the porosity measurement, is another key issue that should pay particular attention to either in the laboratory or in the reservoir production. However, this subject has been sparsely documented in published literatures. In this chapter, a new confined laboratory-measurement strategy is proposed to measure porosity of sample of heavy oil-sand.

This chapter is organized as follows: First, the samples of heavy oil-sand are briefly introduced. Meanwhile, the measurement workflow is also described to show proposed measurement strategy. Then the Archimedes principle is introduced to show

specifically how the “as-is” porosity to be calculated. Next, the laboratory processes of extracting the pore fluids from the sample of heavy oil-sand are carried out. Meanwhile, the porosity is calculated using directly measured grain volume and bulk volume. Finally, two-group data of measured porosity are analyzed to constrain the possible confined bounds on porosity of sample of heavy oil-sand.

5.3 Sample description and measurement strategy

All core plugs come from a shallow heavy oil-sand reservoir. They are frozen with cylinder shape: 1.5 inch in diameter, roughly 3 inch in length, and jacketed with the wrapped Teflon-tape inside, metal foil, and metal screen caps, Figure 5.1. Most samples appear as poorly unconsolidated sand with heavy oil-saturation. Black, sticky heavy oil seems to serve as viscous glue to hold sand grains together and maintain integrity of solid matrix. As a result, the sample of heavy oil-sand could be easily deformed and damaged due to its unconsolidated nature, Figure 5.1.

Figure 5.1 The shape of sample of heavy oil-sand.

In general, the sample of heavy oil-sand is plugged out from a whole core with liquid nitrogen as cooling liquid to maintain sample integrity. Our samples are stored in a freezer all the time to preserve integrity. We cannot directly measure porosity of sample of heavy oil-sand due to existing pore fluids, which may include heavy oil, water, and gas bubbles. However, because gas can bubble out from pore liquids due to the pressure release when core is retrieved to surface, so gas may not exist in pores anymore under surface condition. Air packets in pores can also be generated as water vaporizes naturally, especially for the defrosted sample. If the pore fluids is cleaned out, sand framework is most likely to collapse into loose sand. Therefore, with respect to carefully handle the sample because it is easily altered and the original form cannot be recovered. Due to the nature of the sample of heavy oil-sand, the laboratory measurements are destructive, process-dependent. As a consequence, recording all the measurement processes and intermediate results are obligatory to keep dataset consistent and meaningful.

We assume those samples are maintained under in-situ conditions:

1. Whole core-drilled, and retrieved without damage under in-situ condition.
2. Samples-drilled, transported, and stored without damage.
3. Part of pore fluids may be lost when sample is retrieved. In most likely case, gas may be released if it exists in pore fluids. Water (ice) can be evaporated under frozen condition. As a result, heavy oil will remain in pores with a fraction of water and trivial air.

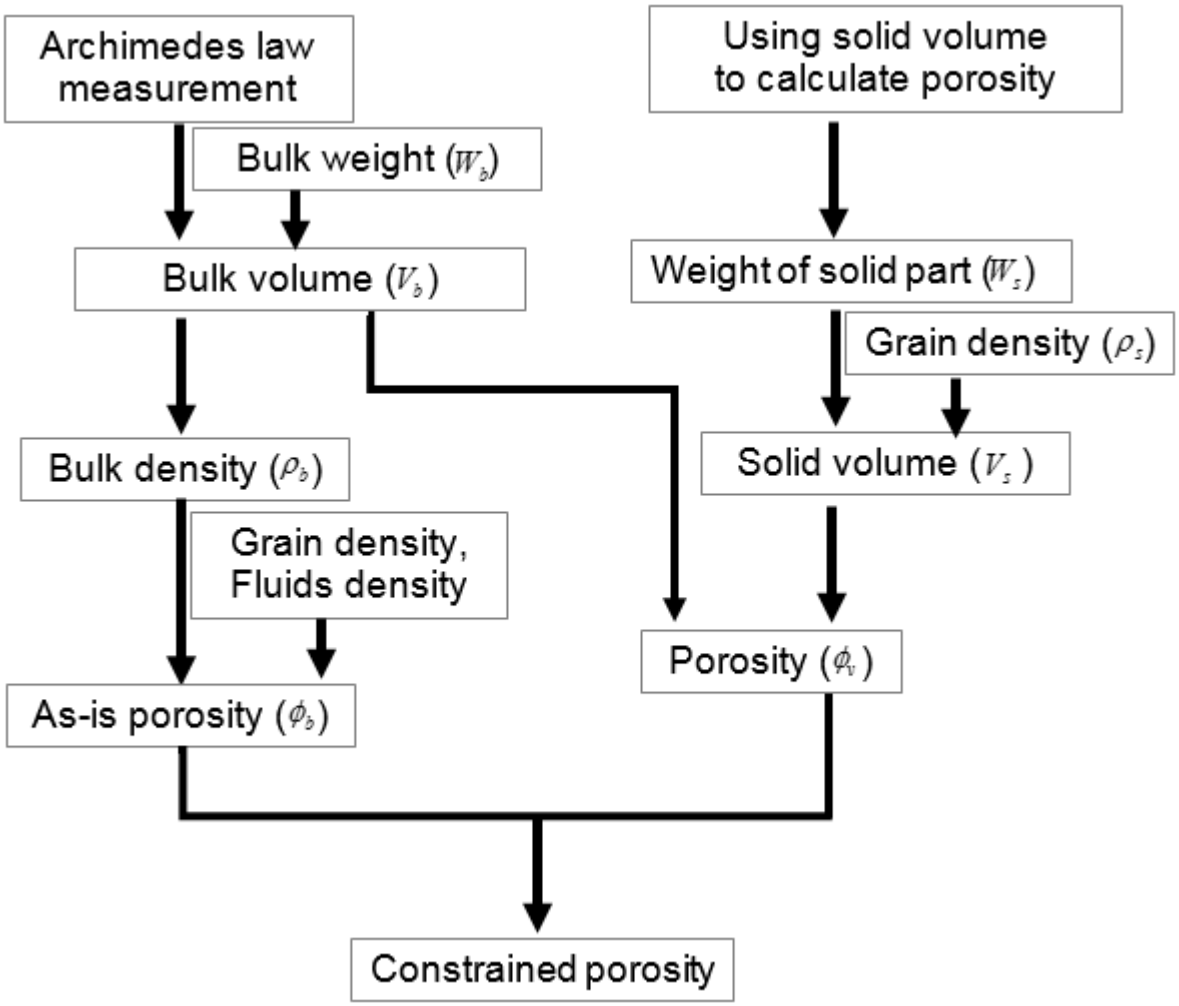

Figure 5.2 Porosity-measurement strategy of sample of heavy oil-sand using Archimedes principle (left) and using solid-volume preservation (right).

Additional pore space may also be generated due to sample expansion, or possible damage. In order to minimize unnecessary damage and accurately estimate porosity during the measurement, the following porosity-measurement strategy is proposed as seen in Figure 5.2. The primary goal of keep sample intact is a key point using

Archimedes law during the porosity measurements. Extracting the fluids (heavy oil/water/gas) to isolate the solids part is a supplementary step to precisely measure required parameters, including fluids density, grain density, and solid volume. Moreover, it leads us to an alternative option of laboratory measurement to calculate the porosity of heavy oil-sand.

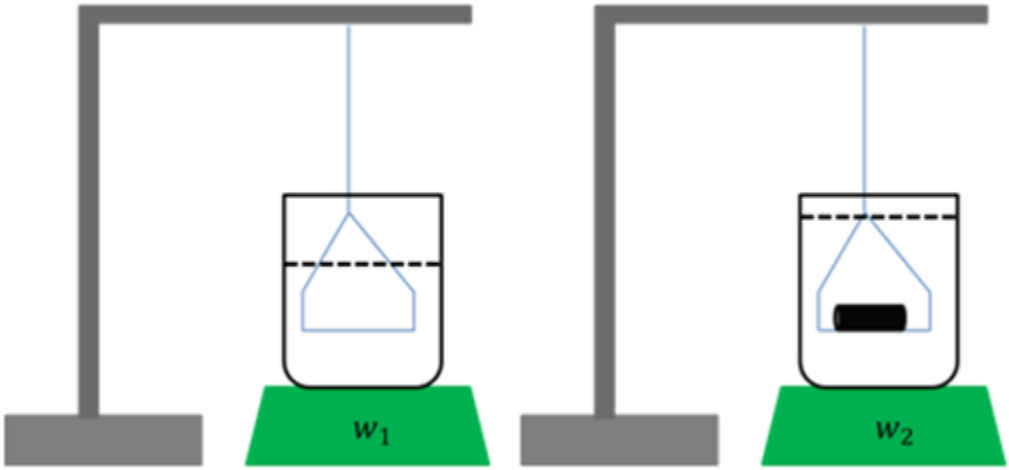

Figure 5.3 A schematic of porosity measurement method applying Archimedes principle.

5.4 Procedure of porosity measurement using Archimedes principle

Considering irregular shape of deformable heavy oil-sand sample, the Archimedes principle is first applied to measure the bulk volume. It not only keeps the sample intact but also measures the accurate bulk volume to calculate the "as-is" porosity as a high-bound of porosity under the assumption of 100% fluid-saturation. As a supplementary but necessary step, extracting the pore fluids from the sample of heavy oil-sand can not only successfully predict a low bound of porosity of heavy oil-sand

based on the direct measurement data, but also provide a chance to further constrain the precise percentage of fluid kind.

The equation for the "as-is" bulk-density of sample of heavy oil-sand can be written as

$$\phi \cdot (S_o + S_w)\rho_{fluid} + \phi \cdot S_{air}\rho_{air} + (1-\phi)\rho_{grain} = \rho_{basis} \quad (5.1)$$

where, S_0 is oil saturation, S_w is water saturation, and S_{air} is air saturation; ρ_{fluid} is fluids density, ρ_{air} is air density, ρ_{grain} is grain density, ρ_{basis} is "as-is" bulk density; ϕ is "as-is" porosity.

if assuming air density ρ_{air} is 0, the "as-is" porosity can be expressed as

$$\phi = \frac{\rho_{grain} - \rho_{basis}}{\rho_{grain} - (S_o + S_w)\rho_{fluid}} \quad (5.2)$$

ρ_{basis} is the parameter that is measured in the Archimedes principle, the rest can also be measured in the subsequent step of fluids extraction.

According to the Archimedes principle,

$$V_t = \frac{w_2 - w_1}{\rho_w} \quad (5.3)$$

where ρ_w is the density of water; "$w_2 - w_1$" is the mass difference before and after submerging heavy oil-sand sample with covers into water; V_t is the water volume occupied by the sample. If there is no water invading into the sample, V_t should be equal to the bulk volume of the sample with the Teflon cover.

Generally, the sample of heavy oil-sand is wrapped with the Teflon tape and metal foil on the surface, and two-screen caps on the top and bottom of core plug, respectively. In order to make accurate measurement, we need to remove all the metal foils off and maintain the minimum of Teflon cover and one screen in each side to keep the integrity of sample. Therefore, effect of attached Teflon wraps and screen on the porosity measurement is required to be revised as seen in Figure 5.4.

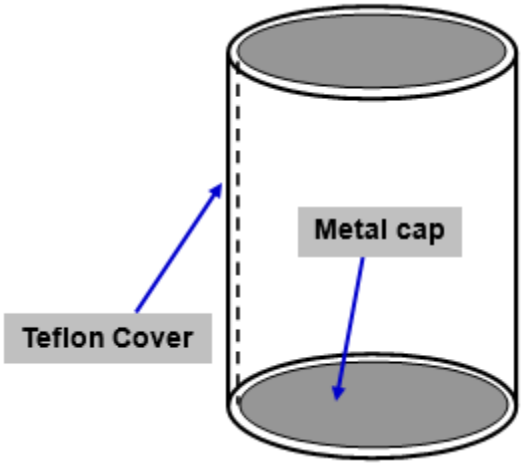

Figure 5.4 A schematic of the Teflon wrapping around sample and metal caps in two-side of sample of heavy oil-sand.

Based on this idea, porosity laboratory-measurement steps is given by:

Step 1: Estimate the native bulk mass w_b of sample of heavy oil-sand

$$w_b = w_{total} - w_{teflon} \tag{5.4}$$

where w_{total} is the mass of measured sample; w_{teflon} and w_{caps} are the mass of Teflon and caps, respectively.

For the sample of heavy oil-sand with regular cylinder shape, which is first wrapped with Teflon tape, then with nickel foil and 2-3 layers of stainless steel-mash screens to protect the sample. In general, it may highly damage the sample of heavy oil-sand due to the viscous heavy oil and fragile rock frame when taking wrapped material off. In order to minimize the sample damage when estimating the mass of wrapped materials, the wrapped foil and tape are removed from a shale sample, measure their mass, and define the relationship with the sample length. Based on the sample length of heavy oil-sand, the mass of wrapped material and screen can be estimated, therefore, their volumes can be calculated with known density. Specifically, since the area density of Teflon is 0.0192 g/cm^2, we can estimate the Teflon mass that equals to cover area of Teflon by area density. Two-screen caps are 0.55 g. According to Equation 5.4, it is easy to estimate the native mass of the sample of heavy oil-sand. Error on such mass estimation is usually less than 0.3 g, which is less than 0.5% of sample mass.

Step 2: Calculate the native bulk volume V_b of sample of heavy oil-sand

$$V_b = V_{total} - V_{teflon} - V_{caps} \tag{5.5}$$

Where V_{total} is the volume of measured sample; V_{teflon} and V_{caps} are volumes of covered Teflon and caps, respectively. From step 1 to step 2, we use density of Teflon (2.2 g/cm^3) to calculate V_{teflon}, the same as for V_{caps} with density of 7.8 g/cm^3.

If no water invades into measured sample, its mass does not change before and after submerging into water tank, and sample volume V_{total} will be equal to the volume V_t calculated based on Equation 5.3. If there is water invasion, that shows as the increment of sample mass *dw* after the sample is submerged into water tank, then we need to compensate *dw* effect on the w_2 due to reduction of buoyancy force using Equation 5.6. For most heavy oil-sand samples, *dw* is relatively small, even negligible. Large *dw* may indicate a large portion of air in pore space.

$$V_{total} = V_t + dw/\rho_w = \frac{w_2 - w_1 + dw}{\rho_w} \tag{5.6}$$

Step 3: Calculate the "as-is" bulk density

"As-is" bulk density ρ_{basis} of measured sample is calculated as ratio of the sample mass w_b to the volume V_b.

$$\rho_{basis} = \frac{w_b}{V_b} \tag{5.7}$$

The calculated "as-is" bulk density from the sample mass and sample volume is applied to characterize the initial status of sample of heavy oil-sand.

Step 4: Calculate the "as-is" porosity

Now we can calculate porosity based on the following assumptions:

1. Assume that grain density ρ_{grain} is equal to 2.65 g/cm^3.

2. Assume that heavy oil and water have the same density as 0.998 g/cm^3.

3. Assume that the sample heavy oil-sand is fully saturated with heavy oil and water, and air occupied pore space is ignored.

$$S_0 + S_w + S_{air} = 1 \approx S_0 + S_w \qquad (5.8)$$

where, S_0 is oil saturation, S_w is water saturation, and S_{air} is air saturation.

Actually, these assumptions can be verified and updated with measured data when performing the fluids extraction later. It is found that the assumption 1 and 2 are reasonable and cause negligible errors. However, ignoring contribution of air occupied pore space willoverestimate porosity. Fortunately, the air saturation S_{air} can also be measured during the process of heavy oil-extraction. If assuming air density ρ_{air} is 0, the "as-is" bulk density of sample of heavy oil-sand can be written

$$\phi = \frac{\rho_{grain} - \rho_{basis}}{\rho_{grain} - (S_o + S_w)\rho_{fluid}} \leq \phi_b = \frac{\rho_{grain} - \rho_{basis}}{\rho_{grain} - \rho_{fluid}} \qquad (5.9)$$

Since we ignore the pore space occupied by the air, the actually estimated porosity ϕ_b is overestimated comparing with ideally calculated ϕ, as shown in Equation 5.9. All the measurements are carried out at room temperature and pressure conditions.

Based on the measured "as-is" bulk density of the sample of heavy oil-sand and reasonable assumptions, the "as-is" porosity can be calculated, as seen in Table 5.1. Because the assumption of heavy oil-water saturation will overestimate "true" porosity, the porosity ϕ_b data in the table 5.1 is seen as a high bound of porosity of heavy oil-sand

sample. If we assume the sample is partially saturated by 80% or 90% heavy oil (suffix "Sb" in the Figure 5.5), and the rest pores are saturated with air. Data suggests that 10% of air-saturation can cause 6% porosity reduction. Therefore, in order to accurately estimate porosity, measuring the precise air-saturation of frozen sample is an indispensable step. In the porosity calculation, the density of water is 0.998 g/cm^3 and the density of heavy oil is 1.025 g/cm^3, which are measured by Rock Physics Laboratory at University of Houston.

Table 5.1: Measured porosity ϕ_b of sample of "as-is" heavy oil-sand with the assumption of 100% fluids-saturation.

Sample	Porosity
1	0.4155
2	0.4667
3	0.4486
4	0.4279
5	0.3681
6	0.4028
7	0.4705
8	0.4606
9	0.4597
10	0.4610

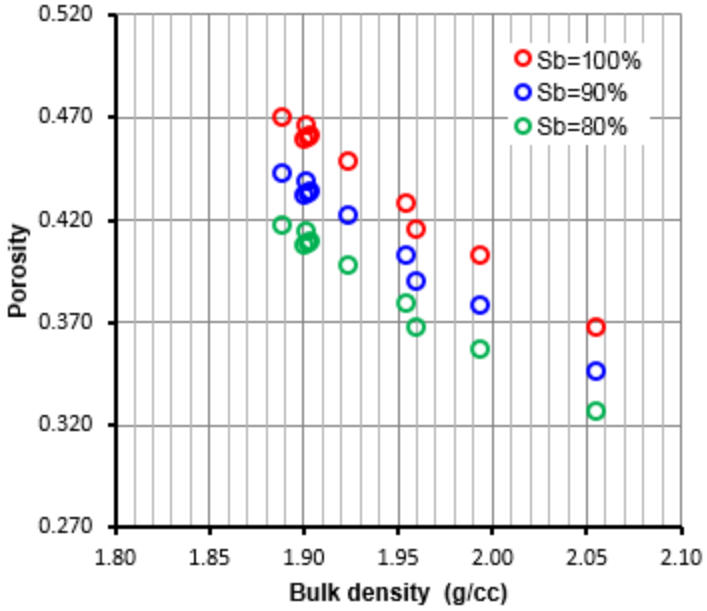

Figure 5.5 Estimated porosity with different degree of heavy oil-saturation. The abbreviation "Sb" indicates the percentage of heavy oil-saturation.

5.5 Porosity calculation using solid volume

5.5.1 Procedure of Heavy oil-extraction

The field samples are not allowed us to break down for they are expensive and rare. Therefore, applying the Archimedes principle can ensure experimental measurements without sample damage. Since the bulk volume has been successfully estimated using Archimedes principle. According to theoretical analysis, directly measured data will provide us a low bound of porosity of heavy oil-sand sample. Practically, we apply heavy oil-extraction method to extract the heavy oil and weigh the residual grain volume. In order to do so, we need to briefly introduce the procedure of heavy oil-extraction, Figure

5.6 (Allen, 1973; Brown et al., 1977; Das, 1995). With mixing solvent, chemical process of extracting heavy oil will take 4-6 weeks under low-temperature condition.

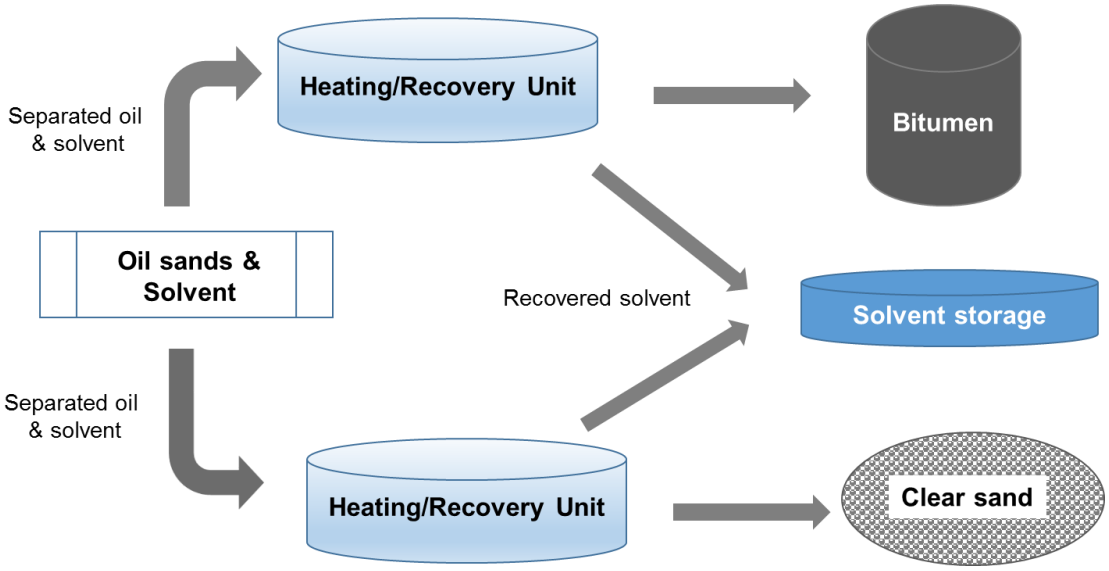

Figure 5.6 A schematic of the procedure of heavy oil-extraction.

Sand grains is carefully weighed when all pore fluids (heavy oil and pore water) are cleaned out. Heavy oil is carefully extracted, its mass is completely preserved during the entire extraction procedure. Unfortunately, we cannot measure the mass of pore water directly, because pore water evaporates during the extraction processes. However, the mass of residual pore water is calculated, based on the weight differences before and after the extraction, if assuming it is no air-occupied in pore space. The mass of "as-is" sample w_b is equal to

$$w_b = w_g + w_o + w_w \tag{5.10}$$

where w_g is the mass of sand grains, and w_o is the mass of heavy oil. The mass of air w_a is ignored. The mass of pore water w_w can be calculated.

$$w_w = w_b - w_g - v \tag{5.11}$$

If we assume that the sample of heavy oil sand is fully saturated with heavy oil and water without any air trapped in the pore space, the mass of pore water w_w calculated from Equation 5.11 can help to calculate porosity, water saturation, and oil saturation.

5.5.2 Mineral density measurement

After the heavy oil-extraction, because the inner wrapping-Teflon cover fails to hold sample integrity, dry sand framework collapses into loose sand. There is no framework structure existing after extraction processes. Therefore, mineral density of solid grains can be measured with helium porosimeter. Figure 5.7 shows measured mineral density, which clearly suggests that our assumption of grain density of 2.65 g/cm^3 is reasonable.

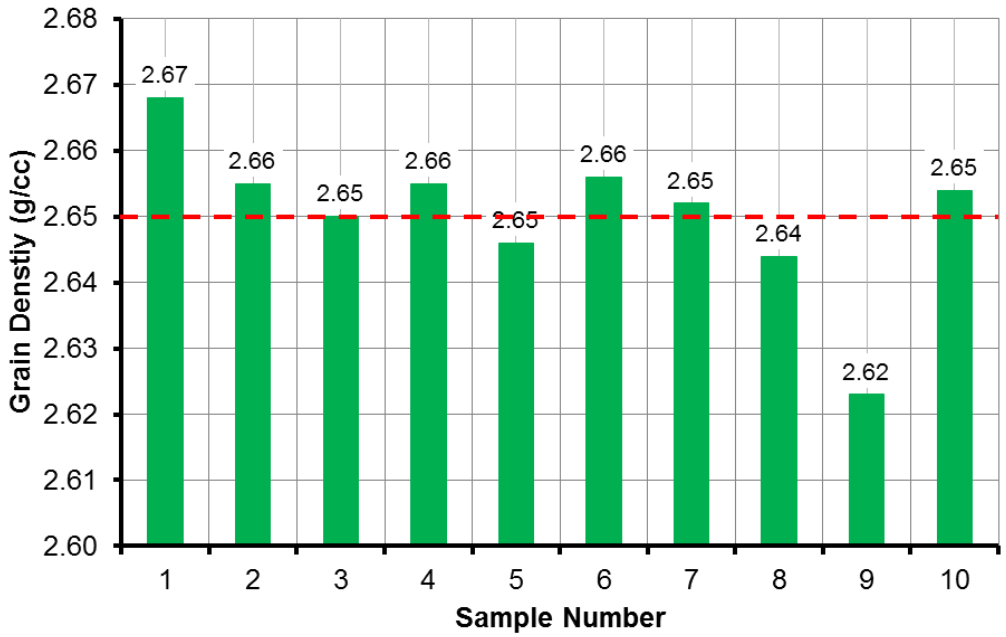

Figure 5.7 Grain density of the sample of heavy oil sand.

5.5.3 Porosity calculation using directly measured solid volume

Theoretically, if we have weighted the mass and its corresponding density for all components of the sample of heavy oil-sand, it gives us a chance to calculate the volume relations

$$V_b = V_g + V_o + V_w + \qquad (5.12)$$

here, $V_g = \frac{w_g}{\rho_g}; \quad V_o = \frac{w_o}{\rho_o}; \quad V_w = \frac{w_w}{\rho_w}; V_a = \frac{w_a}{\rho_a}.$

where V_b is bulk volume of sample, V_g is grain volume, V_o is oil volume, V_w is water volume, and V_a is air volume. ρ_g, ρ_o, ρ_w, ρ_a is solid density of the sample of heavy oil-sand, oil density, water density and air density, respectively.

In Equation 5.12, because we do not know air volume V_a, it is impossible to calculate the bulk volume V_b with the mass preservation data. Here, the sum V_{wa} of the water volume V_w and the air volume V_a is a constant value if assuming oil volume V_o remains constant. The w_w is the mass of residual water, which can change easily. As we have mentioned that pore water can be evaporated if the sample is exposed under room condition for a few days. Therefore, we cannot help to estimate porosity and fluid saturation based on the theoretical Equation 5.12. However, if we use the bulk volume measured using the Archimedes principle, pore volume is estimated as

$$V_p = V_o + V_w + V_a = V_b - \tag{5.13}$$

where, V_p is pore volume.

Then porosity ϕ is defined as the ratio of pore volume and bulk volume, which can be calculated as,

$$\phi = \phi_v = \frac{V_p}{V_b} = \frac{V_b - V_g}{V_b} = 1 - \frac{V_g}{V_b} \tag{5.14}$$

Equation 5.14 is an alternative option to calculate porosity ϕ_v, based on the measured solid volume. This porosity calculation method applies directly measured data without additional assumptions. Hence, it is a reliable laboratory measurement choice to

predict porosity of heavy oil-sand sample with acceptable uncertainties. Measured solid volume data and calculated porosity of heavy oil-sand samples are listed in the table 5.2. The data are systematically lower than the estimated porosity ϕ_b as Equation 5.9 shows.

Table 5.2: Porosity calculation using measured solid volume

Sample	Grain weight (g)	Grain density (g/cc)	Grain volume (cc)	Bulk volume (cc)	Porosity
1	174.00	2.62	66.412	108.8108	0.390
2	124.00	2.67	46.442	83.2068	0.442
3	141.15	2.66	53.064	89.3706	0.406
4	171.00	2.65	64.528	104.1920	0.381
5	168.00	2.66	63.158	93.2700	0.323
6	142.24	2.65	53.675	92.7298	0.421
7	144.35	2.66	54.267	95.4357	0.431
8	133.00	2.65	50.189	85.0751	0.410
9	144.00	2.64	54.545	92.8117	0.412
10	110.45	2.65	41.679	70.3510	0.408

5.6 Uncertainties analysis

Laboratory measurement on porosity of the sample of heavy oil-sand is always challenging. The data uncertainties are unavoidable, especially considering the unconventional strategy of porosity-measurement. Hence, it is necessary to make an uncertainty analysis to evaluate the reliability of measured data. The following measurement steps possibly cause uncertainties during the porosity measurement.

5.6.1 Archimedes principle of porosity measurement

a. Wrapped Teflon layers: According to our estimation of wrapped Teflon in the sample of heavy oil-sand, it might overestimate or underestimate the weight of Teflon due to the length uncertainties.
b. Residual heavy oil in the metal foils and caps: Since the heavy oil is very sticky and viscous, some will remain on the metal foils and caps when separated from original heavy oil-sand sample.

5.6.2 The procedure of heavy oil-extraction

c. Residual sand grains left in the Teflon covers: During the heavy oil-extraction, it is found that there is still small amount of sand grains left in the Teflon cover with sticky heavy oil. As a result, we will overestimate the porosity calculated from grain volume.
d. Light component of heavy oil evaporating: We carefully keep the status of low-temperature during the process of oil extraction. However, there is still a chance that the light component of heavy oil could be evaporated, which will probably cause underestimation of heavy oil-saturation.
e. As mentioned, the “as-is” heavy oil-sand sample contains heavy oil, pore water, and empty space filled with air. But the sample is exposed in room condition for few days before putting into the extraction system, it could cause pore-water evaporation.

5.7 Discussions

5.7.1 Comparison of two datasets

Porosity data ϕ_b, measured by using Archimedes principle, and with porosity ϕ_v, calculated by using the solid volume preservation method, as listed in Table 5.3. Clearly, porosity ϕ_b overestimates "true" porosity and is systematically higher than porosity ϕ_v, except sample 6. It is primarily caused by the assumption of ignoring the pore space occupied by the air in the heavy oil-sand sample. The theoretical "as-is" porosity equation can be expressed as:

$$\begin{aligned}\phi &= \frac{\rho_{grain} - \rho_{basis}}{\rho_{grain} - (S_o + S_w)\rho_{fluid} - S_{air}\rho_{air}} \\ &= \frac{\rho_{grain} - \rho_{basis}}{\rho_{grain} - (S_o + S_w)\rho_{fluid} - [1-(S_o + S_w)]\rho_{air}}\end{aligned} \tag{5.15}$$

Since the air-saturation is assumed to be zero in the Archimedes principle, namely, term $[1-(S_o + S_w)]\rho_{air} = 0$, meanwhile, the increment of term $(S_o + S_w)\rho_{fluid}$ will be dramatically greater than decrement of term $[1-(S_o + S_w)]\rho_{air}$ because the $\rho_{fluid} >> \rho_{air}$, the denominator will decrease, therefore, ϕ is finally overestimated.

Table 5.3: Porosity comparison between data from Archimedes principle and from directly measured solid volume data

Sample	Porosity ϕ_b	Porosity ϕ_v	$\phi_b - \phi_v$
1	0.4155	0.390	0.026
2	0.4667	0.442	0.025
3	0.4486	0.406	0.043
4	0.4279	0.381	0.047
5	0.3681	0.323	0.045
6	0.4028	0.421	-0.018
7	0.4705	0.431	0.040
8	0.4606	0.410	0.051
9	0.4597	0.412	0.048
10	0.4610	0.408	0.053

Since the effect of air saturation on the bulk density is ignored, which causes the overestimation of porosity ϕ_b. The difference may indicate the air saturation in pores.

$$\phi_b = \frac{\rho_{grain} - \rho_{basis}}{\rho_{grain} - \rho_{fluid}} \geq \phi_v = 1 - \frac{V_g}{V_b} \tag{5.16}$$

Based on measured samples in this chapter, porosity of sample of heavy oil-sand under room condition typically ranges between 35% and 40%, with heavy oil-saturation of ~70%. Pore water may be lost during the sample preservation. Therefore, additional pore space could be generated by the sample expansion, or possible damage. Hence, it generally tends to be several percent unit (PU) higher than the porosity estimation from well-log.

5.7.2 Porosity bound analysis

Because the measured bulk volume may be sightly overestimated due to the extra pore generation and mass loss in grain-volume measurement, as well as, using directly measured data without any assumptions, the porosity calculation can be assumed as a low bound of porosity. On the other hand, due to the assumptions of full fluid-saturation and ignoring air-space occupation in the Archimedes principle, it allows us to estimate a high bound of porosity of sample of heavy oil-sand. With comprehensive analysis on the entire measurement processes, it is believed that the true "as-is" porosity of the sample of heavy oil-sand is close to the low bound of porosity.

5.7.3 Percentage estimation of oil and water-saturation

Figure 5.8 shows porosity estimated based on Equation 5.9 with 100%, 90%, and 80% heavy oil-saturation and porosity ϕ_v based on Equation 5.14. According to uncertainties analysis, the porosity ϕ_v, is close to the true "as-is" porosity of heavy oil-sand. The heavy oil-sand sample appears to have heavy oil-water saturation around 80% to 90%. Then air saturation is 20 to 10% accordingly. On the other hand, the heavy oil and water-saturation can also be estimated based on the solid-volume preservation

$$S_o = \frac{V_o}{V_b - V_g} \quad ; \quad S_w = 1 - S_o \tag{5.17}$$

Most samples show ~70% heavy oil-saturation and ~30% water-saturation, Figure 5.9.

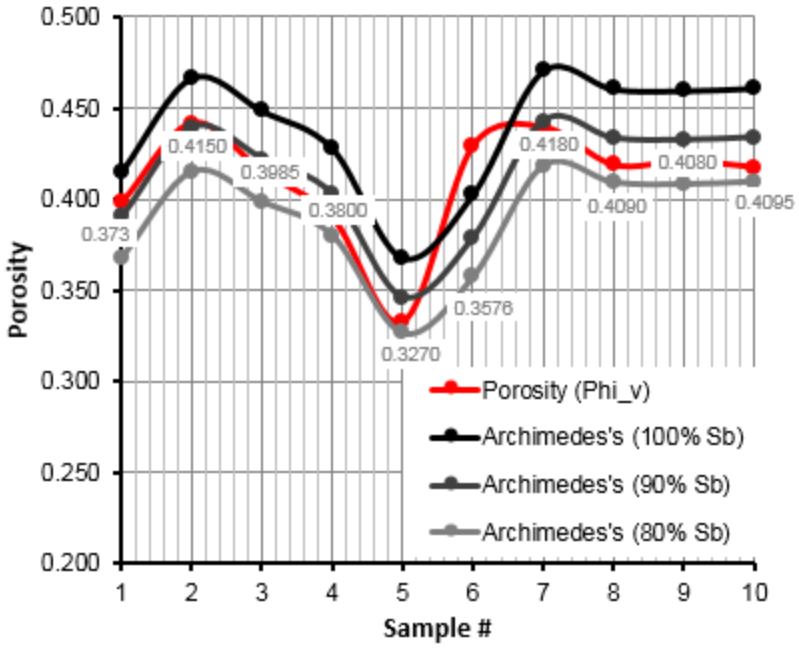

Figure 5.8 Measured porosity with different percentage heavy oil-saturation from two different data sources.

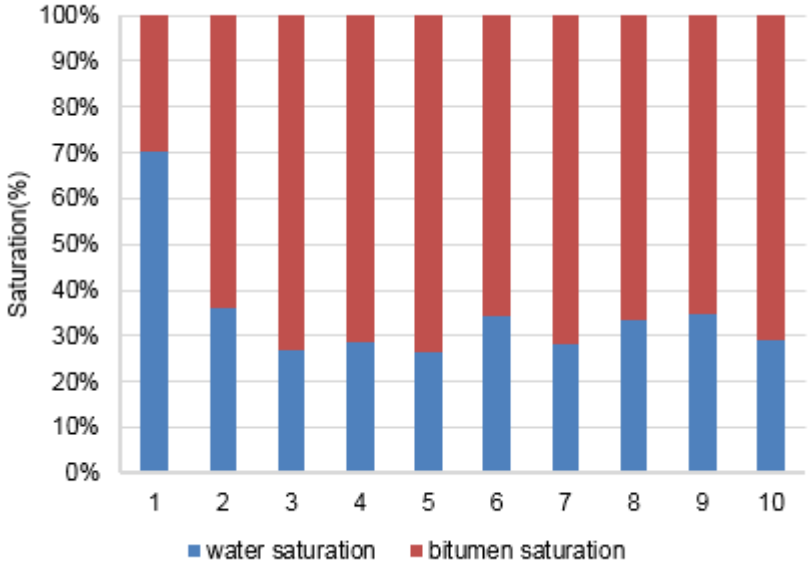

Figure 5.8 Porosity, measured by using Archimedes principle with different degree of heavy oil-saturation from different data sources.

5.7.4 Efficiency and expense

The Archimedes principle is advantageous and adverse on the porosity measurement of the sample of heavy oil-sand. From advantageous look, in fact bulk density is measured with the prerequisites of keeping sample intact, which is the primary goal of application of Archimedes principle. Furthermore, estimating the rest parameters takes an adverse effect on the precise calculation of porosity. As a supplementary step, the fluids density, grain density, and fluid saturation are measured when extracting the fluids from the original sample. However, it breaks the sample and troubles the subsequent measurement. As a trade-off analysis, the representative samples from the same reservoir can be extracted to evaluate the required parameters. From the operable and practical point of view, the Archimedes principle is easy to proceed in the laboratory measurement with key parameters measured from fluids extraction approach. Furthermore, as a compromise of costing and acceptable result, the Archimedes principle with the some key parameters constrained by fluids extraction approach enable us to do the porosity measurement efficiently.

5.8 Conclusions

A hybrid strategy porosity-measurement is proposed to estimate the “as-is” porosity of sample of heavy oil-sand. This two-step method first allows us to estimate the high porosity limit by applying the Archimedes principle. The Archimedes principle method is both advantageous and adverse on the measurement. It is easy and economical in practical experiment for bulk density measurement with the prerequisites of keeping

sample intact, but brings in more uncertainties when ignoring the air in pore and assuming the full fluid-saturation in the porosity calculation. Therefore, a supplementary step is designed. The fluids density, grain density, and fluid saturation are measured when extracting the fluids from the original sample. The obtained a low bound of porosity, according to uncertainties evaluation and error analysis, is close to the true "as-is" porosity of sample of heavy oil-sand. Due to expensive cost and sample damage, we suggest that the representative samples from the same reservoir be extracted to evaluate the required parameters as a trade-off approach when Archimedes principle is applied to measure "as-is" porosity of sample of heavy oil-sand.

Chapter 6
Elastic properties of heavy oil-sand: effects of temperature, pressure, and microstructure

6.1 Abstract

The elastic properties of heavy oil-sand, influenced by multiphase of heavy oil itself and solid matrix with respect to the temperature, pressure, and microstructure, are investigated. In order to separately identify the role of heavy oil and solid matrix under a specific condition, specialized ultrasonic measurements are designed and conducted for both the heavy oil and solid matrix-saturated with heavy oil. Measured data indicate that the viscosity of the heavy oil reaches 10^{15} cP at the temperature of glass point, leading the heavy oil to act as a part of solid frame of heavy oil-sand sample. The heavy oil is likely to be movable pore fluid accordingly, once its viscosity dramatically drops to ~10^{3}cP at the temperature of liquid point. The viscosity-induced elastic modulus of heavy oil, in turn, makes the elastic properties of heavy oil-saturated grain-solid sample be particular temperature-dependent. In addition, the rock-physics model suggests that the microstructure of heavy oil-sand is transitional. Consequently, the solid Gassmann's equation underestimates the measured velocities at the low-temperature range of quasi-solid phase of heavy oil, while overestimates when the temperature exceeds the liquid point. Heavy oil-sand sample shows high modulus and approaches to high bound

due to the stiffer heavy oil acting as solid matrix with decreased temperature. In contrary, heavy oil-sand displays low modulus and approaches to low bound when the heavy oil is becoming softer with increased temperature.

6.2 Introduction

Heavy oil is residues after the bio-degradation of light oil. Heavy oil is defined to bear API between 22.3^{o} and 10^{o}, whereas API of bitumen is even less than 10^{o}. Meanwhile, the high amounts of asphaltenes and resins make the viscosity of heavy oil several orders higher than that of light oil (Curtis, 2002; Das, 2010). Therefore, it exhibit distinct elastic properties. Heavy oil is often considered to have a significant impact on the elastic properties of heavy oil-sand. First, heavy oil acts like a quasi-solid when temperature is less than the temperature of liquid point, wherein it has a shear modulus; Second, heavy oil is strongly temperature-dependent, which, in turn, causes the physical properties of heavy oil-sand to be temperature-dependent; Third, heavy oil often acts as a cementing agent for unconsolidated sands in sedimentary rock (Batzle *et al*. 2004, 2006; Han *et al*. 2008). By incorporating the idea of glass point and liquid point for the evaluation of heavy oil, Han et al. (2008) physically divided the heavy oil into three phases: solid phase, quasi-solid phase, and liquid phase, Figure 6.1, which offer a clear insight into the physical properties of heavy oil under different temperature conditions. As a consequence, such unique characteristic of heavy oil makes both the laboratory measurements and theoretical rock-physics modeling particularly challenging.

Heavy oil-sand is typically unconsolidated and held together by the viscous heavy

oil. As a result, it is easily fragile and highly attenuated, causing the unclear and weak wave signals. Therefore, direct measurements of P- and S- wave velocities for heavy oil-sand are still lacking. Obviously, the limited available data will hinder us to analyze the multiphase properties of heavy oil-sand reservoir, and further to calibrate the relevant rock-physics models.

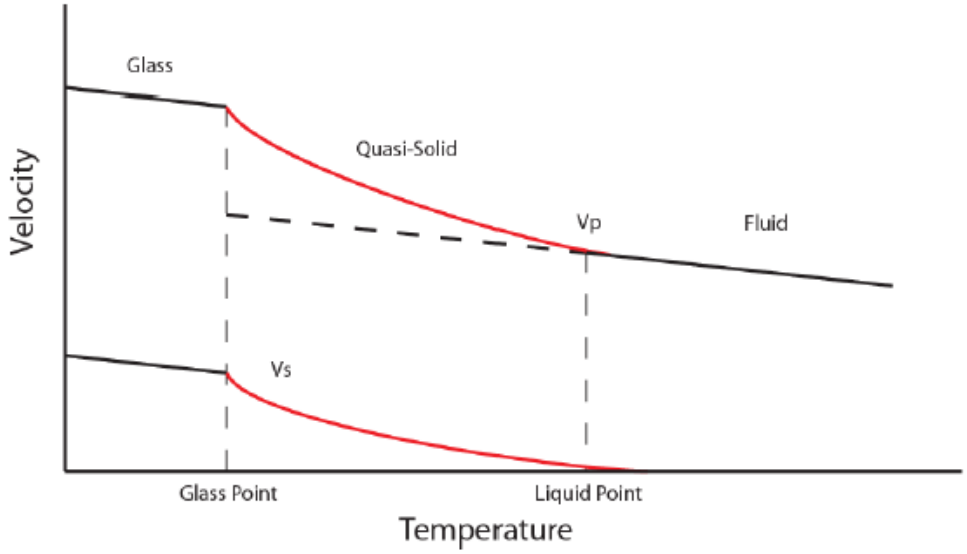

Figure 6.1 Schematic diagram of transition zone of heavy oil-phase as a function of temperature (adapted from Han *et al*, 2008).

Performing ultrasonic measurements and developing rock-physics models are both indispensable tools to understand and predict the complex elastic properties of heavy oil-sand (Han *et al*., 2006; 2007; 2008; Batzle *et al*., 2006; Rojas *et al*., 2008). Direct laboratory measurements give us reliable data to quantitatively understand the elastic properties of heavy oil and heavy oil-saturated sand. Meanwhile, the rock-physics modeling makes us reveal the physical law behind measured data and guides us to

quantitatively characterize fundamental micro-mechanism between the heavy oil and solid matrix.

Some rock-physics models on heavy oil-saturated rock are documented in the published literatures (Leurer and Dvorkin, 2006; Ciz and Shaprio, 2007; Kato and Han, 2008; Das and Batzle, 2009). Leurer and Dvorkin (2006) incorporated the Hertz-Mindlin grain-contact model (Mindlin, 1949) with viscoelastic theory to formulate effective-elastic properties of identical spherical solid grain packs-saturated with viscous heavy oil. Extended solid Gassmann-substitution, as proposed by Ciz and Shapiro (2007), extended the anisotropic Gassmann's equation (Brown and Korringa, 1975) to calculate elastic modulus of reservoir rock-saturated with temperature-dependent heavy oil. Based on ultrasonic velocity measurements on the samples of unconsolidated heavy oil-sand, an empirical rock-physics model was established along with Gassmann theory (Kato, 2010; Kato and Han, 2008). Das and Batzle (2009) integrated the self-consistent approach (Berrymann, 1980; 1992) and the differential effective-medium theory to estimate elastic properties of high-porosity heavy oil-sand and further compared them with the measured data.

To quantitatively investigate the role of a single phase in the sample integration of heavy oil-sand, we design and perform specific laboratory measurements to understand the effects of each components on the whole rock properties in this chapter. We build three samples of artificial heavy oil-sand, two of which are the mixtures of glass beads with heavy oil, another is extracted grains-saturated with heavy oil. We measure the P- and S-wave velocities under different conditions to simulate practically physical states of

heavy oil-sand reservoir. This chapter is organized as follows. First, we show the ultrasonic measurements of heavy oil and theoretically analyze the relevant factors that affect their elastic properties. And then we perform ultrasonic measurements on the three samples of heavy oil-sand under different conditions. Lastly, based on the ultrasonic measurements, we summarize the elastic properties of heavy oil-sand and analyze the possible physical mechanism behind these measured data.

6.3 Laboratory measurements

Laboratory measurement data are essential to calibrate the rock-physics models. The ultrasonic measurements are performed on both heavy oil and samples of heavy oil-saturated sands. The API density of the heavy oil is 6.6^{o}, which is used to saturate the glass beads/extracted sand packs. The sample #8 and #9 are mixtures of glass beads with heavy oil. The sample V3 is the extracted solid grains re-saturated with heavy oil. Their physical properties are listed in the Table 6.1.

Table 6.1: Physical parameters of heavy oil-sand samples

Sample ID	**Type**	**Porosity** %	**Grain density** (g/cm^3)	**Bulk density** (g/cm^3)		
				Dry	Water saturation saturation	Oil
#8	GB-HO	40.96	2.49	1.47	-	1.89
#9	GB-HO	35.90	2.49	1.60	1.95	1.96
V3	ES-HO	37.10	2.66	1.54	-	1.97

Note: "GB-HO" represents glass bead packs-saturated with heavy oil; "ES-HO" represents the extracted heavy oil-sand packs-saturated with heavy oil.

6.3.1 Ultrasonic measurements of heavy oil

Based on the measured sample length and travel time by ultrasonic pulse-receiver technique, the P-wave velocity is defined. However, it is difficult to recognize the transmitted shear signals, because of the intense attenuation in heavy oil. Hence, instead of direct measurement, the S-wave velocity is calculated by applying Han's S-wave model (2007), which considers S-wave velocity of heavy oil as a function of API and frequency. Technically, we estimate S-wave velocity using the FLAG program. By using the measured density at corresponding temperature and pressure conditions, the measured velocities are converted into modulus, which is more physically meaningful. Considering on phase-transition temperature of heavy oil and in-situ reservoir condition, we measure four typical temperature points for heavy oil (12 ^{o}C, 22 ^{o}C, 30 ^{o}C, and 60 ^{o}C, respectively), which mainly locate in the zone of quasi-solid phase.

6.3.1.1 Modulus as a function of pressure and temperature

Figure 6.2(a) shows that both the bulk and shear modulus of heavy oil increase linearly with increased pressure at a given temperature. At a given pressure, because the heavy oil becomes stiffer with increased temperature, the lower is the temperature, the higher is the bulk modulus. The shear modulus is almost zero when temperature rises upon to 60 ^{o}C, which exceeds the temperature of liquid point. Once the temperature is less than the temperature of liquid point, the shear modulus increases gradually. It suggests that the viscosity-induced modulus of heavy oil is significantly dominated by temperature. The increment of modulus caused by temperature and pressure is displayed

in Figure 6.2 (b) and (c), respectively. Specifically, for a given pressure condition of Figure 6.2(b), the increment of bulk modulus is almost constant as pressure increases. For the increment of shear modulus, first, the increment is much higher under low pressure point comparing with the increment of bulk modulus; second, the increment of shear modulus decreases dramatically as pressure increases, which suggests that the viscosity-induced shear modulus is more sensitive to the temperature. Under a given pressure condition, the increment of modulus is calculated using modulus at 22 ^{o}C and 60 ^{o}C, respectively. For the pressure effect, the bulk modulus increases of 30% as temperature increases. Meanwhile, it increases slightly as temperature increases. The increment of shear modulus keeps increasing temperature from 12 ^{o}C to 60 ^{o}C. At a given temperature, the increment of modulus is calculated by using modulus at 0.8 MPa and 48 MPa, Figure 6.2(c), respectively.

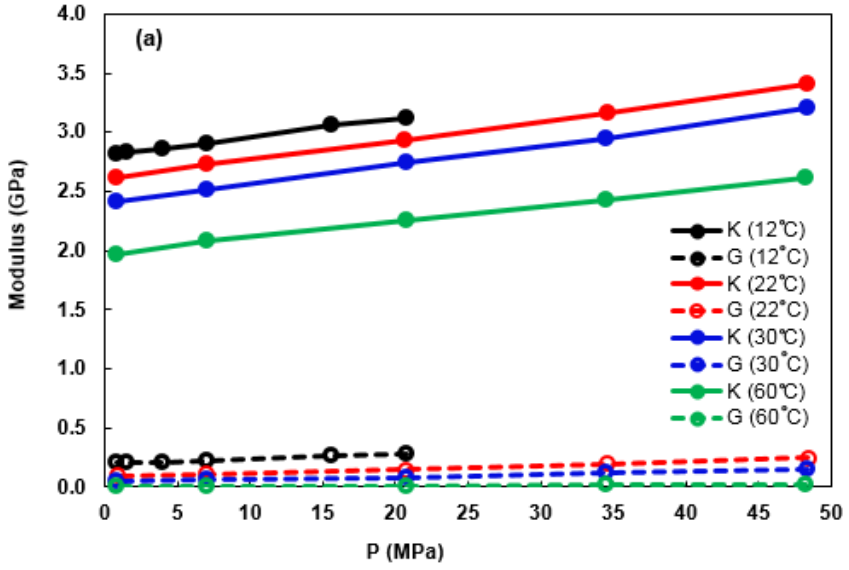

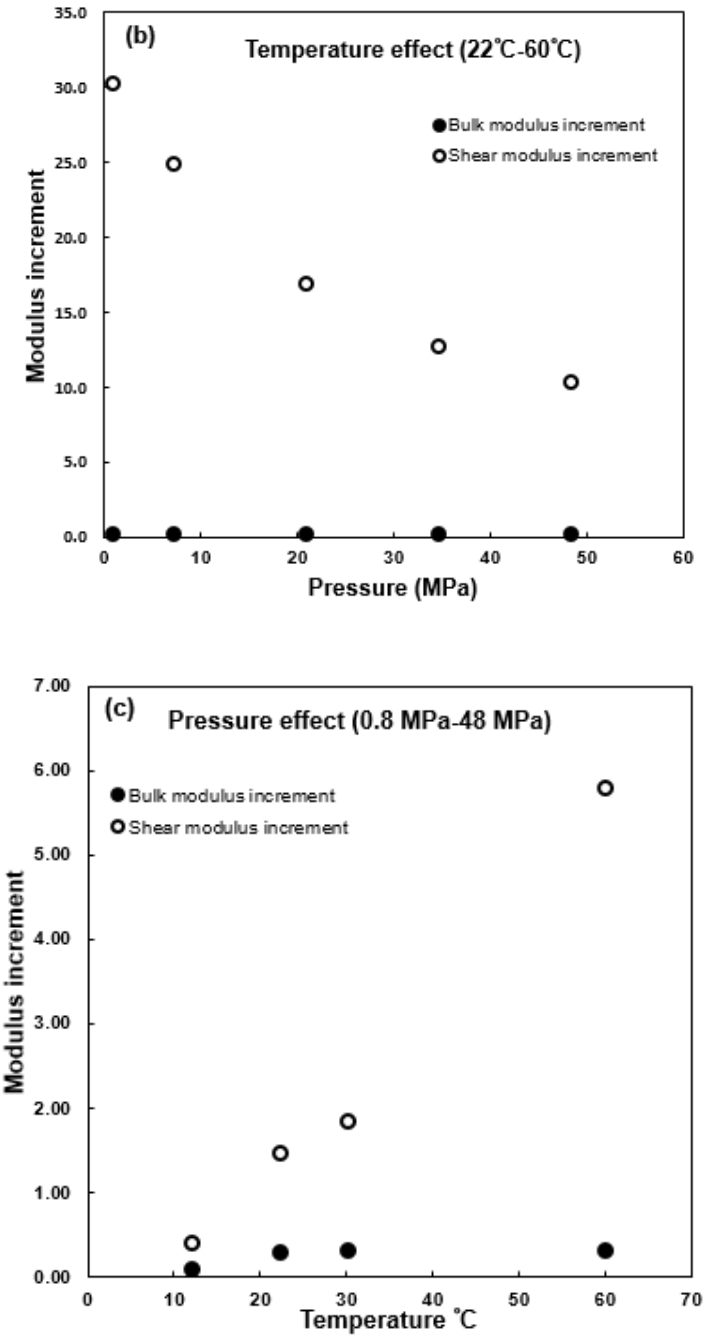

Figure 6.2 (a) Measured bulk modulus and calculated shear modulus of heavy oil against pressure; (b) Modulus increment against pressure; (c) Modulus increment against temperature.

6.3.1.2 Shear-viscosity as a function of temperature

The viscosity of heavy oil is extremely sensitive to temperature, especially when the measured temperature approaches both the temperatures of liquid point and glass point. Figure 6.3 shows that the viscosity decreases gradually with the increment of temperature. Usually, shear viscosity varies by orders of magnitude even for the same API gravity (Hinkle *et al*., 2008). The high shear-viscosity at low-temperature enables heavy oil to act as a part of solid frame, especially when the temperature is less than the temperature of glass point. Certainly, heavy oil at high-temperature could be treated as a movable liquid with no additional contribution to rock-solid frame. Namely, at temperature higher than the liquid point, the viscosity is so low that its effect on modulus can be neglected and acts as elastic material. Within these two stages, heavy oil acts as a viscoelastic material, where waves passing through are strongly dispersive with high attenuation. More importantly, heavy oil in the quasi-solid phase has a finite shear modulus-induced by the shear viscosity. In our case, the shear viscosity of heavy oil (API=6.6^{o}) is about 10^{15} cP at the glass point (-34.6 ^{o}C) while it quickly decreases to 10^{3} cP when temperature goes down to the liquid point (48.7 ^{o}C). Undoubtedly, the shear modulus is inevitably affected by the temperature-dependent viscosity.

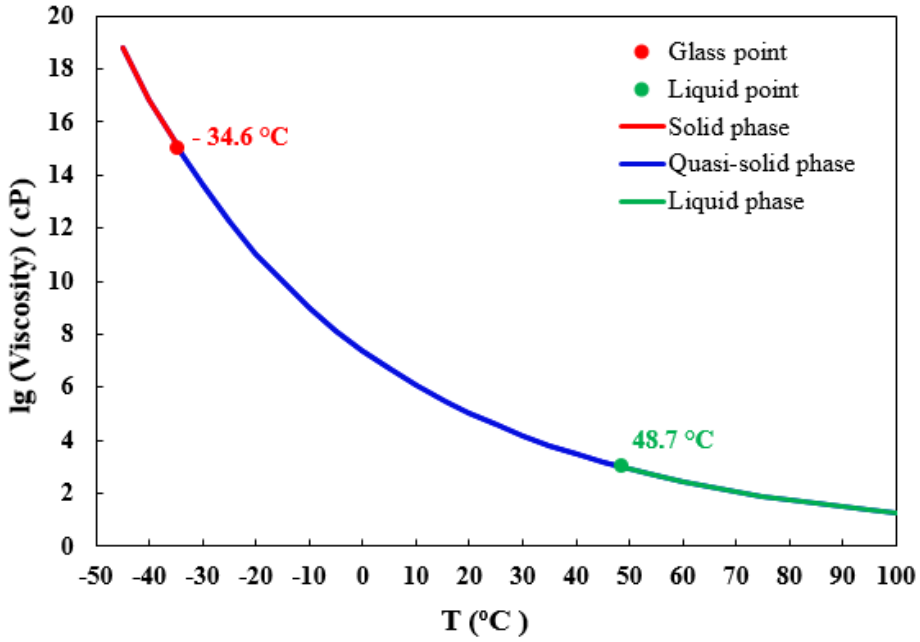

Figure 6.3 The shear viscosity of heavy oil against the temperature (API=6.6^{o}).

6.3.1.3 Velocity as a function of frequency

When temperature is within the quasi-solid zone, shear viscosity-induced shear modulus is non-negligible, even though the heavy oil is assumed as a Newtonian liquid at quasi-solid phase (Song, 1986). For a Newtonian liquid, the viscosities are frequency-dependent. It leads to viscosity-induced velocity dispersion with high attenuation. Figure 6.4 shows both the P- and S-wave velocities increase as frequency increases. The velocity dispersion is predicted by the modified Havriliak-Negami model using the FLAG program. Both P- and S-wave velocities increase from seismic frequency range to ultrasonic frequency range. Moreover, Figure 6.4 (b) suggests that the S-wave is more dispersive than that of P-wave. It is because the shear and bulk viscosity synergistic

effect, although bulk viscosity is often simply assumed to be 0 (Das and Batzle, 2009). Additionally, at a given temperature, the velocity curve indicates that the P-wave velocity is slightly higher at high-pressure (7MPa) than that of at low-pressure (0.8 MPa) in the whole frequency range. The velocity dispersion of heavy oil decreases as temperature increases until P-wave velocity remains constant, and heavy oil transfers to elastic standard fluid when temperature (60 ^{o}C) is greater than the temperature of liquid point (48.7 ^{o}C). Experimentally, the measured P-wave velocity (1MHz, 12 ^{o}C) matches well with theoretical prediction under both low- and high- pressure in the quasi-solid phase. The S-wave velocity is closely related to the frequency, temperature, and pressure displays the same trend as the P-wave does.

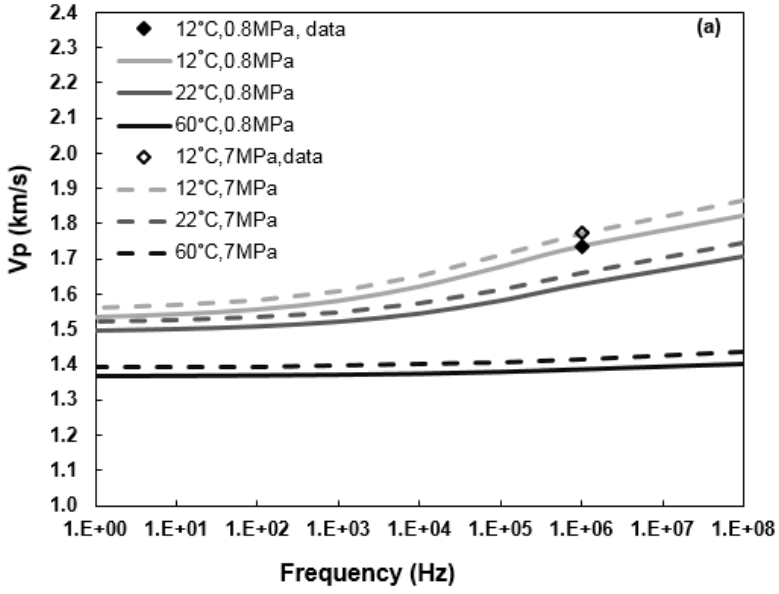

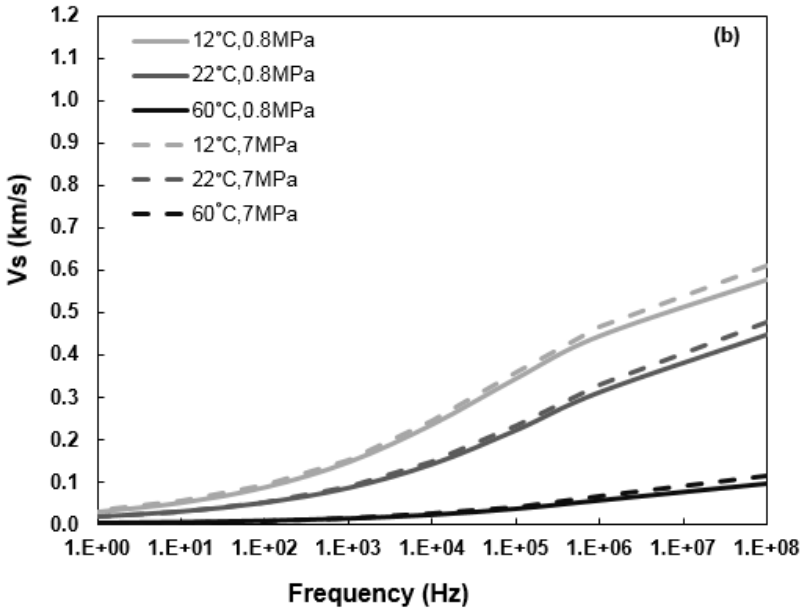

Figure 6.4 (a) P-wave velocity against frequency; (b) S-wave velocity against frequency.

From above laboratory measurements and theoretical model prediction of heavy oil, it can conclude that the temperature is the first order factor to determine the viscosity of heavy oil. The viscosity-induced modulus is temperature-dependent. Meanwhile, the Newtonian liquid feature of heavy oil in the quasi-solid phase enables the wave velocities of heavy oil to be frequency-dependent. As an essential part of heavy oil-sand reservoir, these unique properties of heavy oil will undoubtedly determine the elastic properties of heavy oil-sand. Hence, we will perform specific measurements to investigate the role of heavy oil in the heavy oil-sand sample under different conditions.

6.3.2 Ultrasonic measurements of heavy oil-saturated sands

Three artificial samples are measured under both dry and saturated conditions in a

single run. The ultrasonic measurements procedure contains two loading and unloading cycles at dry condition, the length variation is monitored during the loading/unloading cycles. Then four loading and unloading cycles are performed for the saturated samples at designed temperature/pressure conditions.

The dry-solid packs are first measured at as-is condition before measuring the heavy oil-saturated grain-solid samples. Two technique tricks are taken to ensure the dry-solid pack fully saturated. First, controlling the rate of fluid injection as low as 0.01 *ml/cc*; second, the fluid is injected from the bottom of sample and observed in the outlets of upper pore channel. Then the sample is kept for three hours to make sure that no air trapped inside the sample. Meanwhile, in order to quantify the effect of fluid type, the sample #9 goes through water-saturation cycle firstly, and then replaced by the heavy oil. Four typical temperature points within quasi-solid zone (12 ^{o}C, 22 ^{o}C, 30 ^{o}C, and 60 ^{o}C, respectively) are measured samples of heavy oil-saturated sands.

6.3.2.1 Effect of pressure on elastic modulus of solid frame under as-is dry condition

To analyze pressure-dependent elastic modulus at "as-is" grain packs samples, the dry modulus are measured at the second pressure cycle. Figure 6.5 shows both the bulk modulus and shear modulus of dry solid pack steadily increases with increased pressure. But the increment of bulk modulus continuously increases as pressure decreases. This is because the micro-crack and soft pores are quickly closed as pressure increases. Due to the porosity effect, the bulk modulus satisfy: sample #9 (ϕ=35.90%) ＞sample #8

(ϕ=40.96%) ＞sample V3 (ϕ=42.10%). For the shear modulus, the sample V3 is higher than the samples #8 and #9, and the discrepancy continuously increases. This is likely to be caused by the smoothness of grain surface, which is considered to be the first order factor of influencing the shear modulus. Because the grain solids of sample V3 is from the extracted heavy oil-sand sample, which has been through complicated long-term geological process comparing with the artificial glass beads.

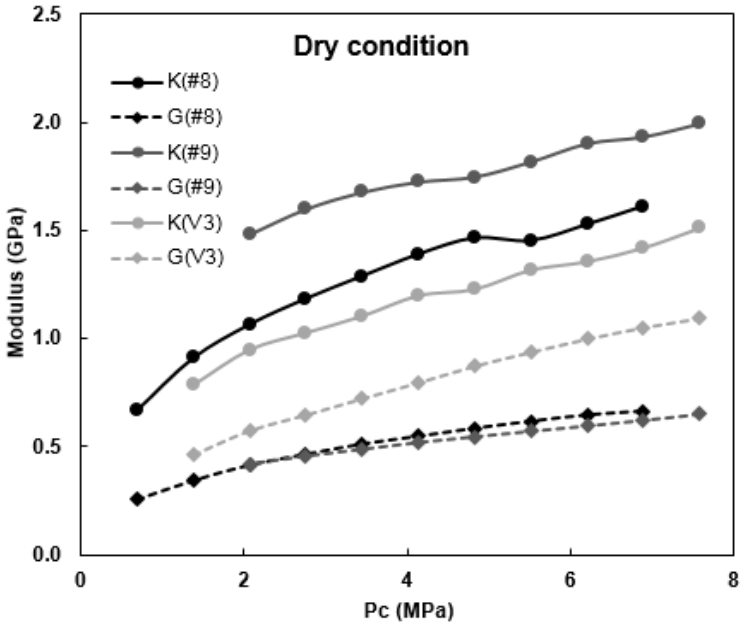

Figure 6.5 Modulus of dry-solid packs against confining pressure.

6.3.2.2 Effect of pressure on elastic modulus of heavy oil-saturated sands

At a given temperature point, both the bulk modulus and shear modulus of heavy oil-saturated solid samples steadily increase as pressure increases, Figure 6.6. Specifically, the bulk modulus exhibit the highest increment at temperature of 12 ^{o}C, then it remains

almost constant as temperature increases, Table 6.2(a). While the increment of shear modulus continuously increases as temperature increases, Table 6.2(b). Due to mostly measured temperature point within quasi-solid phase, it makes the modulus of heavy oil-saturated sand sample to be majorly determined by the elastic properties of heavy oil, which is mainly influenced by temperature.

Table 6.2a: Effect of pressure on bulk modulus

Sample	12°C	20/25°C	40°C	60°C
#8	2.00	0.07	0.09	0.20
#9	1.88	0.09	0.09	0.11
V3	0.06	0.08	0.06	0.11

Table 6.2b: Effect of pressure on shear modulus

Sample	12°C	20/25°C	40°C	60°C
#8	0.05	0.10	0.21	0.30
#9	0.17	0.07	0.18	0.24
V3	0.11	0.08	0.16	0.31

Note: Calculation of the effect of pressure on P-wave velocity using measured modulus at 1100 psi and 500 psi, respectively. The increment equation is $I = \frac{M^{1100\,psi} - M^{500\,psi}}{M^{500\,psi}}$, where $M^{1100\,psi}$ is modulus at 1100 Psi, and $M^{500\,psi}$ is modulus at 500 psi.

The water-saturation procedure has no primary impact on the elastic properties of heavy oil-saturated solid sample comparing the sample #8 with the sample #9. The results show, firstly, the modulus of fully water-saturated sample at room condition (25 °C) is even lower than that of fully heavy oil saturated sample at 60 °C because of the low viscosity of water (1 cP).

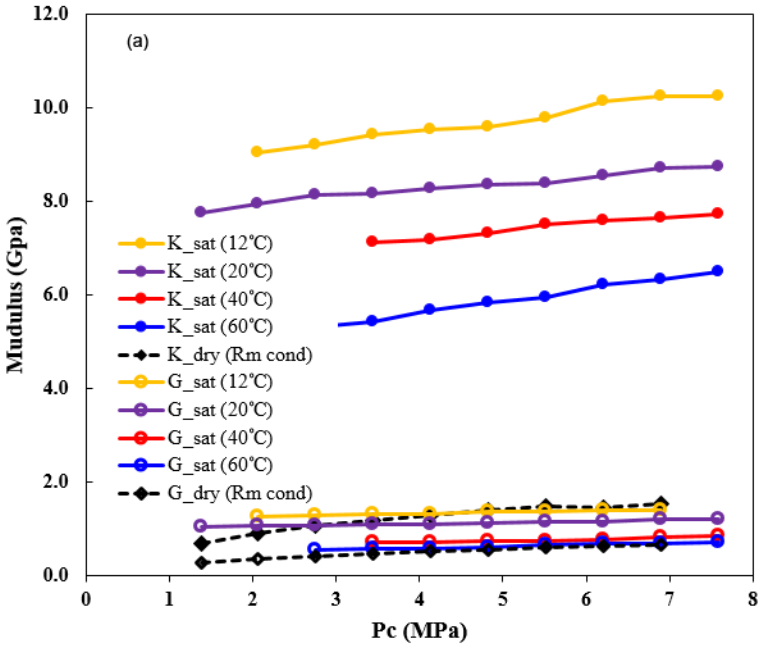
(a)
Mudulus (Gpa)
Pc (MPa)
K_sat (12℃)
K_sat (20℃)
K_sat (40℃)
K_sat (60℃)
K_dry (Rm cond)
G_sat (12℃)
G_sat (20℃)
G_sat (40℃)
G_sat (60℃)
G_dry (Rm cond)

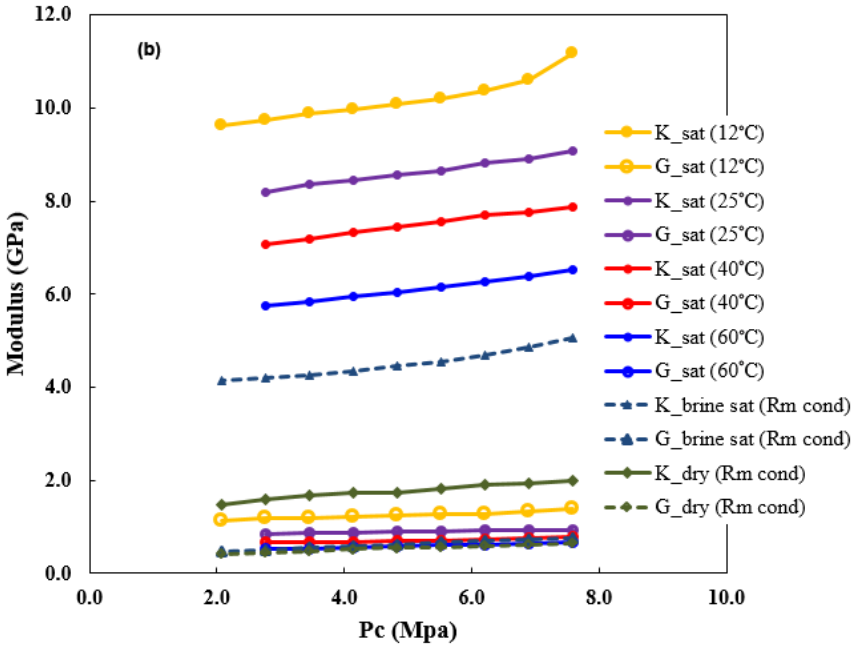
(b)
Modulus (GPa)
Pc (Mpa)
K_sat (12°C)
G_sat (12°C)
K_sat (25°C)
G_sat (25°C)
K_sat (40°C)
G_sat (40°C)
K_sat (60°C)
G_sat (60°C)
K_brine sat (Rm cond)
G_brine sat (Rm cond)
K_dry (Rm cond)
G_dry (Rm cond)

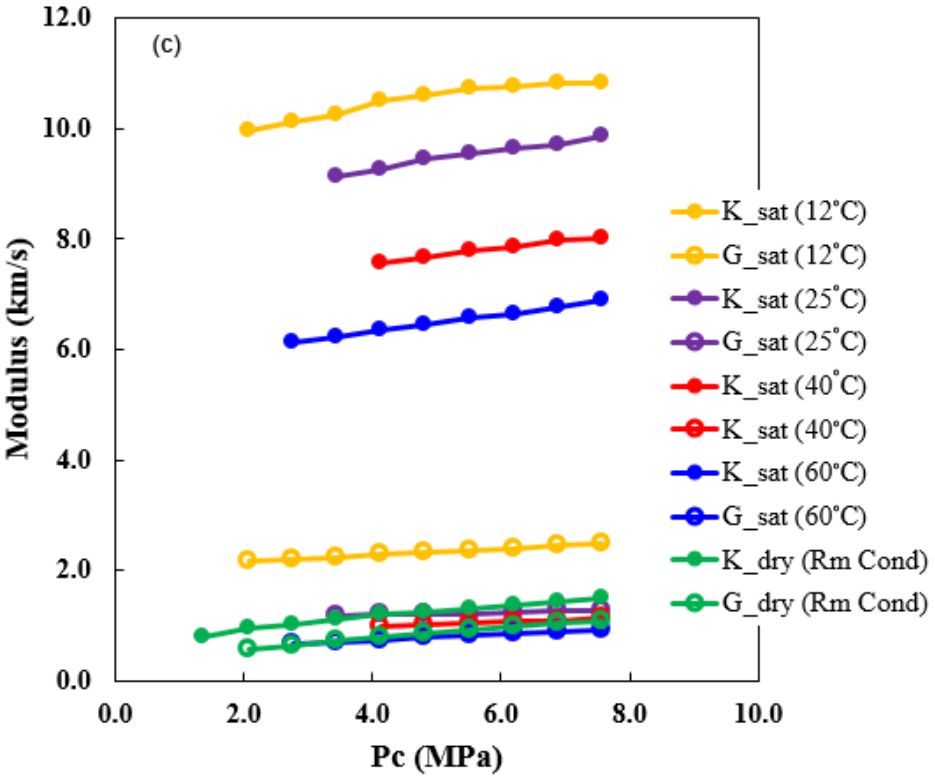

Figure 6.6 Modulus against confining pressure. (a) Sample #8; (b) Sample #9; (c) Sample V3 (c).

6.3.2.3 Effect of temperature on elastic modulus of heavy oil-saturated sands

As temperature increases, the bulk and shear modulus significantly decrease in the quasi-solid stage, Figure 6.7. In contrast, in the high temperature range, the bulk modulus gently decreases, whereas the shear modulus virtually remains constant. The behavior in the low temperature range is associated with the viscoelastic feature, that the bulk and shear modulus of heavy oil are enforced by the corresponding viscosities (Nur et al., 1984; Easterwood, 1993; Schmitt, 1999; Batzle et al., 2006). Moreover, the systematic pressure effects are also observable.

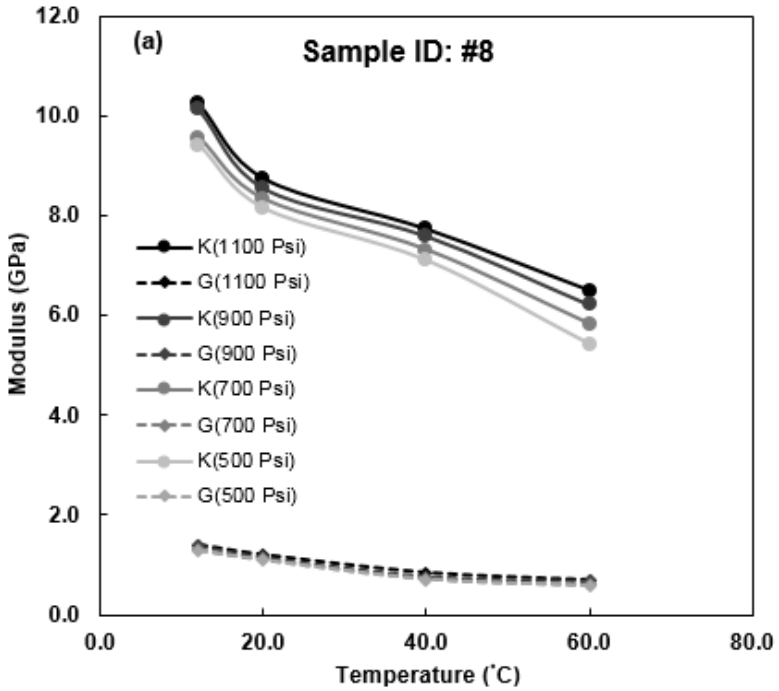
(a)
Sample ID: #8
Modulus (GPa)
Temperature (˚C)
K(1100 Psi)
G(1100 Psi)
K(900 Psi)
G(900 Psi)
K(700 Psi)
G(700 Psi)
K(500 Psi)
G(500 Psi)
12.0
10.0
8.0
6.0
4.0
2.0
0.0
0.0
20.0
40.0
60.0
80.0

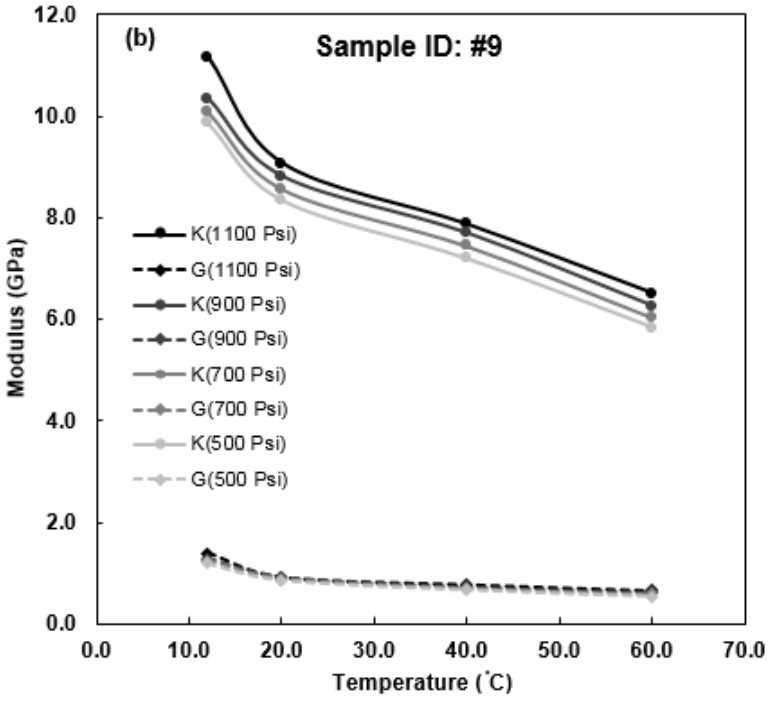
(b)
Sample ID: #9
Modulus (GPa)
Temperature (˚C)
K(1100 Psi)
G(1100 Psi)
K(900 Psi)
G(900 Psi)
K(700 Psi)
G(700 Psi)
K(500 Psi)
G(500 Psi)
12.0
10.0
8.0
6.0
4.0
2.0
0.0
0.0
10.0
20.0
30.0
40.0
50.0
60.0
70.0

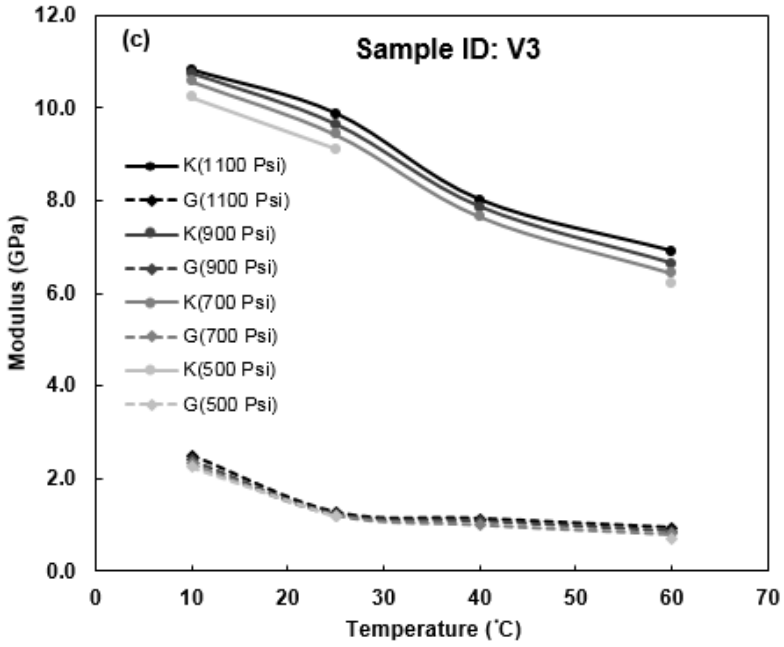

Figure 6.7 Modulus of heavy oil-saturated sand samples as a function of temperature. (a) sample #8; (b) sample #9; (c) sample V3.

Figure 6.8 (a) displays the temperature effects on elastic modulus for all three heavy oil-saturated solids samples. It again suggests that the temperature is the first order factor to determine the viscosity-induced modulus of heavy oil, which, in turn, makes the elastic properties of heavy oil-saturated solids being temperature-dependent.

The increment of elastic modulus is a significant indicator to characterize the temperature sensitivity on modulus. Under a given pressure, the modulus increment is calculated using the reference modulus at 60 ^{o}C and 12 ^{o}C, respectively. Figure 6.8 (b) shows that the shear modulus of heavy oil-saturated solids is more temperature sensitive. Especially, the increment ratio of shear modulus of samples #8 and #9 is about 1, whereas

that of sample V3 reaches 2.2 at low pressure and decreases gradually as pressure decreases. The viscosity-induced shear modulus of heavy oil increases significantly when the temperature is closed to the glass point. In contrast, the bulk modulus increases at a reduced rate when increasing shear viscosity from liquid point (Kato, 2010).

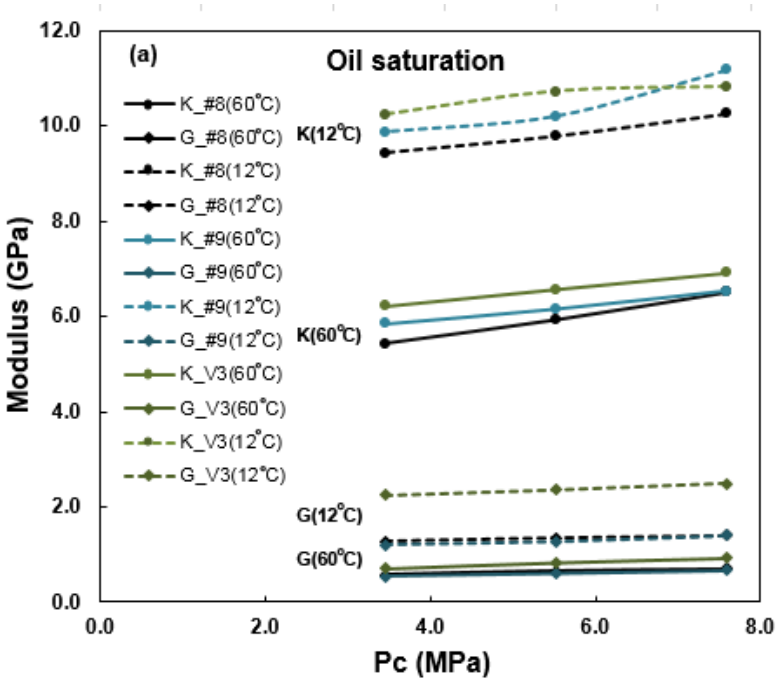

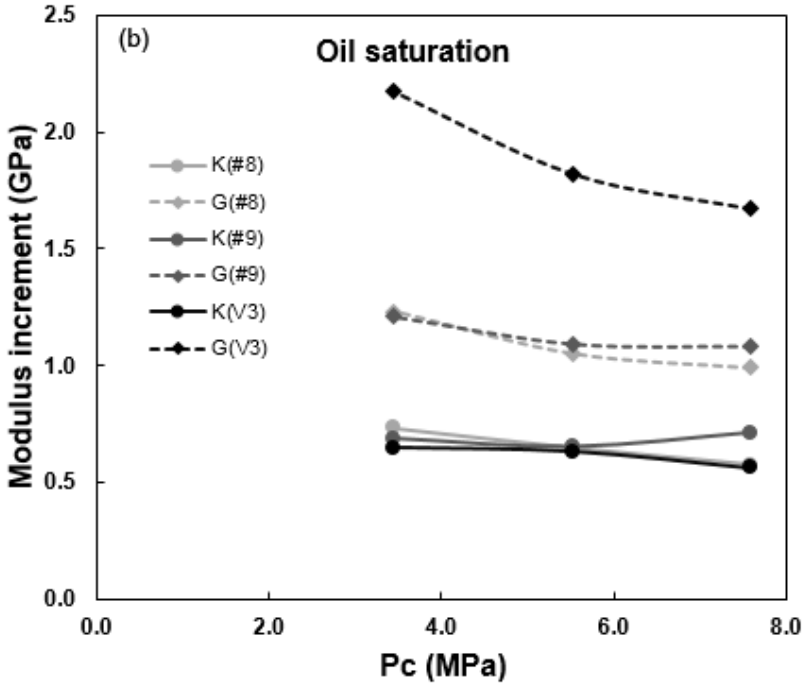

Figure 6.8 (a) Temperature effects comparison on both bulk modulus and shear modulus after heavy oil-saturation; (b) modulus increment.

6.3.2.4 Other effects on elastic modulus of heavy oil-saturated sands

The microstructure and elastic properties of solids may be another factors influencing the elastic modulus of heavy oil-sand. For example, both samples #8 and #9 are made of glass beads, however, the bulk modulus of sample #9 is higher than that of sample #8 at 12 ^{o}C, which can be explained by the porosity, which is a critical parameter to characterize the microstructure of random granular packs. Furthermore, due to the difference of elastic properties of quartz sands and glass bead, the sample V3 has a highest bulk modulus with the highest porosity. The grain surface of sample V3 is rough due to the complicated long-term geological process. We also can observe that the sample

V3 has the highest increment of shear modulus. The smoothness of grain surface is critical factor to influence the shear stiffness as well.

6.4 Discussions

On the basis of above experimental results, we can summarize that the temperature, pressure, and microstructure are the main factors to influence the elastic properties of heavy oil-saturated solid matrix due to the variable characteristics of heavy oils itself.

6.4.1 The dominant effect of heavy oil on rock-physics modeling

It is no doubt that the unique characteristics of heavy oil dominate the entire properties of heavy oil-sand rocks. The temperature-dependent viscosity spans from 10^{15} cP at glass point to 10^{3} cP at liquid point. The laboratory measurements confirm Han's model (Han, *et al.*, 2008) that heavy oil can be regarded as a part of rock frame when the temperature is less than that of the glass point. However, it changes to completely movable pore fluid when the temperature is greater than that of the liquid point. As a consequence, at the low-temperature range of quasi-solid stage of heavy oil, the solid Gassmann's equation makes an underestimation between the predicted both P- and S-wave velocities and measured data. It may be because partial heavy oil turns into solid frame at low temperature, which does not count well by the solid Gassmann's equation. The solid Gassmann's equation works well as temperature increases till reaching liquid point, it is due to the heavy oil starts to transfer into moveable pore filling materials with less shear viscosity. Once the temperature exceeds the liquid point, the solid Gassmann's

again overestimates the measured data. The high temperature resulting in the variation of grain-solid frame of heavy oil-sand may cause this phenomenon, Figure 6.9.

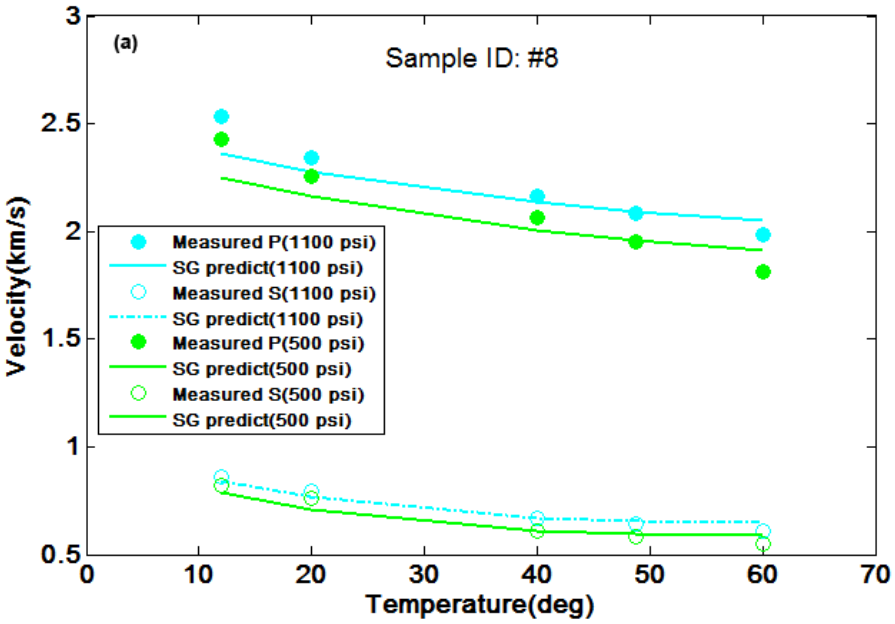

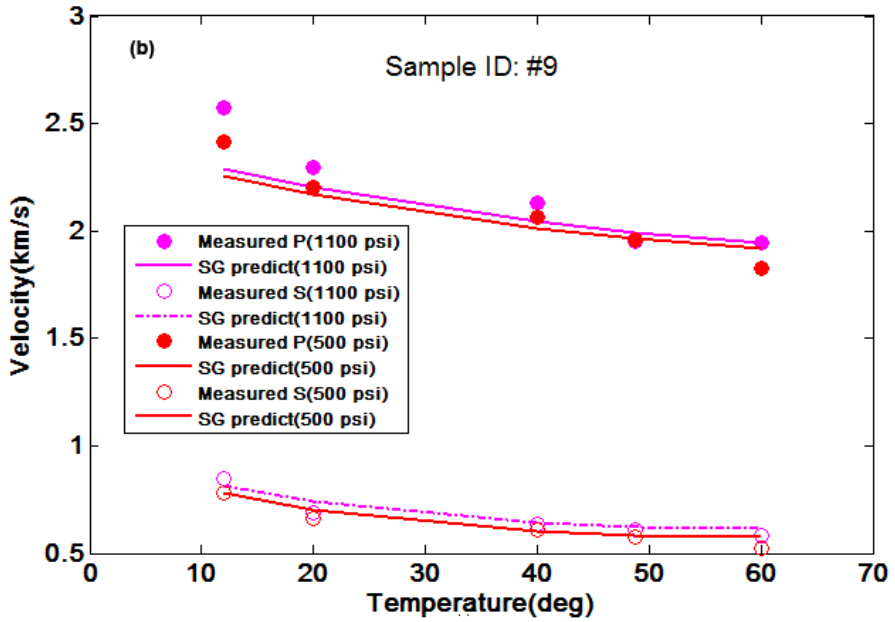

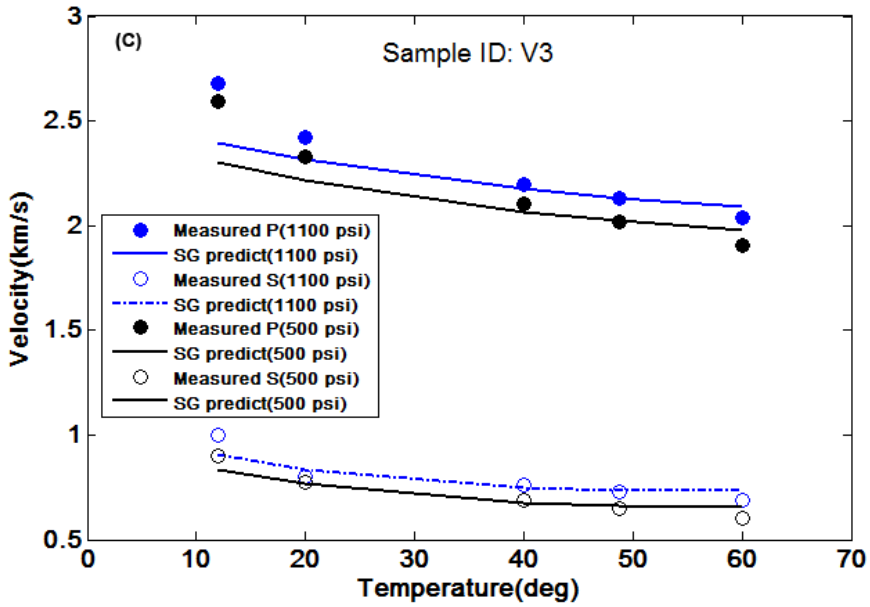

Figure 6.9 Solid Gassmann'S equation predicts velocity against temperature with measured data.

Robust rock-physics model to link the physical properties of heavy oil-saturated rock with seismic data is a feasible tool to precisely characterize the reservoirs. Sensitive temperature-dependent shear viscosity of heavy oil at quasi-solid state violates assumptions of classical Gassmann's equation (Gassmann, 1951), which makes fluid substitution in the heavy oil-saturated rock non-applicable (Makarynska *et al.*, 2010). Even for the extended solid Gassmann's equation cannot well handle the heavy oil saturated rock because of temperature-dependent properties of heavy oil. Therefore, quantitatively characterizing heavy oil-saturated sand is challenging but an indispensable step in theoretical modeling. The key point of capturing the elastic properties of heavy

oil-sand rock is to incorporate the temperature-dependent properties of heavy oil into the rock-physics model. It allows us to physically understand how the heavy oils determine the elastic properties of heavy oil-sand rocks.

6.5 Conclusions

Experimental observations of elastic properties of heavy oil and heavy oil-saturated grain-solid matrix suggest that the elastic properties of heavy oil sands influenced by multiphase of heavy oil itself and solid matrix with respect to the temperature, pressure, and microstructure. Moreover, the intrinsic feature of viscosity-induced heavy oil properties dominates the elastic properties of heavy oil saturated sand rock. Namely, the temperature, as the external condition, is the first order factor to determine the elastic properties of heavy oil-saturated sand sample. In addition, because of temperature-dependent heavy oil, the transitional microstructure of heavy oil-sand demands us to build up new rock-physics model to characterize the ambiguity of heavy oils in each temperature segment instead of using universal rock physics model in the entire temperature range.

7. References

Adam, L., M. L., Batzle, and K. T., Lewallen, 2009, Seismic wave attenuation in carbonates, Journal of Geophysical Research, **114**, B06208.

Ali, S. A., W. J. Clark, W. R., Moore, and J. R. Dribus, 2010, Diagegesis and reservoir quality, Oilfield review, **22**, 14-27.

Allen, J. P. L., 1991, The Bouma division A and the possible duration of turbidity currents, Journal of Sedimentary Petrology, **61**, 291-295.

Allen, J. C., 1973, Method for recovering viscous oils by solvent extraction. Canadian Patent No. 1008361, Texaco Development.

Aki, K. and P. G., Richards, 1980, Quantitative seismology: Theory and methods, W. H. Freeman & Co.

Avseth, P., 2000, Combining rock physics and sedimentology for seismic reservoir characterization in North Sea turbidite system [Ph.D. thesis], Stanford University.

Avseth, P., J. Dvorkin, G. Mavko, and J. Rykkje, 2000, Rock physics diagnostic of North Sea sands: Linking between microstructure and seismic properties. Geophysical Research Letters, **27**, 2671-2764.

Avseth, P., T. Mukerji, and G. Mavko, 2005, Quantitative seismic interpretation: Applying rock physics tools to reduce interpretation risk, Cambridge University Press.

Avseth, P., T. Mukerji, G. Mavko, and J. Dvorkin, 2010, Rock-physics diagnostics of depositional texture, diagenetic alterations, and reservoir heterogeneity in high-porosity siliciclastic sediments and rocks—A review of selected models and suggested work flow, Geophysics, **75**, 75A31-75A47.

Bachrach, R. and P. Avseth, 2008, Rock physics modeling of unconsolidated sands: Accounting for nonuniform contacts and heterogeneous stress fields in the effective media approximation with applications to hydrocarbon exploration, Geophysics, **73**, E197–E209.

Bahrami M, M. M. Yovanovich, and J. R. Culham, 2005, A compact model for spherical rough contacts, Journal of Tribology, **127**, 884-889.

Batzle, M. L., R., Hofmann, and D. H., Han, 2006, Heavy oils-Seismic properties. The Leading Edge, **25**, 750-756.

Batzle, M. L., D. H. Han, and R. Hofmann, 2006, Fluid mobility and frequency-dependent seismic velocity—Direct measurements, Geophysics, **71**, 1–N9.

Batzle, M. L., B., Zadler, R., Hofmann, and D. H., Han, 2004. Heavy oils-Seismic properties. 74th Annual International Meeting, SEG, Expanded Abstracts, 1762-1765.

Berryman, J. G., 1980, Long-wavelength propagation in composite elastic media II. Ellipsoidal inclusions: Journal of the Acoustical Society of America, **68**, 1980-1831.

Berryman, J. G., 1992, Single-scattering approximations for coefficients in Biot's equations of poroelasticity: Journal of the Acoustical Society of America, **91**, 551-571.

Berryman, J. G., 1994, Role of porosity in estimates of composite elastic constants, Journal of Energy Resource, **116**, 87-96.

Berryman, J. G., and H. F. Wang, 2000, Elastic wave propagation and attenuation in a double-porosity dual-permeability medium, Int. J. Rock Mech. Min.Sci., **37**, 63– 78.

Biot, M. A., 1956a, Theory of propagation of elastic waves in a fluid-saturated porous solid: Part1—Low-frequency range, Journal of the Acoustical Society of America, **28**, 168–178.

———, 1956b, Theory of propagation of elastic waves in a fluid-saturated porous solid: Part2— Higher frequency range, Journal of the Acoustical Society of America, **28**, 179–191.

———, 1962, Mechanics of deformation and acoustic propagation in porous media, Journal of Applied Physics, **33**, 1482–1498.

Bourbié, T., O. Coussy, and B. Zinszner, 1987, Acoustics of porous media, Editions Technip.

Brandt, H., 1955, A study of the speed of sound in porous granular materials, Journal of Applied Mechanics, **22**, 479-486.

Brown, A., C. H., Wu, and D. T., Konopnicki, 1977, Combined multiple solvent and thermal heavy oil recovery. United States Patent No. 4004636, Texaco, New York.

Brown, R., and J., Korringa, 1975, On the dependence of the elastic properties of a porous rock on the compressibility of the pore fluid: Geophysics, **40**, 608-616.

Cadoret, T., D., Marion, and B., Zinsner, 1993, Influence of frequency fluid distribution on elastic wave velocities in partial saturated limestones, Journal of Geophysical Research, **100**, 9789-9803.

Carcione, J. M. and F. Cavallini, 2002, Poisson's ratio at high pre pressure, Geophysical Prospecting, 50, 97-106.

Chen, Y. and T. F. Huang, 2001, Rock Physics (in Chinese), Beijing: Peking University Press.

Ciz, R., and Shapiro, S., 2007. Generalization of Gassmann equations for porous media saturated with a solid material: Geophysics, **72**, A75–A79.

Chester, J. S., S. C. Lenz, F. M. Chester, and R. A. Lang, 2004, Mechanics of compaction of quartz sand at diagenetic conditions, Earth and Planetary Science Letters, **220**, 435-451.

Choquette, P. W. and L. C. Pray, 1970, Geologic nomenclature and classification of porosity in sedimentary carbonates, AAPG Bulletin, **54**, 207-250.

Curtis, C., Kopper, R., Decoster, E., Garcia, A.G., Huggins, C., Knauer, L., Minner., Kupsch, N., Linares, L.M., Rough, H., and White, M., 2002. Heavy-oil reservoirs. Oilfiled Review, **14**, 30-51.

Czichos, H., T. Saito, and L. Smith, 2006, Springer handbook of materials measurement methods, Springer.

Das, S. K., 1995. In situ recovery of heavy oil and bitumen using vaporized hydrocarbon solvents. PhD thesis, University of Calgary, Canada.

Das, A., 2010, The viscoelastic properties of heavy-oil saturated rocks [Ph.D. dissertation], Colorado School of Mines.

Das, A., and Batzle, M., 2009, A combined effective medium approach for modeling the viscoelastic properties of heavy oil reservoirs: 79th Annual International Meeting, SEG, Expanded Abstracts, 2110-2114.

De Segonzac, 1968, The birth and development of the concept of diagenesis, Earth Science Review, **4**, 153-201.

Deng J. X., D. H. Han, and S. X. Wang, 2011, A study of the influence of stress relaxation on the elastic properties of granular materials and the calibration of effective media model. Chinese Journal of Geophysics (in Chinese), **54**, 1079-1089.

Digby, P. J., 1981, The effective elastic modulus of porous granular rocks, Journal of Applied Mechanics, **48**, 803-808.

Domenico, S. N., 1976, Effect of brine-gas mixture on velocity in an unconsolidated sand reservoir, Geophysics, **41**, 882–894.

Domenico, S. N., 1977, Elastic properties of unconsolidated porous sand reservoirs, Geophysics, **42**, 1339–1368.

Domenico, S. N., 1984, Rock lithology and porosity determination from shear and compressional wave velocity, Geophysics, **32**, 1188-1195.

Duffaut, K. M., M. Landrø, and R. Sollie, 2010, Using Mindlin theory to model friction-dependent shear modulus in granular media, Geophysics, **75**, E143–E152.

Dunn, M. L., and H., Ledbetter, 1995, Poisson's ratio of porous and microcracked solids: theory and application to oxide superconductors, Journal of Materials Research, **10**, 2715-2722.

Dutta, T., G. Mavko, and T. Mukerji, 2010, Improved granular medium model for unconsolidated sands using coordination number, porosity, and pressure relations, Geophysics, **75**, 91-99.

Dvorkin, J. and A. Nur, 1996, Elasticity of high-porosity sandstones: Theory for two North Sea data sets, Geophysics, **61**, 1363-1370.

Dvorkin, J., A. Nur, and H. Z. Yin, 1994, Effective properties of cemented granular materials, Mechanics of Materials, **18**, 351-366.

Dvorkin, J., J. Berryman, and A .Nur, 1999, Elastic modulus of cemented sphere packs, Mechanics of Materials, **31**, 461-469.

Dvorkin, J. and H. Z. Yin, 1995, Contact laws for cemented grains: Implications for grain and cement failure, International Journal of Solids and Structures, **32**, 2497-2510.

Dvorkin, J. and M. A. Gutierrez, 2001, Textural sorting effect on elastic velocities, part II: Elasticity of a bimodal grain mixture, Society of Exploration Geophysicists Annual Meeting, Expanded Abstract.

Eastwood, J., 1993, Temperature-dependent propagation of P-waves and S-waves in Cold Lake oil sands: Comparison of theory and experiment: Geophysics, **58**, 863-872.

Gassmann, F., 1951, Uber die Elastizitat poroser medien. Veirteljahrasschrift der

Naturforschen- den Gesellschaft in Zurich, **96**, 1-23.

Gautam, K., 2003, Fluid Effects on attenuation and dispersion of elastic waves [M.Sc. thesis], Colorado School of Mines, Golden, Colorado.

Geng, J. F., D., Howell, E. Longhi, R. P., Behringer, L., Reydellet, L., Vanel, E. Clement, and S. Luding, 2001, Footprints in the sands: The response of granular material to local perturbations, Physical Review Letters, **87**, 035506.

Gist, G. A., 1994, Interpreting laboratory velocity measurements in partially gas-saturated rocks, Geophysics, **59**, 1100–1109.

Gregory, A. R., 1976, Fluid saturation effects on dynamic elastic properties of sedimentary rocks, Geophysics, **41**, 895–921.

Gueguen, Yves, and V. Palciauskas, 1994, Introduction to the physics of rocks, Princeton University Press.

Hagin, P. N., and M. D., Zoback, 2004, Viscous deformation of unconsolidated sands—Part 1: Time-dependent deformation, frequency dispersion, and attenuation, Geophysics, **69**, 731-741.

Han, D. H., 1986, Effects of porosity and clay content on acoustic properties of sandstones and unconsolidated sediments [Ph.D. dissertation], Stanford University.

Han, D. H., and Liu, J. J., 2007, Temperature and frequency models of shear wave in heavy oil: DHI/Fluids annual report.

Han, D. H., Liu, J. J., and Batzle, M. L., 2006, Acoustic property of heavy oil-measured data. 76th Annual International Meeting, SEG, Expanded Abstracts, 1903–1907.

----- 2008. Seismic properties of heavy oils-measured data. The Leading Edge, 1108-1114.

Han, D. H., Liu J. J., and Baztle, M. L., 2008, Seismic properties of heavy oils-measured data. The Leading Edge, 1108-1114.

Han, D. H., and M. L. Batzle, 2004, Gassmann's equation and fluid-saturation effects on seismic velocities, Geophysics, **69**, 398–406.

Han, D. H., and Q. Yao, 2009, Intrinsic seismic wave attenuation—Tight gas sand example, Annual Report, Fluids/DHI Consortium.

Han, D. H., Yao, Q. L., and Zhao, H. Z., 2007, Challenges in heavy oil sand measurements, DHI/Fluids annual report.

Hashin, Z., and S., Shtrikman, 1963, A variational approach to the elastic behavior of multiphase minerals: Journal of the Mechanics and Physics of Solids, **11**, 127-140.

Hertz, H., 1884, Ueber die Berührung fester elastischer Körper, Journal für die reine und angewandte Mathematik, **92**, 156-171.

Hinkle, A., E. J., Shin, M. W., Liberatore, A. M., Herring, and M. L., Batzle, 2008. Correlating the chemical and physical properties of a set of heavy oils from around the world. Fuel, **87**, 3065-3070.

Jenkins, J. T., and M. A., Koenders, 2005, The incremental response of random aggregates of identical round particles, European Physical Journal, **13**, 113-123.

Ji, S. C., 2004, A generalized mixture rule for estimating the viscosity of solid-liquid suspensions and mechanical properties of polyphase rocks and composite materials, Journal of Geophysical Research, **109**, B10207.

Johnson, K. L., 1988, Contact mechanics, Cambridge University Press.

Jones, T. D., 1986, Pore fluids and frequency-dependent wave propagation in rocks, Geophysics, **51**, 1939–1953

Kato, A., and D. H., Han, 2008, Volume viscosity and its induced bulk modulus of heavy oil, Fluids/DHI consortium.

Kato, A., 2010, Reservoir characterization and steam monitoring in heavy oil reservoirs. PhD thesis, University of Houston.

Kithas, B. A., 1976, Lithology, gas detection and rock properties from acoustic logging system, SPWLA 17th annual Logging Symposium, R1-R10.
Kolbuszewski, J. J., 1948, Proceedings, 2nd International Conference of Soil Mechanics, **1**, p. 158.

Krumbein, W. C., 1942, Physical and chemical changes in sediments after deposition, Journal of Sedimentary Petrology, **12**, 111-117.

Leurer, K. C., and J. Dvorkin, 2006, Viscoelasticity of precompacted unconsolidated sand with viscous cement: Geophysics, **71**, T31-T40.

Liner, C. L., 2012, Elements of seismic dispersion: A somewhat practical guide to frequency-dependent phenomena, 2012 Distinguished Instructor Short Course, Society of

Exploration Geophysicists.

Liu, Y. and T. D. Xia, 2011, Experimental study on influence of particle roughness on shear wave velocity of sand, Chinese Journal of Geotechnical Engineering, **33**, 285-290.

Liu, H. and L. Peselnick, 1983, Investigation of internal friction in fused quartz, steel, plexiglass, and Westerly Granite from 0.01 to 1.00 Hertz, Journal of Geophysical Research, **88**, 2367-2379.

Macrae, J. C., and W. A., Grey, 1961, Significance of the properties of materials in the packing of real spherical particles, British Journal of Applied Physics, **12**, 164-172.

Makarynska, D., B. Gurevich, J. B., and Batzle, M., 2010. Fluid substitution in rocks saturated with viscoelastic fluids: Geophysics, **75**, E115-E122.

Makse, H. A., and H. J., Herrmann, 1999, Microscopic model for granular stratification and segregation, **43**, 1-6.

Makse, H. A., 2004, Granular packings: Nonlinear elasticity, sound propagation and collective relaxation dynamics, Physical Review E, **70**, 061302.

Marion, D., A. Nur, H. Z., Yin, and D. H., Han, 1992, Compressional velocity and porosity in sand-clay mixtures, Geophysics, **57,** 554-563.

Mavko, G., T. Mukerji, and J. Dvorkin, 2009, The rock physics handbook: The tools for seismic analysis in porous media, Cambridge University Press.

Mavko, G., T. Mukerji, and J. Dvorkin, 1998, The rock physics handbook: Tools for seismic analysis in porous media. New York: Cambridge University Press, 106-160.

McKavanagh, B. and F. D. Stacey, 1974, Mechanical hysteresis in rocks at low-strain amplitudes and seismic frequencies, Physics of the Earth and Planetary Interiors, **8**, 246-250.

Miller, S. L., and R. R., Stewart, 1990, Effects of lithology, porosity and shaliness on P- and S-wave velocities from sonic log, Canadian Journal of Exploration Geophysics, **26**, 94-103.

Mindlin, R. D., 1949, Compliance of elastic bodies in contact, Journal of Applied Mechanics, **16**, 259-268.

Müller, T. M., B. Gurevich, and M. Lebedev, 2010, Seismic wave attenuation and dispersion resulting from wave-induced flow in porous rocks—A review, Geophysics,

75, 75A147-75A164.

Murphy, W. F., 1982, Effects of partial water saturation on attenuation in Massilon sandstone and Vycor porous glass, Journal of the Acoustical Society of America, **71**, 1458–1468.

Murphy, W. F. III, 1982, Effects of microstructure and pore fluids on the acoustic properties of granular sedimentary materials [Ph.D. dissertation], Stanford University.

Murphy, W. F., J. N. Roberts, D. Yale, and K. W. Winkler, 1984, Centimeter-scale heterogeneities and microstratification in sedimentary rocks, Geophysical Research Letters, **11**, 697–700.

Murphy, W. F. I., K. W. Winkler, and R. L. Kleinberg, 1986, Acoustic relaxation in sedimentary rocks: Dependence on grain contacts and fluid saturation: Geophysics, **51**, 757–766

Norris, A. N., and D. L., Johnson, 1997, Nonlinear elasticity of granular media, Journal of Applied Mechanics, **64**, 39-49.

Norris, A. N., P., Sheng, and A. J., Callegari, 1985, Effective-medium theories for two-phase dielectric media. Journal of Applied Physics, **57**, 1990-1996.

Nur, A., 1992, Critical porosity and the seismic velocities in rocks. Eos, Transactions, American, Geophysical Union, **73**, 43-66.

Nur, A., G. Mavko, J. Dvorkin, and D. Galmudi, 1998, Critical porosity: A key to relating physical properties to porosity in rocks, The Leading Edge, **17**, 357-362.

Nur, A., Tosaya, C., and Thanh, D. V., 1984. Seismic monitoring of thermal enhanced oil recovery processes: 54th Annual International Meeting, SEG, Expanded Abstracts, 118-121.

O'Connell, R. J., and B., Budiansky, 1974, Seismic velocities in dry and saturated cracked solid, Journal of Geophysical Research, **79**, 5412-5426.

Paffenholz, J., and H., Burkhardt, 1989, Absorption and modulus measurements in the seismic frequency and strain range on partially saturated sedimentary rocks, Journal of Geophysical Research, **94**, 9493-9507.

Peselnick, L., H. P., Liu, and K. R., Harper, 1979, Mechanical hysteresis loops of an anelastic solid and the determination of rock attenuation properties, Geophysical Research Letters, **6**, 545-548.

Pickett, G. R., 1963, Acoustic character logs and their application in formation evaluation, JPT, **3**, 659-667.

Ratnanabha, S., 2010, Numerical simulation of pore-scale heterogeneity and its effects on elastic, electrical and transport properties, [Ph.D. Thesis], Stanford University.

Rojas, M. A., J., Castagna, R., Krishnamoorti, and D. H., Han, 2008, Shear thinning behavior of heavy oil samples: laboratory measurements and modeling: 78th Annual International Meeting, SEG, Expanded Abstracts, 1714-1717.

Sams, M. S., J. P., Neep, M. H., Worthington and M. S., King, 1997, The measurement of velocity dispersion and frequency-dependent intrinsic attenuation in sedimentary rocks, Geophysics, **62**, 1456-1464.

Schmitt, D. R., 1999, Seismic attributes for monitoring of a shallow heated heavy oil reservoir: A case study: Geophysics, **64**, 368-377.

Shapiro, S. A., and Muller, T. M., 1999, Seismic signatures of permeability in heterogeneous porous media, Geophysics, **64**, 99-103.

Smith, T.M., C.H. Sondergeldz, and C.S. Rai, 2003, Gassmann fluid substitutions: A tutorial, Geophysics, **68**, 430-440

Song, J. H., 1986, Measurement of the visco-elasticity of Daqing crude oils: Oilfield Surf. Facil, **5**, 12– 21 (in Chinese).

Spencer, J.W., 1981, Stress relaxations at low frequencies in fluid-saturated rocks: Attenuation and modulus dispersion, Journal of Geophysical Research, **86**, 1803–1812.

Steinour, H. H., 1944, Rate of sedimentation, concentrated flocculated suspensions of poweders, Industry energy and chemistry, **36**, 840-847.

Tang, X. M., M. N. Toksὸz, P. Tarif, and R. H. Wilhens, 1987, A method for measuring acoustic wave attenuation in the laboratory, Journal of the Acoustical Society of America, **83**, 453-462.

Tittmann, B. R., V. A., CALARK, J. M., Richardson and T. W., Spencer, 1980, Possible mechanism for seismic attenuation in rocks containing small amounts of volatiles, Journal of Geophysical Research, **85**, 5199-5208.

Toksὸz, M. N., and D. H., Johnston, 1981, Seismic wave attenuation, SEG Geophysics reprint, 2.

Toksὸz, M. N., D. H., Johnston, and A., Timur, 1978, Attenuation of seismic waves in

dry and saturated rocks: I. Laboratory measurement, Geophysics, **44**, 681-690.

Tutuncu, A. N., J. Dvorkin., and A. Nur, 1997, Influence of cementation and permeability on wave velocities in poorly consolidated sands, International Journal of Rock Mechanics & Mineral Society, **34**, p313.

Wang, Z. J., and A. Nur, 2000, Seismic and acoustic velocities in reservoir rocks, recent developments, Geophysics reprint series.

White, J. E., 1983, Underground sound, application of seismic waves, Elsevier Science Publishers B.V.

Walton, K., 1987, The effective elastic modulus of a random packing of spheres, Journal of the Mechanics and Physics of Solids, **35**, 213-226.

White, J. E., 1975, Computed seismic speeds and attenuation in rocks with partial gas saturation: Geophysics, **40**, 224–232.

Wilson, M. D., and E. D., Pittman, 1977, Authigenic clays in sandstones: Recognition and influence on reservoir of sedimentary and paleoenvironmental analysis, Journal of Sedimentary Petrology, **47**, 3-31.

Winkler, K., 1983, Contact stiffness in granular porous materials: Comparison between theory and experiment, Geophysical Research Letters, **10**, 1073–1076.

——－, 1985, Dispersion analysis of velocity and attenuation in Berea sandstone: Journal of Geophysical Research, **90**, 6793–6800

Winkler, K., A., Nur, and M., Gladwin, 1979, Friction and seismic attenuation in rocks, Nature, 277, 528-531.
Winkler, K., and A., Nur, 1982, Seismic attenuation—Effects of pore fluids and frictional sliding, Geophysics, **47**, 1–15.

Winkler, K., H. L., Liu, and D. L., Johnson, 1989, Permeability and borehole Stoneley waves: Comparison between experiment and theory. Geophysics, **54**, 66-75.

Worden, R. H., and S. D., Burley, 2003, Sandstone diagenesis: The evolution of sand to stone, International Association of Sedimentologists Reprint Series, **4**, 3-44.

Xia, T. D., Y., Liu, and M., Wu, 2011, Shear wave velocity in deep buried sand based on spheres-contact theory, Journal of Harbin Institute of Technology, **43**, 99-103.

Yao, Q., 2014, Velocity dispersion and attenuation in reservoir [Ph.D. Thesis],

University of Houston.
Yin, C. S., M. L., Batzle, and B. J., Smith, 1992, Effects of partial liquid gas saturation on extensional wave attenuation in Berea sandstone, Geophysical Research Letters, **19**, 1399–1402.

Zhao, L., 2014, Poroelastic and seismic characterization of heterogeneous reservoir rocks [Ph.D. Thesis], University of Houston.

Zimmer, M., 2003, Controls on the seismic velocities of unconsolidated sands: Measurements of pressure, porosity, and compaction effects [Ph.D. dissertation], Stanford University.

Zimmer, M., M., Prasad, and G., Mavko, 2002, Empirical velocity-pressure and porosity-pressure trends in unconsolidated sands, SEG Annual Meeting, Expanded Abstract, **72**, 1866-1869.

Appendix

Appendix A

Arrangement type I:

The volume *V* of the cement at each cement region for each grain is:

$$V = \int_0^a (h + \frac{r^2}{2R}) * 2\pi r dr = \pi a^2 h + \frac{a^4}{4}\frac{\pi}{R} \quad (1)$$

Therefore, the overall volume of the cement for the sandstone is:

$$V_2 = (\pi a^2 h + \frac{a^2}{4}\frac{\pi}{R}) nm \quad (2)$$

where *n* is the number of grains around each grain (coordination number) and *m* is the number of grains in the sandstone.

From the definition of critical porosity (Nur, 1992; Guo, 2012), the relationship between the whole volume V_3 of the sandstone and the volume V_4 occupied by the grains in the sandstone is

$$V_4 = (1 - \phi_0) V_3 \quad (3)$$

where ϕ_0 is the critical porosity of the sandstone. The expressions for V_3 and V_4 are as follows:

$$V_3 = \frac{4}{3}\pi R_1^3 \qquad V_4 = \frac{4}{3}\pi m R^3 \quad (4)$$

With the combination of Equations 3 and 4, I can obtain the following relationship between R_1 and R:

$$R_1^3 = \frac{mR^3}{1-\phi_0} \tag{5}$$

Therefore, the relative volume of the cement in the loose sandstone is:

$$C_1 = \frac{(\pi a^2 h + \frac{a^2}{4}\frac{\pi}{R})nm}{\frac{4}{3}\pi\frac{mR^3}{1-\phi_0}} \tag{6}$$

Assuming that the porosity of the sandstone is ϕ, then:

$$C_1 = \phi_0 - \phi \tag{7}$$

From Equations 6 and 7, we can get the following equation for α:

$$\frac{3n}{16}\alpha^4 + \frac{3n\varepsilon}{4}\alpha^2 - \frac{\phi_0 - \phi}{1-\phi_0} = 0 \tag{8}$$

Where $\alpha = \frac{a}{R}$, it is the normalized cementation radius; where $\varepsilon = \frac{h}{R}$, it is the normalized contact thickness.

By solving Equation 8, the expression for α is:

$$\alpha = \sqrt{-2\varepsilon + 2\sqrt{\varepsilon^2 + \frac{4}{3n}\frac{\phi_0 - \phi}{1-\phi_0}}} \tag{9}$$

If set ε=0, Equation 9 is simplified as:

$$\alpha = 2[\frac{\phi_0 - \phi}{3n(1-\phi_0)}]^{0.25} \tag{10}$$

Arrangement type II:

If the cement is distributed evenly around the grain, the thickness of the cement layer

can be expressed as follows:

$$H = \frac{a^2}{2R} \tag{11}$$

where a is the cementation radius; R is the radius of the grain.

Therefore, the content of the cement in the sandstone is

$$V_6 = [\frac{4}{3}\pi(R + \frac{a^2}{2R})^3 - \frac{4}{3}\pi R^3]m$$

$$= \frac{4}{3}\pi m(\frac{3}{2}a^2 R + \frac{3}{4}\frac{a^4}{R} + \frac{a^6}{8R^3}) \tag{12}$$

We can get the following equation:

$$\frac{\frac{4}{3}\pi m(\frac{3}{2}a^2 R + \frac{3}{4}\frac{a^4}{R} + \frac{a^6}{8R^3})}{\frac{4}{3}\pi\frac{mR^3}{1-\phi_0}} = \phi_0 - \phi \tag{13}$$

From Equation 13, I can get the following equation:

$$\frac{3}{2}\alpha^2 + \frac{3}{4}\alpha^4 + \frac{1}{8}\alpha^6 = \frac{\phi_0 - \phi}{1-\phi_0} \tag{14}$$

Because $\alpha<1$, $\alpha^6<<\alpha^4<<\alpha^2$, α^6 and α^4 can be ignored, then it can get the expression for α with arrangement type II:

$$\alpha = \sqrt{\frac{2(\phi_0 - \phi)}{3(1-\phi_0)}} \tag{15}$$